Effect of time-varying freestream on performance and vortex dynamics of forward and reversed pitching airfoils

Lei Shi[1,2], Yefang Wang[2], Annie-Claude Bayeul-Lainé[1], Olivier Coutier-Delgosha[1,3]

[1]Arts et Métiers ParisTech, ONERA, CNRS, Univ. Lille, Centrale Lille, UMR 9014-LMFL-Laboratoire de Mécanique des Fluides de Lille-Kampé de Fériet, F-59000 Lille, France

[2]Research Centre of Fluid Machinery Engineering and Technology, Jiangsu University, China

[3]Kevin T. Crofton Department of Aerospace and Ocean Engineering, Virginia Tech, Blacksburg, VA 24060, USA

[*]Corresponding author e-mail: mumuyedda@126.com

Abstract

The goal of the present work deals with the influence of the oscillating freestream on the global performance, transition and vortex dynamics of forward and reversed airfoils. Three important parameters, involving the phase lag, oscillating amplitude and mean reduced frequency, are analyzed systematically. The primary results show that both the phase lag and oscillating amplitude have great impact on the transition and flow structures, depending on the instantaneous freestream Reynolds number. The reversed airfoil is more prone to being affected by these parameters, characterized by the earlier flow separation near the sharp leading edge and the more complex vortex shedding, compared with that over the forward airfoil. It shows that increasing the oscillating amplitude can improve the mean performance, but it decreases with the increase of the mean reduced frequency. Additionally, it is observed that there is a second transition on both two sides near the trailing edge of the reversed airfoil, which becomes weak when the instantaneous freestream Reynolds number is relatively low. Afterwards, the time-averaged performance of the reversed airfoil is better than forward airfoil at low reduced frequency, but it deteriorates dramatically with the increase of the reduced frequency. Furthermore, the transition and vortex evolution are delayed as the reduced frequency increases, and the delayed flow structures can be inferred from the velocity profiles in the wake region. Moreover, it can be seen that the velocity profile has a transition from the drag-indicative to thrust-indicative type when the reduced frequency increases, and the velocity variation in the vertical direction is more evident for the reversed airfoil due to the massive flow separation.

Keywords: freestream oscillation; transition; phase lag; oscillating amplitude; mean reduced frequency

1. Introduction

Many devices operating in propulsive mode or in energy recovery mode are based on the kinematics of foil motions, mainly including the plunging (or heaving), pitching and flapping (combination of plunging and pitching) [1]. The pure pitching is a simple motion, referring to the target rotating around a pivot-point. A quantity of experimental and numerical works has been done previously, with special emphasis on the dynamic stall prediction and unsteady vortical flows. For some examples, Wang et al. [2] found that the SST k-ω (Shear Stress Transport) model shows the superiority than the standard k-ω model, in terms of the dynamic stall location and the life-span and thickness of the leading-edge vortex (LEV). As a complementary, Wang et al. [3] stated that the complex flows of the deep dynamic stall and boundary-layer transition can be well predicted by the SST k-ω based DES (Detached Eddy Simulation) approach, compared with the RANS-based (Reynolds Averaged Navier-Stokes) turbulence models. Tseng and Cheng [4] used the SST k-ω model to simulate two-dimensional flows over a pitching airfoil at high Reynolds number of 2.5×10^{6}, and the mechanism of the delayed dynamic stall is clarified in detail on the basis of the LEV formation stage. Moreover, the vortex generation mechanism and the trajectory over a pitching airfoil are also revealed by Tseng and Hu [5], with the aid of the Lagrangian coherent structures (LCS) methodology. Both on the stationary or oscillating foils, one of the well-known phenomena, namely laminar-turbulence transition, should not be neglected due to the impact on the overall performance. Therefore, the SST γ-$Re_{\theta t}$ transition model, initially proposed by Menter et al. [6-7], was adopted by Ducoin et al. [8] to investigate the pitching hydrofoil with the amplitude ranging from $0°$ to $15°$, and the main conclusion is that increasing the pitching velocity can delay or even suppress the laminar-turbulence transition during the pitch-up motion. Recently, Zhang et al. [9] also employed the SST γ-$Re_{\theta t}$ transition model to shed light on the mechanism of the dynamic stall delay associated with the delay of the LEV as the pitching rate increases, and the suppression of hysteresis loops and the intensification of the dynamic force fluctuation at lower pitching rate.

In many vertical-axis turbines and propellers, the propulsive system comprises several blades that have two basic motions: rotation and pitching. As shown in figure 1, the two-bladed cycloidal rotor operates in forward flight, which can produce the lift and propulsive force continuously. In a specific cycle, it would undergo the retreating side when the foil geometry is shown reversely, leading to the flow moving from the sharp leading edge to the blunt trailing edge. When the foil operates in the reversed mode, the blade loading and flow structures show significant difference compared with that at advancing side. There are also some related works performed on the reversed airfoil/hydrofoil. Lind et al. [10-11] shown that the performance of the reversed airfoil becomes much worse compared with the forward airfoil because of the early flow separation near the sharp leading edge, and detected three wake regimes, involving the slender body vortex shedding, turbulent and deep stall vortex shedding. The influence of Reynolds number is also studied by Lind et al. [12] for NACA0012 and NACA0024 airfoils and it concludes that the airloads of NACA0012 is almost insensitive to the Reynolds number compared with NACA0024, for the reason that it acts like a thin airfoil because of the sharp leading edge. At incidence of $0°$, Marchand et al. [13] found that the discontinuity lift occurs for NACA0015 hydrofoil at Reynolds number of 5×10^{5}, which is induced by the leading-edge separation bubble and asymmetrical boundary layer near the blunt trailing edge. When it comes to the reversed pitching airfoil, Lind and Jones [14] reported that the reversed dynamic stall is weakly sensitive

to the Reynolds number, but is strongly affected by the reduced frequency. The number of vortex structures increase with the reduction of the reduced frequency, and with the increase of the maximal pitching angle. Lastly, Smith and Jones [15] investigated the influence of the yawed angle on the reversed pitching foil, and the results show that the yawed blade can suppress the secondary flow structures and delay the breakup of the reverse flow dynamic stall vortex (RFDSV).
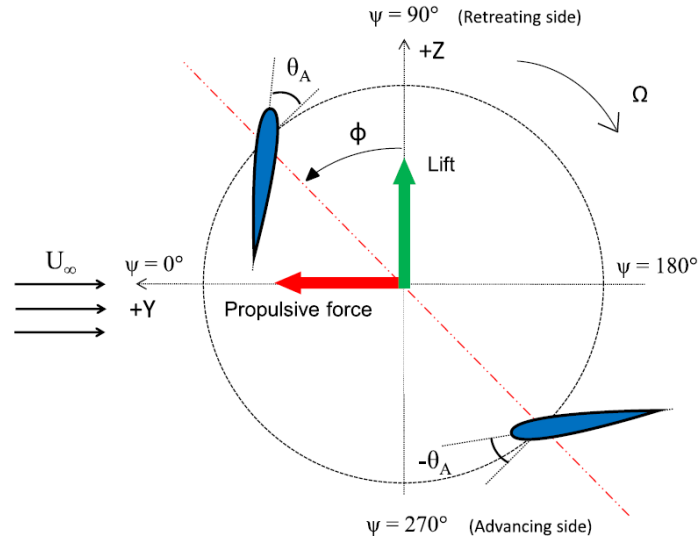

Figure.1 Sketch of cycloidal rotor system.

In most cases, the performance and unsteady vortical flows are predicted in steady-flow state numerically and experimentally. However, in practice, the operating environment is not steady and it is always transient and non-linear. The pitching airfoils in steady flow have been extensively investigated for many years, but relatively few studies have addressed the effect of the unsteady inflow on the oscillating objectives. Under stall condition at incidence of 20°, Gursul and Ho [16] conducted the experiments to demonstrate that the phase-averaged lift coefficient of NACA0012 is much higher than the conventional value, at an optimal reduced frequency of the unsteady freestream. Concerning the boundary layer flows measured by the experiments, Brendel and Mueller [17] and Strangfeld et al. [18] both found that the oscillating inflow has great impact on the location of the separation bubble and its subsequent shedding, which indicates that the transition is influenced considerably. For the pitching blade with the application to the helicopter rotor, Pierce et al. [19] performed the experiments in a low-speed wind tunnel with an axis gust generator and clarified that the velocity perturbations have a significant effect on the pitching moment, but no remarkable influence on the blade instability. Then, effects of different parameters on the airfoil performance and flow structures, including the Reynolds number and attack angle [20], the phase difference between the freestream oscillation and airfoil oscillation [21] and the oscillation frequency ratio between the freestream and foil motion [22], are investigated systematically previously. Furthermore, by performing the experiments over a pitching delta wing, Shi and Ming [23] elaborated the mechanism of the maximal lift increase and dynamic stall angle delay, which is ascribed to the change of the leading-edge vortex structure. Recently, to study the evolution of the leading-edge vortex and boundary layer unsteadiness, the experiments were done in a wide range of freestream oscillating amplitudes and reduced frequencies by Smith and Jones [24]. Simultaneously, the vortex formation over the reversed airfoil under freestream oscillating condition was investigated by Kirk and Jones [25]

experimentally and main results include the higher convection speed and comparable strength of LEVs in reverse flow surge compared with the reverse flow LEVs. According to the study mentioned above, it concludes that most of the results are obtained by the experiments and a few works are carried out using the numerical methodology. It admits that there is still a challenging to the experimental measurements due to the difficulty in accessing to the thin boundary layer. The numerical results are always achieved by the RANS-based turbulence models without the consideration of the transition effect, which is inappropriate because the laminar-turbulence transition is inevitable at low Reynolds number and is dominated when the attack-of-angle is relatively small.

Inspired by the aforementioned works and considering the gap in transition and vortical flows under unsteady inflow conditions, the present work aims to study the global performance, boundary layer event and unsteady vortical flows around the forward and reversed pitching airfoils under time-varying freestream conditions. The main parameters, involving the oscillating amplitude, phase lag and reduced frequency, are also considered. It is believed that this work can deep the underlying physics of flow structures under such special conditions and provide some inspirations to a better design of some energy harvesting equipment.

2. Computational methodology

2.1 Problem formulation

As is shown in figure 2, a two-dimensional rigid symmetrical airfoil NACA0018 is placed in the centre of the computational domain. The airfoil has a chord length $c=0.348$m, and the prescribed oscillation is

$$\alpha(\Phi) = \alpha_0 + \alpha_1 \sin(\Phi) \tag{1}$$

where α_0 is the mean angle-of-attack, α_1 is the pitching amplitude and Φ is the phase angle. In the present work, the pitching is symmetrical and the mean incidence is $0°$. The peak-to-peak amplitude of the oscillating motion is $60°$.

The inflow variation is given by

$$U_0(\Phi) = U_0[1 + \sigma sin(\Phi - \tau)] \tag{2}$$

where U_0 is the mean inflow velocity, σ is the amplitude of the freestream oscillation and τ is the phase lag relative to the pitching motion.

On the basis of the airfoil chord length and freestream velocity, the temporal variation of the Reynolds number Re is described by

$$Re(\Phi) = \frac{U_0(\Phi)c}{\nu} \tag{3}$$

where ν is the kinematic viscosity of the working fluid.

Also, the non-dimensional parameters used to determine the aerodynamic coefficient vary temporally, which are written as follows

$$L(\Phi) = \frac{1}{2}C_l(\Phi)\rho c U_0^2(\Phi) \tag{4}$$

$$D(\Phi) = \frac{1}{2}C_d(\Phi)\rho c U_0^2(\Phi) \tag{5}$$

$$M(\Phi) = \frac{1}{2}C_m(\Phi)\rho c^2 U_0^2(\Phi) \tag{6}$$

where $L(\Phi)$, $D(\Phi)$ and $M(\Phi)$ are the lift, drag and moment, and $C_l(\Phi)$, $C_d(\Phi)$ and $C_m(\Phi)$ are the lift, drag and moment coefficient, respectively.

For the pitching airfoil, the classical definition of the nondimensional pitching frequency is given by

$$k_n = \frac{\pi f c}{U_0} \tag{7}$$

Due to the freestream oscillation, the instantaneous reduced frequency is introduced by

$$k(\Phi) = \frac{\pi f c}{U_0(\Phi)} \tag{8}$$

where f is the pitching frequency.

2.2 Turbulence modelling

The computational fluid dynamics (CFD) package STARCCM + with an unsteady incompressible and viscous flow solver is employed to model the flows around the pitching airfoil. The governing equations for the unsteady incompressible flow are shown as follows

$$\nabla \cdot \boldsymbol{u} = 0 \tag{9}$$

$$\frac{d\boldsymbol{u}}{dt} = -\frac{1}{\rho}\nabla p + \nu \nabla^2 \boldsymbol{u} \tag{10}$$

where $\boldsymbol{u}$ donates the velocity vector and p refers to the pressure.

The SST γ-$Re_{\theta\text{t}}$ transition model is applied, with the consideration of the transition effect. The advantage of the SST k-ω model is that it can reduce the strong freestream sensitivity compared with the standard k-ω model and improve the prediction of the adverse pressure gradient [26]. The governing equations for the SST k-ω model are displayed as follows

$$\frac{\partial(\rho k)}{\partial t} + \frac{\partial(\rho k u_j)}{\partial x_j} = P_k - D_k + \frac{\partial}{\partial x_j}\left[(\mu + \sigma_k \mu_t)\frac{\partial k}{\partial x_j}\right] \tag{11}$$

$$\frac{\partial(\rho \omega)}{\partial t} + \frac{\partial(\rho \omega u_j)}{\partial x_j} = \frac{\gamma}{\nu_t}P - \omega^2 \rho \beta + \frac{\partial}{\partial x_j}\left[(\mu + \sigma_\omega \mu_t)\frac{\partial \omega}{\partial x_j}\right] + 2(1 - F_1)\frac{\rho \sigma_{\omega 2}}{\omega}\frac{\partial k}{\partial x_j}\frac{\partial \omega}{\partial x_j} \tag{12}$$

where k and ω are the turbulent kinetic energy and the rate of eddy dissipation. P_k and D_k are the production and destruction terms in turbulent kinetic energy equation, and F_1 is the blending function. The definitions of these functions and parameters can be found in reference [26].

To model the transition event, the other two additional equations, namely intermittency and transition momentum thickness Reynolds number, are introduced to trigger the onset of transition, which are written by

$$\frac{\partial(\rho \gamma)}{\partial t} + \frac{\partial(\rho \gamma u_j)}{\partial x_j} = P_\gamma - E_\gamma + \frac{\partial}{\partial x_j}\left[\left(\mu + \frac{\mu_t}{\sigma_\gamma}\right)\frac{\partial \gamma}{\partial x_j}\right] \tag{13}$$

$$\frac{\partial(\rho \overline{Re_{\theta t}})}{\partial t} + \frac{\partial(\rho u_j \overline{Re_{\theta t}})}{\partial x_j} = P_{\theta t} + \frac{\partial}{\partial x_j}\left[\sigma_{\theta t}(\mu + \mu_t)\frac{\partial \overline{Re_{\theta t}}}{\partial x_j}\right] \tag{14}$$

where P_γ and E_γ are the production and destruction terms in intermittency equation, while $P_{\theta t}$ is the production term in transition momentum thickness Reynolds number equation. The other empirical coefficients and correlations are described in detail in reference [6-7].

The coupling of the transition model with the turbulence model is given by

$$\frac{\partial(\rho k)}{\partial t} + \frac{\partial(\rho k u_j)}{\partial x_j} = \widetilde{P_k} - \widetilde{D_k} + \frac{\partial}{\partial x_j}\left[(\mu + \sigma_k \mu_t)\frac{\partial k}{\partial x_j}\right] \tag{15}$$

$$\widetilde{P_k} = \gamma_{eff}P_k \tag{16}$$

$$\widetilde{D_k} = min\left[max(\gamma_{eff}, 0.1), 1.0\right]D_k \tag{17}$$

where γ_{eff} is the effective intermittency.

Compared with the traditional transition model, the superiority of the SST γ-$Re_{\theta t}$ transition model is that it has the capability in dealing with the freestream turbulence, pressure gradient and separation and wall roughness. Also, it is based on the local variables which could be easily implemented into many CFD codes and it has no direct relationship with the momentum equation. Nowadays, this transition model has been successfully applied to many transitional flows over different objectives, such as the airfoils [27-28], the open water propeller [29] and the wind turbine [30].

2.3 *Computational configuration and mesh generation*

As shown in figure 2a and 2c, the computational domain is rectangular and the airfoil is placed in the middle section. The numerical configuration extends $3c$ from the airfoil leading edge and $10c$ from the trailing edge. The top-wall and bottom-wall have the same distance of $1.44c$ from the airfoil surface, which is the same compared with the experiment [20]. The pitch-pivot-point is located at $x/c=0.25$ from the leading edge.

The sliding mesh technique is employed to control the airfoil motion by creating an interface between the rotating part and the external stationary region. Concerning the mesh distribution, the trimmed mesh outside, with the prism layer inside the boundary layer, are used in the present work. The meshes both in the normal and streamwise directions should be considered because of its great impact on the transition. In addition, to minimize the effect of the vortical flow in the wake region, the mesh is refined by creating a cone covering the rotating part, which is shown in 2a. Therefore, the study of the mesh independence is only performed by changing the local mesh distribution, which is listed in table 1. Mesh 1, 2 and 4 are adopted to investigate the mesh distribution in the streamwise direction by changing the grid size over the airfoil surface, while the mesh effect in the normal direction is shown by mesh 3,4 and 5 via increasing the number of the prism layer, leading to the maximal y^+ for mesh 4 smaller than 0.1. The main results of different meshes are presented in figure 3 using the plots of the instantaneous lift, moment, pressure coefficient ($C_p=p/(0.5*\rho*U_0^2)$, where p is the pressure and U_0 is the inlet velocity) and skin friction coefficient ($C_f=\tau_w/(0.5*\rho*U_0^2)$, where τ_w is the magnitude of wall shear stress). The distributions of the lift and moment have large fluctuations as the airfoil experiences the large incidence, mainly at $\Phi=60°\sim140°$ and $240°\sim320°$, which is closely related to the intensive flow separation at relatively high attack-of-angle under the oscillating inflow condition. Furthermore, it is observed that the results obtained by mesh 1 and 2 have some difference in distributions of the lift, moment and pressure coefficient, compared with that for mesh 3, 4 and 5. Besides, as shown in figure 3d, when given the mesh in the normal direction, it seems that the transition point predicted by mesh 3 move downstream. However, for mesh 4 and 5, the distribution of the skin friction coefficient is quite similar. In summary, considering the mesh in the streamwise and normal directions, it seems that mesh 4 is appropriate for all the tested cases.
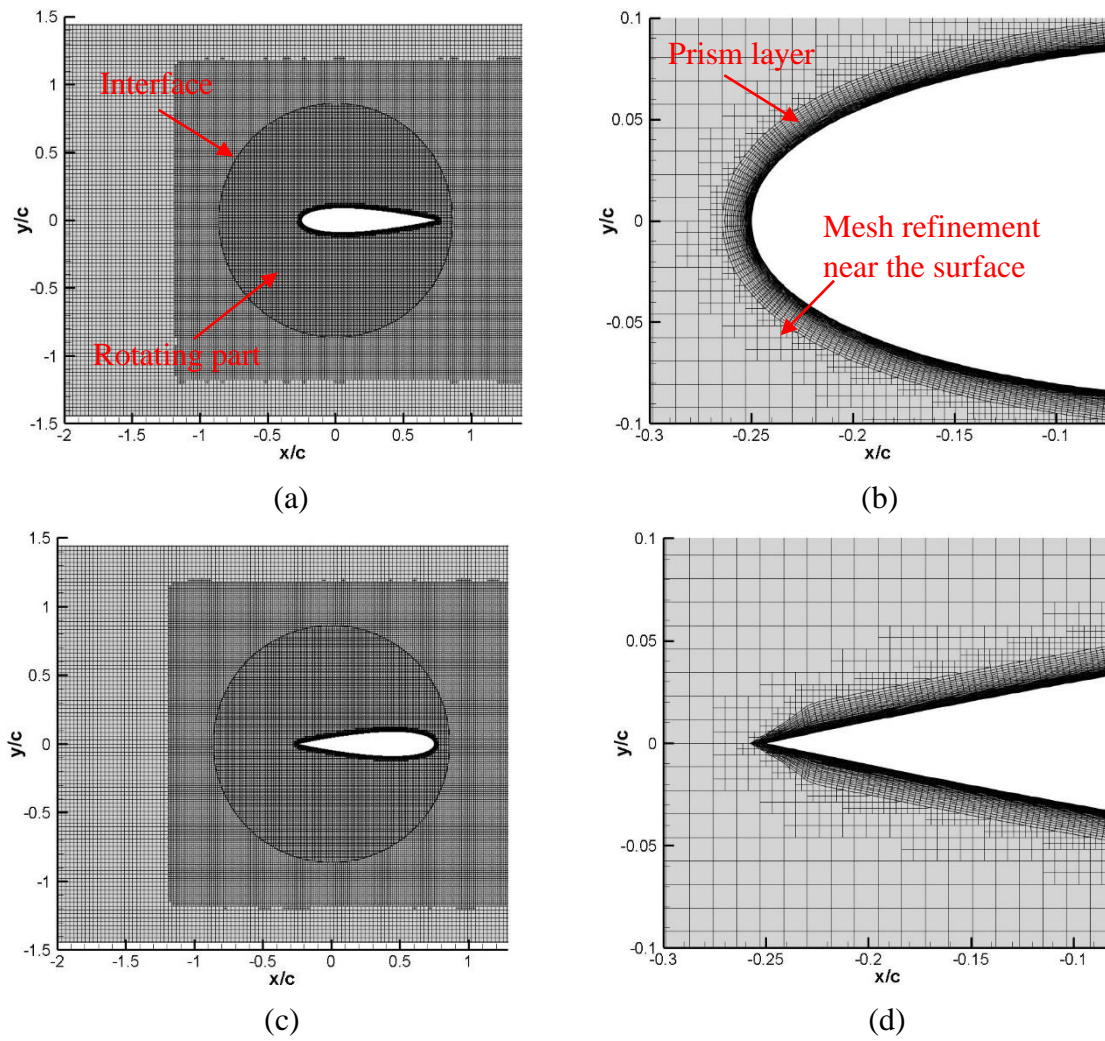
Fig.2 Partial views of mesh arrangements in the computational domain and near the airfoil surface. (a) Mesh in the computational domain for the forward airfoil; (b) Mesh distribution near the forward airfoil surface; (c) Mesh in the computational domain for the reversed airfoil; (d) Mesh distribution near the reversed airfoil surface.

Table 1 Detailed mesh information of the tested cases

	Target size of the mesh in the rotating part (mm)	Target size of the mesh over the surface (mm)	Prism layer thickness (mm)	Stretch ratio	Number of the prism layer	Total nodes
Mesh 1	5	2.5	5	1.1	60	171,943
Mesh 2	5	1.5	5	1.1	60	192,542
Mesh 3	4	1	5	1.1	50	197,898
Mesh 4	4	1	5	1.1	60	208,968
Mesh 5	4	1	5	1.1	70	212,658
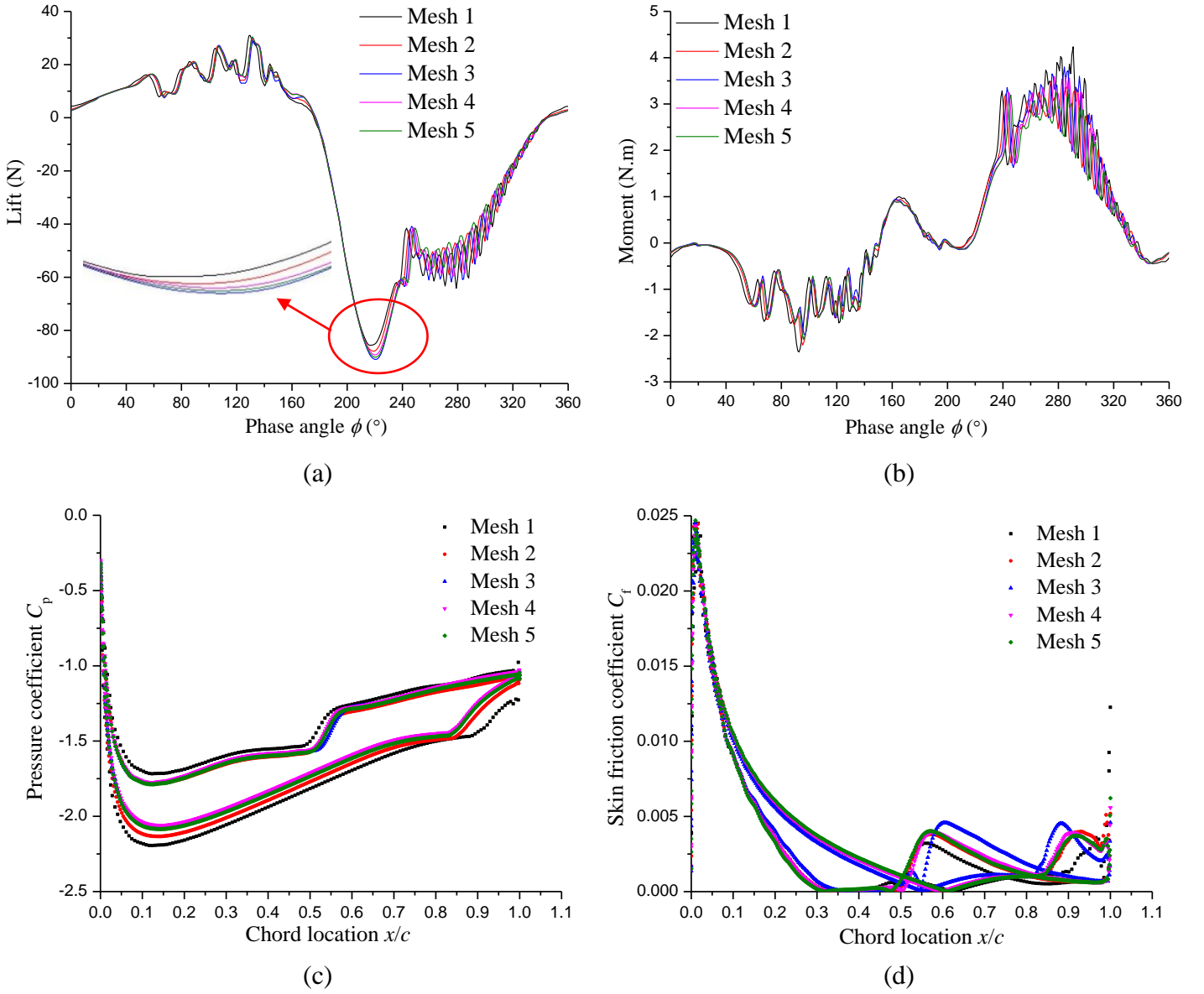
Fig.3 Plots of the instantaneous performance for different meshes. The tested case is with the oscillating freestream of $11.1 \cdot [1 + 0.5 \sin(\Phi - 135°)]$ and reduced frequency of 0.036. (a) Lift; (b) Moment; (c) Pressure coefficient; (d) Skin friction coefficient.

2.4 Numerical setup and boundary conditions

The classical boundary conditions are applied to the computational domain: the oscillating freestream is imposed on the inlet section while the pressure is assigned on the outlet section. The top-wall and bottom-wall are set as the symmetry planes to eliminate the wall effect while the airfoil surface is regarded as the no-slip wall. The finite-volume-based segregated flow solver is utilized to simulate the unsteady flow structures. In the simulations, the second-order upwind spatial discretization is used for the convective flux and the second-order central discretization is applied to the diffusion term. The all y^+ wall treatment is employed in this work, which is a blended wall function that adopts the low y^+ wall treatment for fine meshes, and the high y^+ wall treatment for the coarse mesh. The time-step also has remarkable effect on the flow fields and the main results for different timesteps are displayed in figure 4. It is observed that there are two regions where the lift and moment have large fluctuations: $60°{\sim}140°$ and $240°{\sim}320°$, which is possibly associated with the low freestream turbulence intensity [4] and the three-dimensional

effect in the downstroke stage [31]. Additionally, at relatively high incidence, the flow separation under oscillating freestream condition is also responsible for the performance fluctuation. With the decrease of the time-step, the fluctuation becomes more obvious, but the results are quite close in most of the time, for the cases with $\Delta t=0.3^{\circ}$/rotation and $\Delta t=0.25^{\circ}$/rotation. Consequently, the timestep of 0.3°/rotation is chosen in all cases. For each case, 15 rotations are necessary to get a periodic result of the computations.
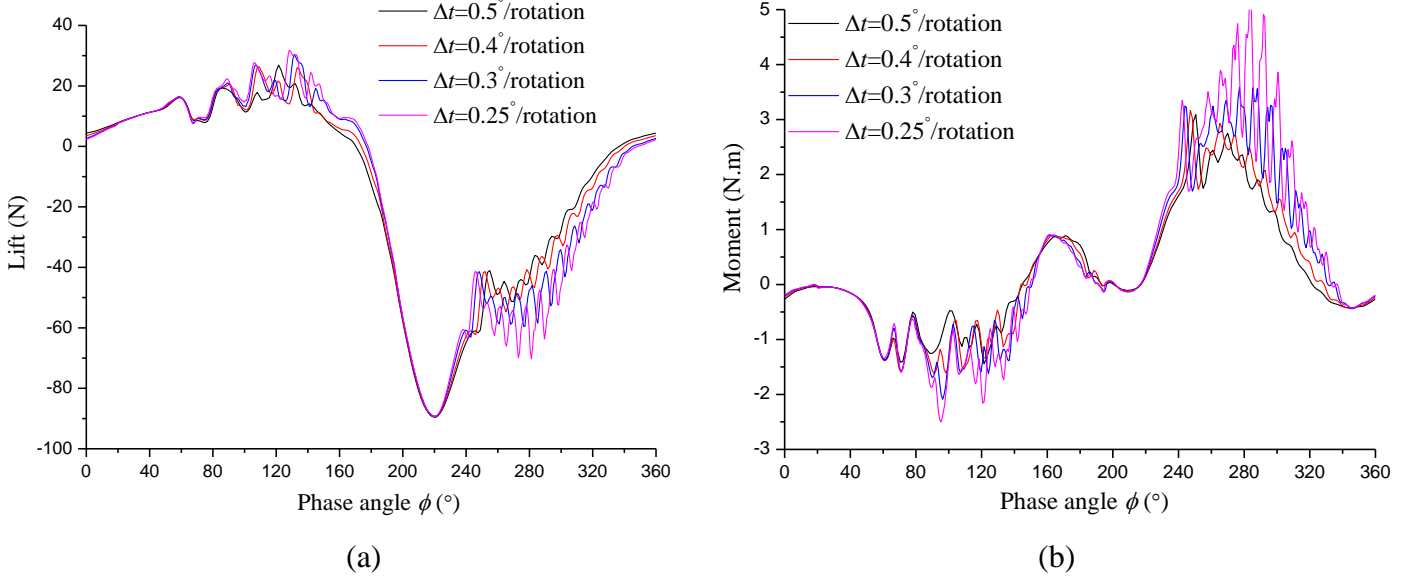
Fig.4 Plots of the instantaneous performance for different timesteps. The tested case is with the oscillating freestream of $11.1 \cdot [1 + 0.5 \sin(\Phi - 135^{\circ})]$ and reduced frequency of 0.036. (a) Lift; (b) Moment.

3. Results and discussion

3.1 *Validation of the transition over airfoils*

Due to the limited experiments about the transition for the pitching airfoil, the validation is conducted on the single stationary airfoils initially. Two airfoils, namely NACA0012 and 0018, are investigated at $Re=4.8\times10^4$ and 1.0×10^5, respectively. Three incidences, 6° for NACA0012 and 5° and 10° for NACA0018, are tested. The chord length of these two airfoils are 0.18m and 0.20m, and the numerical setup is similar with the experiments [32-33]. In figure 5, the time-averaged pressure coefficient C_p and skin friction coefficient C_f, and separation (SP), transition (TP) and reattachment points (RP) are plotted, which are used to compare with the available experiments. At relatively low incidence, the pressure distributions of two airfoils agree with the experiments. However, for NACA0018 at incidence of 10°, there is a little difference in the transition region. In addition, the SST k-ω model only resolves the fully turbulent flows, and it has no capability in capturing the laminar-turbulence transition. When it comes to the distribution of C_f, it is observed that NACA0012 has the largest size of the separation bubble, characterized by the early flow separation and delayed reattachment point. The separation point for NACA0012 at incidence of 6° is almost the same with that for NACA0018 at $\alpha=10^{\circ}$, but the reattachment point is more downstream, due to the influence of the incidence and Reynolds number. Similarly, the flow separation for NACA0018 at $\alpha=5^{\circ}$ is delayed, but the reattachment point is nearly at the same location, compared with NACA0012. As the incidence increases, both the separation and reattachment points shift upstream for NACA0018, which indicates that the length of the

separation bubble reduces significantly. By the comparison with the experiments, it seems that the transition region obtained by the computations are predicted well, as shown in figure 5c.

(a)

(b)

(c)
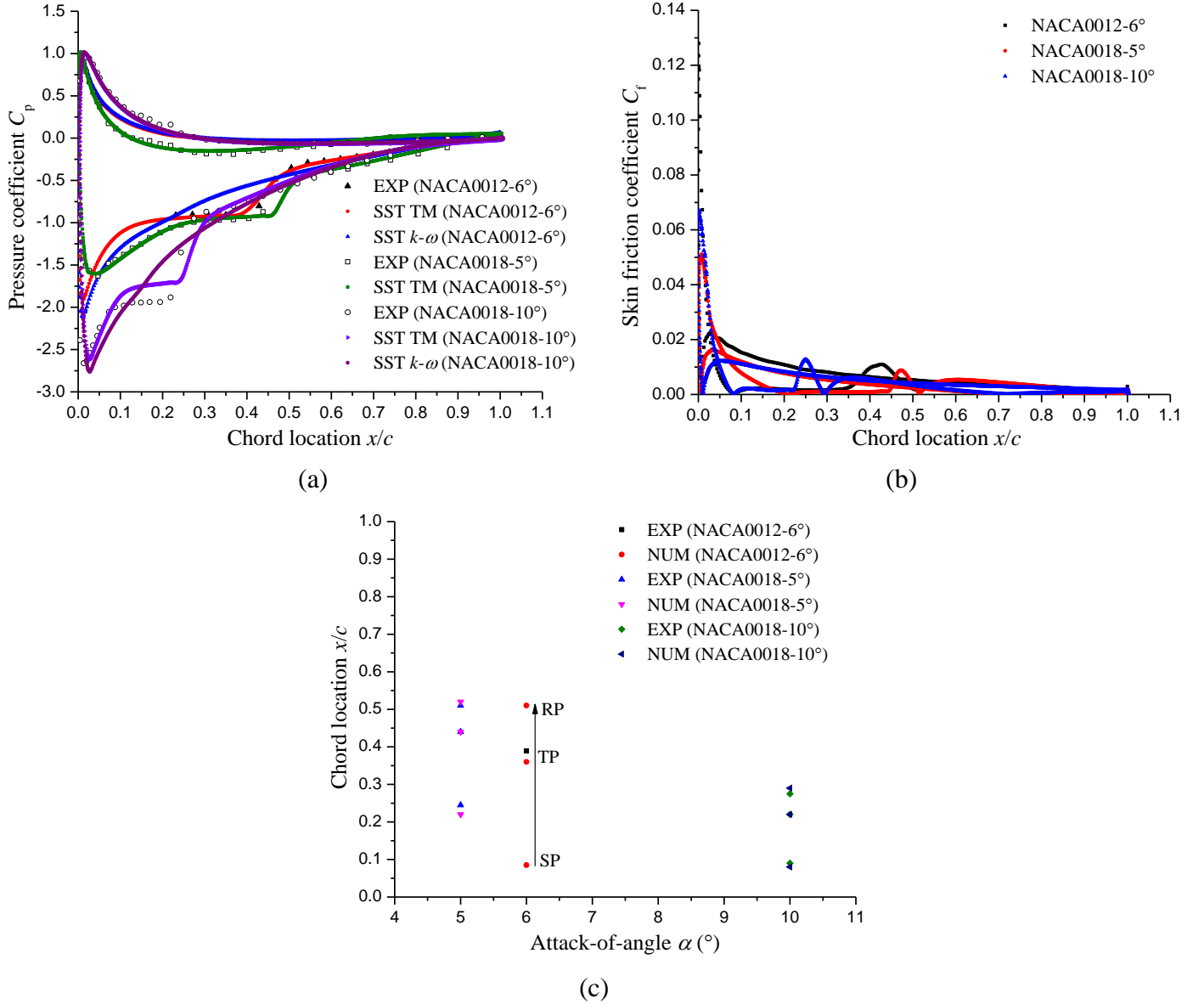
Fig.5 Transition over two different airfoils. (a) Pressure coefficient; (b) Skin friction coefficient; (c) Separation, transition and reattachment locations.

3.2 Effect of the phase lag τ

The phase lag between the pitching motion and the oscillating freestream is studied firstly. The variations of the incidence $\alpha(\Phi)$ and velocity $U_0(\Phi)$ are plotted in figure 6, under various phase lag conditions. The peak-to-peak amplitude is $60°$ for the pitching airfoil with a sinusoidal motion. The instantaneous lift and moment in a revolution are displayed in figure 6, to show the performance change induced by the phase lag. Compared with the experiments [20], it seems that the present simulation can capture the performance variation reasonably. For an example, the lift has an obvious positive peak as the phase angle is about $45°$ for the case with $\tau=315°$, followed by the case with the freestream oscillation amplitude equal to $0°$. This phenomenon is ascribed to the peak of the freestream velocity at $\Phi=45°$. When $\tau=135°$, in the up-stroke process, the variation of the lift is smooth. However, during the down-stroke at $\Phi=225°$ when the airfoil has a negative incidence, the negative peak of the lift occurs, which is associated with the maximal freestream

velocity at this instant. Therefore, it concludes that the variation of the airfoil performance has close relationship with the freestream velocity oscillation. In the up-stroke when the airfoil has a positive incidence, the positive lift peak exists at maximal freestream velocity, while the negative peak of lift is evident in the down-stroke when the incidence is negative. The variation trend of the moment is opposite with the change of the lift.

(a)

(b)

(c)
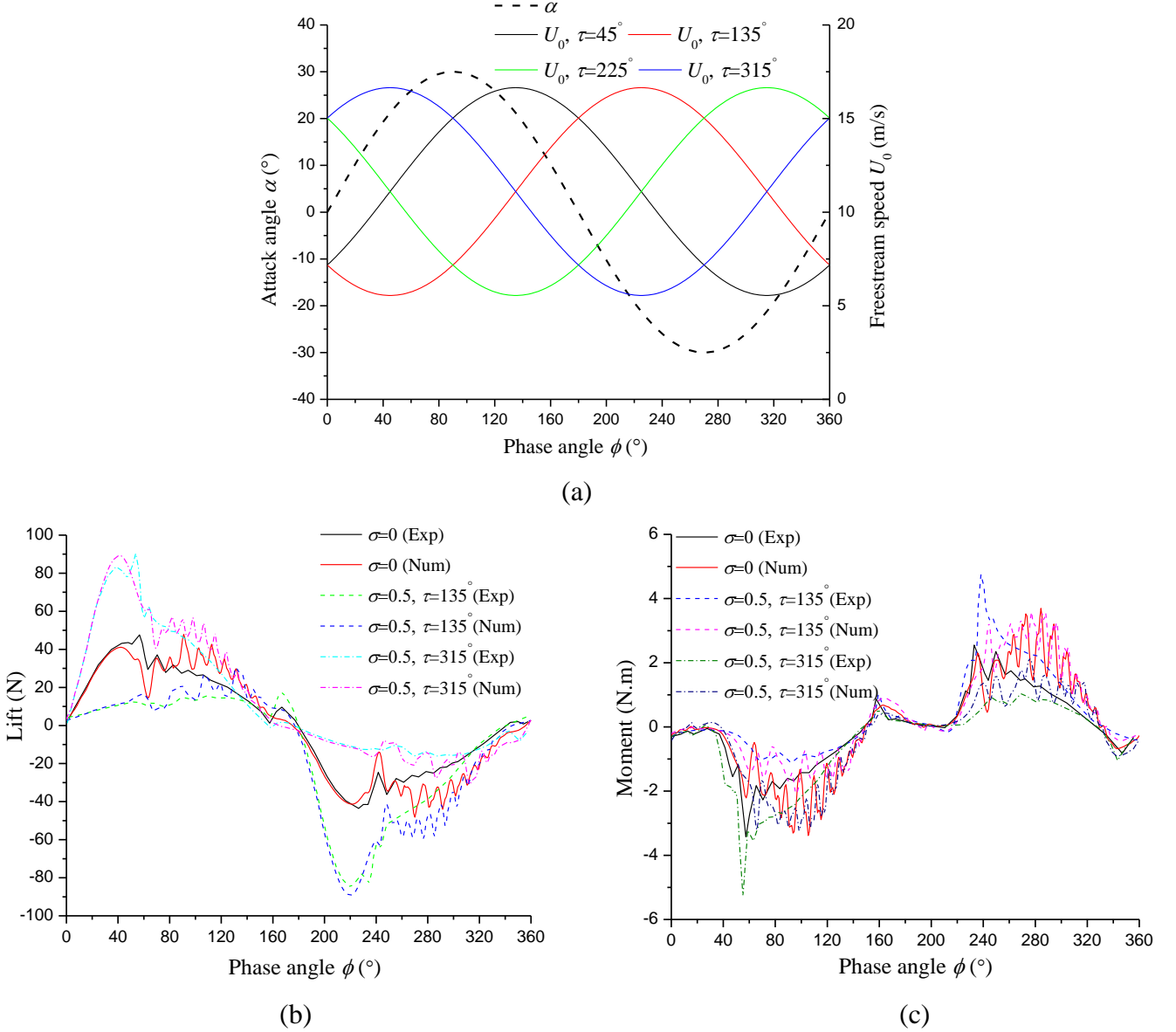
Fig.6 Plots of the instantaneous lift and moment in a revolution under various phase lag conditions. The tested case is with the oscillation freestream of $11.1 \cdot [1 + 0.5 \sin(\Phi - \tau)]$ and reduced frequency of 0.036. (a) Variations of the attack-of-angle and freestream velocity; (b) Lift; (c) Moment.

The non-dimensional lift and moment coefficients are plotted in figure 7 under various phase lag conditions. Using the non-dimensional coefficients can include the effect of the freestream velocity oscillation. For an instance, as $\tau=135°$, the lift coefficient is largest at $\Phi=55°$, although the magnitude of the lift at this instant is not much large, which is mainly due to the minimal freestream velocity. Moreover, at $\Phi=40°$, the lift peak is observed when $\tau=315°$, but the peak of the lift coefficient is not apparent because of the maximal freestream velocity shown in figure 6a. By the comparison with the experiments, it can be found that the predictive lift and moment coefficients obtained by the simulations have relatively large fluctuations because of the

unsteady oscillating freestream and the occurrence of the stall, but the computations can still get the main trend for different cases.

(a)

(b)

(c)

(d)
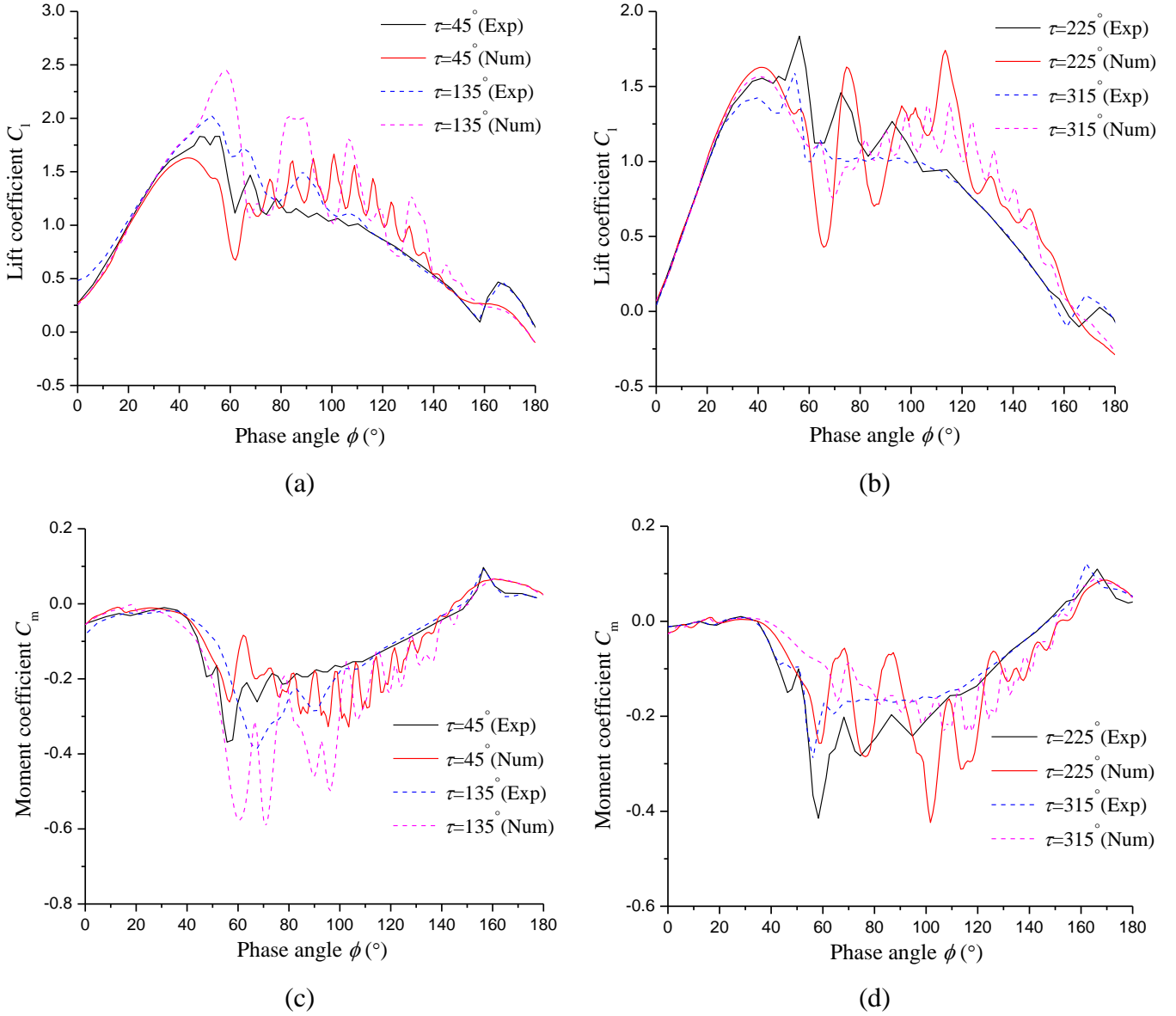
Fig.7 Plots of the instantaneous lift and moment coefficients in a revolution under various phase lag conditions. The tested case is with the oscillation freestream of $11.1 \cdot [1 + 0.5\sin(\Phi - \tau)]$ and reduced frequency of 0.036. (a) and (b) Lift coefficient; (c) and (d) Moment coefficient.

It can be seen that the lift and moment coefficients have large fluctuations in some regions at peak-to-peak amplitude of $60°$, therefore, it is of great importance to check if the performance also has the oscillation with the decrease of the pitching amplitude at different phase lag conditions. Three pitching amplitudes of $10°$, $20°$ and $30°$ at $\tau=135°$ and $315°$ are investigated in figure 8. The distributions of instantaneous lift, drag and moment coefficients show that increasing the pitching amplitude leads to the large performance fluctuation. However, the region where the performance fluctuates at two phase lag conditions is opposite. For an example, the large fluctuation of the lift appears at $\Phi=60°$-$140°$ for the case with $\tau=135°$, while it moves to the region at $\Phi=240°$-$320°$ when $\tau=315°$, which is due to the change of the freestream velocity in figure 6a. In addition, it is observed that the performance fluctuation at $\Phi=60°$-$140°$ is due to the increase of the freestream velocity from the minimal value, while the decrease of the freestream

velocity from the maximal magnitude is responsible for the fluctuation at Φ=240°-320°. Obviously, the former leads to the large fluctuation.
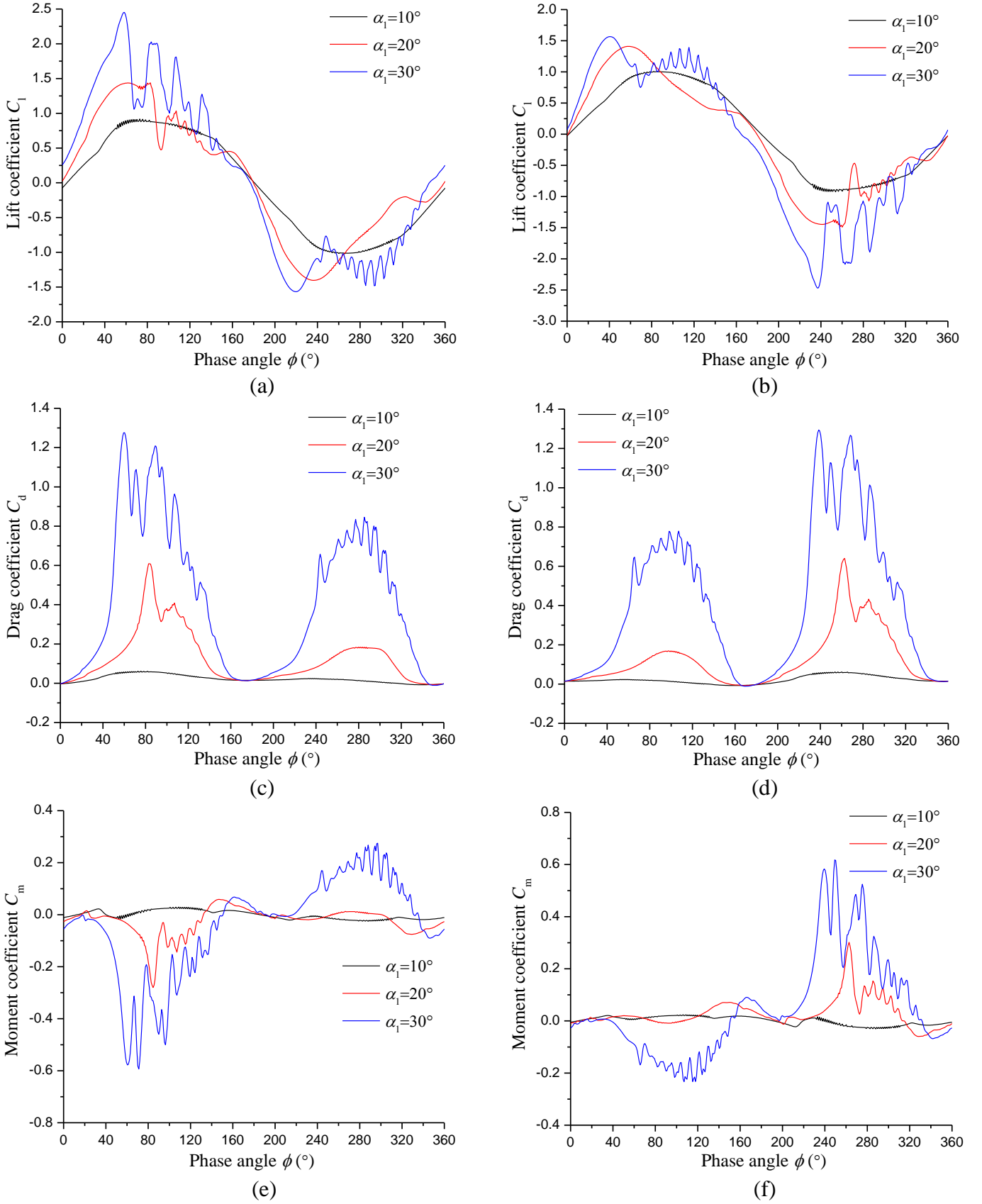
Fig.8 Plots of the instantaneous lift, darg and moment coefficients at two phase lag conditions for different pitching amplitudes. The tested case is with the oscillation freestream of $11.1 \cdot [1 + 0.5 \sin(\Phi - \tau)]$ and reduced frequency of 0.036. (a), (c) and (e) τ=135°; (b), (d) and (f) τ=315°.

The contours of the spanwise vorticity for three different cases in figure 6, are presented in figure 9 to clarify the difference of flow structures. Two different instants, corresponding to the maximal and minimal freestream velocity, are selected. The spanwise vorticity coupled with the streamlines are presented in figure 9 to describe the flow fields while the pressure coefficients C_p are also used to show the influence of the vortical flows on the performance. As $\Phi=45°$, the case with $\tau=135°$ has the minimal freestream velocity while it has the peak of the inlet velocity for the case with $\tau=315°$. At this moment, it is observed that both the leading-edge vortex (LEV) and trailing-edge vortex (TEV) coexist with the opposite sign of the vorticity. However, the LEV is still attached on the suction side in figure 9b, whereas it starts to separate in figure 9a and 9c, depending on the entrainment ability of the freestream. The distribution of the pressure coefficient in figure 9g shows that the attached LEV reduces the pressure on the suction side and further increases the performance, which is more obvious for the case with $\tau=135°$. Then, at $\Phi=225°$, the freestream velocity, vorticity and pressure coefficient have a opposite trend compared with the results at $\Phi=45°$. Therefore, it concludes that the change of the freestream velocity is responsible for the local flow structures and the performance remarkably.

(a)

(b)

(c)

(d)

(e)

(f)

(g)

(h)
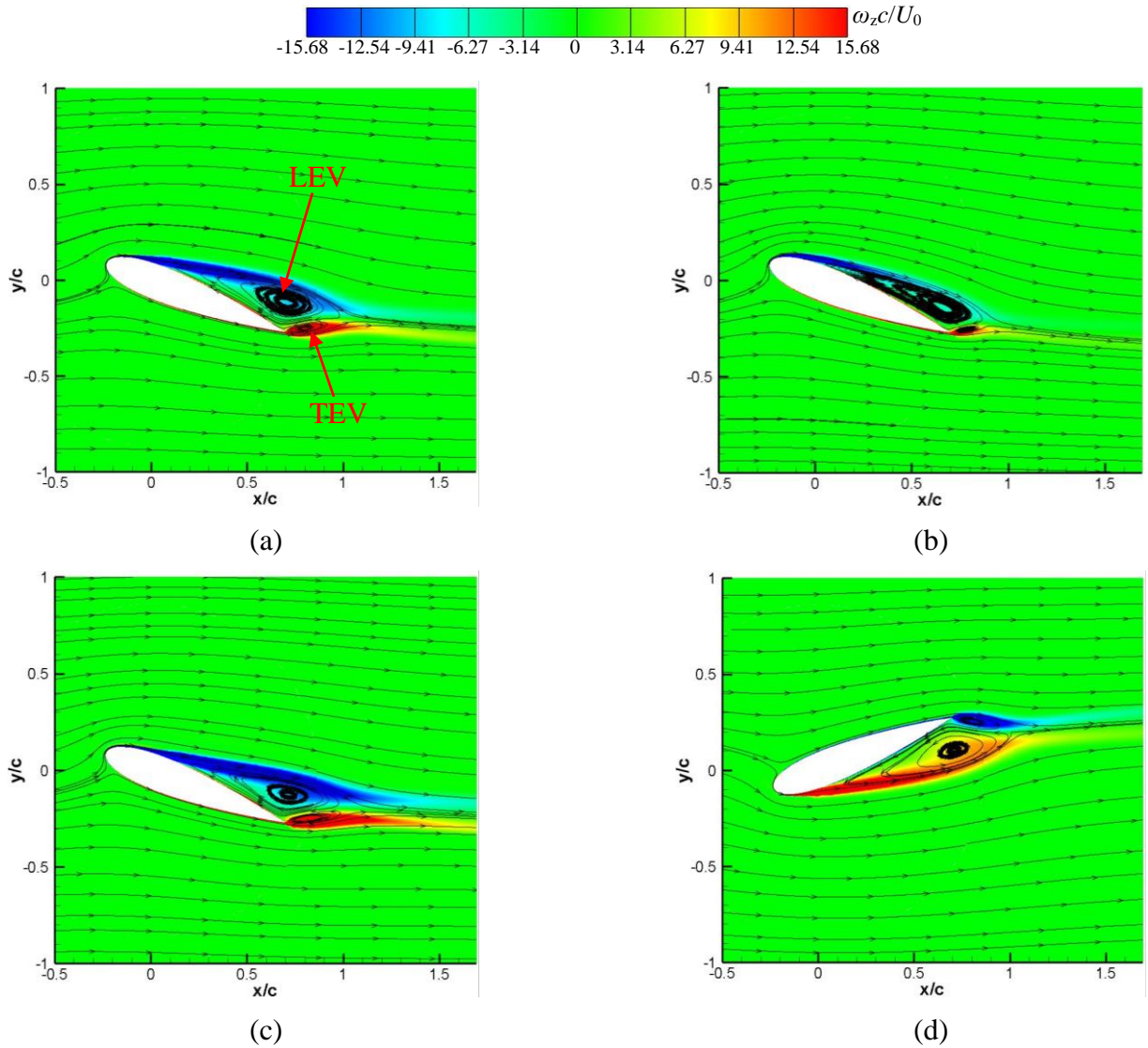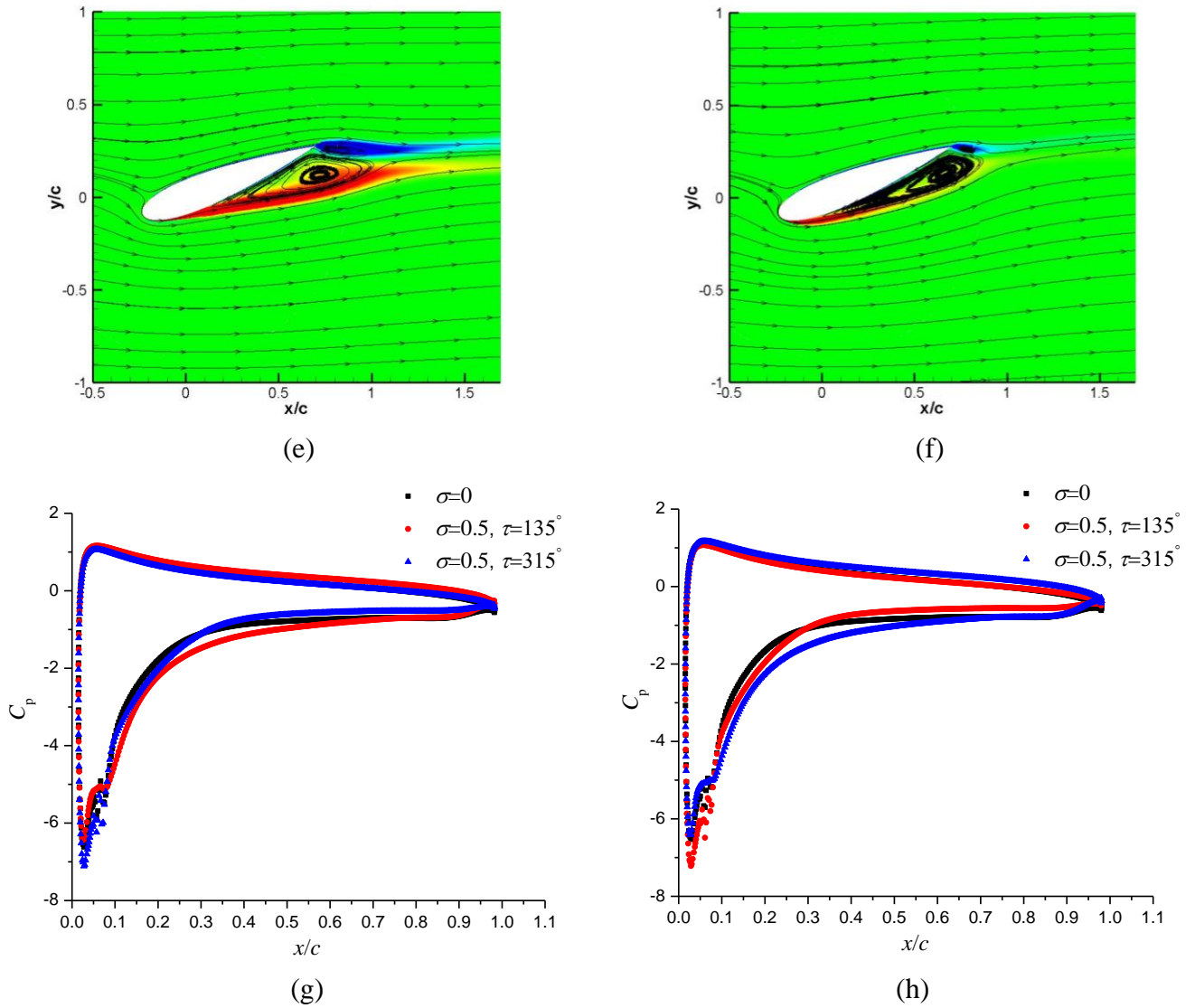
Fig.9 Spanwise vorticity contours and pressure distributions. The tested case is with the oscillation freestream of $11.1 \cdot [1 + \sigma \cdot \sin(\Phi - \tau)]$ and reduced frequency of 0.036. (a) $\sigma = 0, \Phi = 45°$; (b) $\sigma = 0.5, \Phi = 45°, \tau = 135°$; (c) $\sigma = 0.5, \Phi = 45°, \tau = 315°$; (d) $\sigma = 0, \Phi = 225°$; (e) $\sigma = 0.5, \Phi = 225°, \tau = 135°$; (f) $\sigma = 0.5, \Phi = 225°, \tau = 315°$; (g) $\Phi = 45°$; (h) $\Phi = 225°$.

In order to investigate the impact of the freestream oscillation on the laminar-turbulence transition, three different cases in figure 6, at $\Phi=18°$ and $198°$, are displayed in figure 10 using the distribution of the intermittency with the streamlines. If the intermittency is close to 1, it is turbulent flow, while it is laminar flow if the value approaches to 0. Due to the different instantaneous Reynolds number based on the freestream velocity, the morphology of the laminar separation bubble (LSB) varies considerably. For instance, when the airfoil is at $\Phi=18°$ where the freestream velocity is relatively small for the case with $\tau=135°$, the LSB length is much longer and its height is also higher. However, for the case with $\tau=315°$, the length of LSB is shorter, which is ascribed to the relatively high instantaneous Reynolds number. The change of separation, transition and reattachment points shown by the distribution of the skin friction coefficient, are presented in figure 10g and 10h. When the instantaneous Reynolds number is relatively small, the separation, transition and reattachment points move downstream, but the movement of reattachment point is more obvious. At $\Phi=198°$, the LSB shape and the skin friction distribution

for the case with τ=315° show the opposite trend compared with that at Φ=18°, as a result of the instantaneous Reynolds number based on the freestream velocity.

(a)

(b)

(c)

(d)

(e)

(f)

(g)　　　　　　　　　　　　　　　　　　(h)
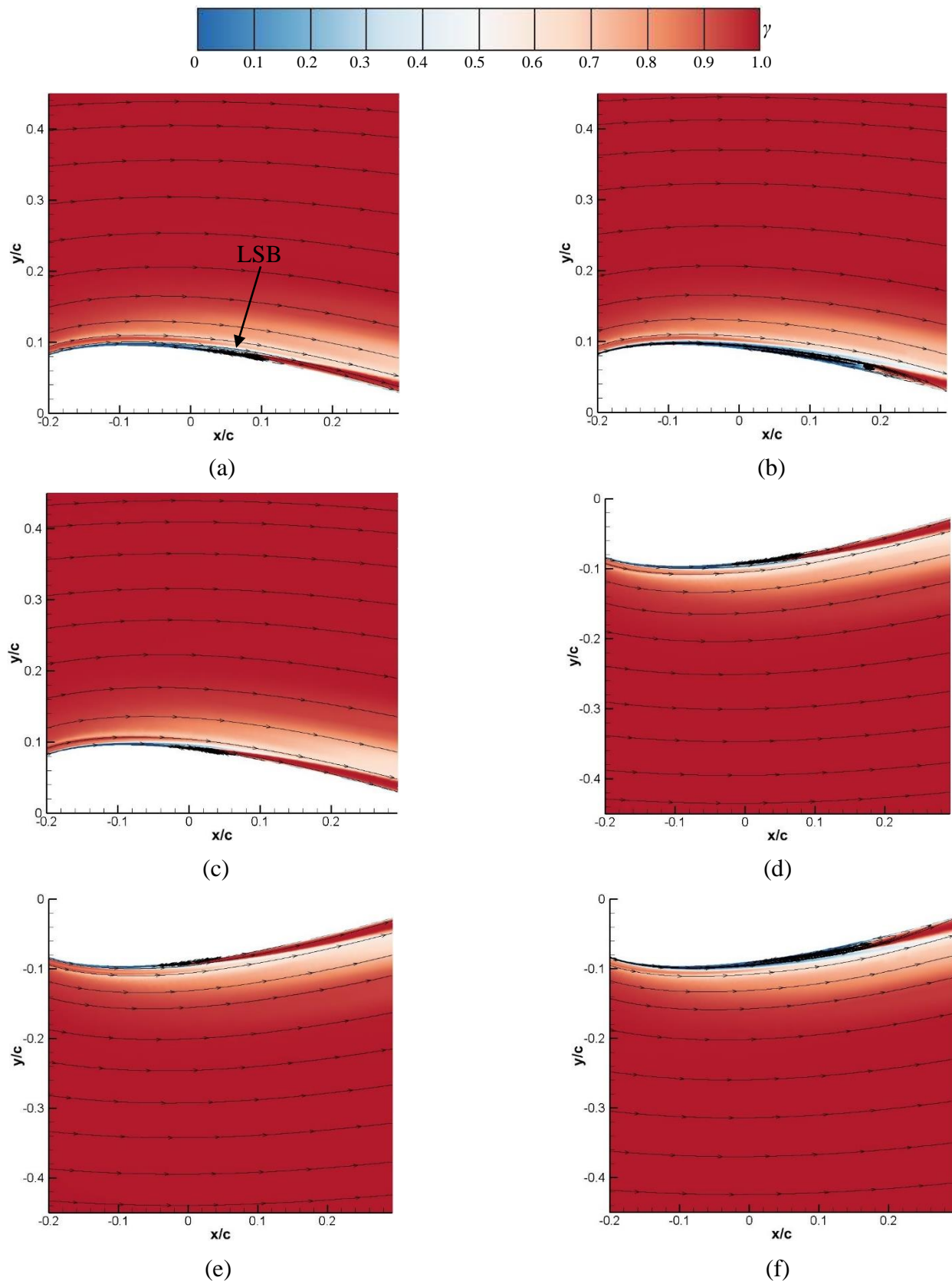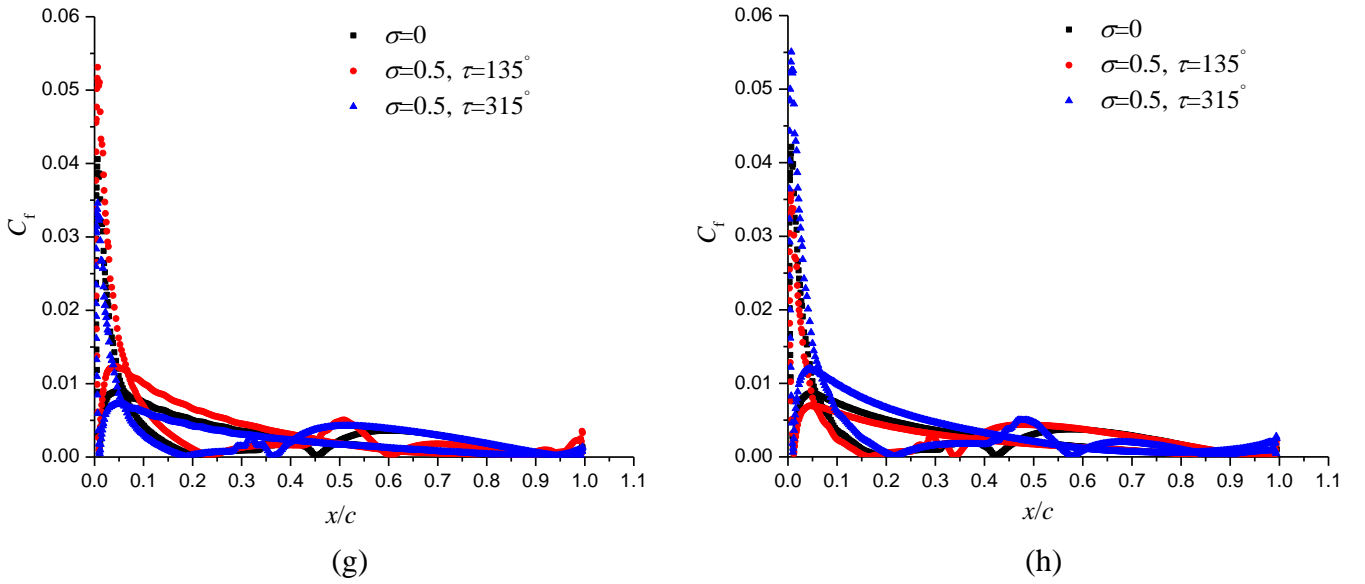
Fig.10 Laminar-turbulence transition and skin friction coefficients. The tested case is with the oscillation freestream of $11.1 \cdot [1 + \sigma \cdot \sin(\Phi - \tau)]$ and reduced frequency of 0.036. (a) $\sigma = 0, \Phi = 18°$; (b) $\sigma = 0.5, \Phi = 18°, \tau = 135°$; (c) $\sigma = 0.5, \Phi = 18°, \tau = 315°$; (d) $\sigma = 0, \Phi = 198°$; (e) $\sigma = 0.5, \Phi = 198°, \tau = 135°$; (f) $\sigma = 0.5, \Phi = 198°, \tau = 315°$; (g) $\Phi = 18°$; (h) $\Phi = 198°$.

3.2　Effect of the freestream oscillating amplitude σ

In this part, the effect of the freestream oscillating amplitude σ on the performance and flow structures around the forward and reversed airfoils are investigated systematically. The freestream oscillation function is $11.1 \cdot [1 + \sigma \cdot \sin(\Phi - 135°)]$ and the reduced frequency k_n is 0.036. As shown in figure 11a, the phase angle where the magnitude of the freestream velocity is maximal or minimal is the same for different cases, but the peak varies with the oscillating amplitude. The lift, drag and moment coefficients in a revolution are plotted in figure 11 for different oscillating amplitudes. Both for the forward and reversed airfoils, the lift peak in the upstroke increases with the oscillating amplitude. The lift and drag peak of the reversed airfoil at $\Phi=0°$-$180°$ is larger than that for the forward airfoil when σ is below 0.7. However, as σ increases to 0.9, the fluctuation of the lift, drag and moment reduces for the reversed airfoil, especially at $\Phi=180°$-$360°$. Although the freestream velocity is quite low when $\Phi=60°$, the lift coefficient is relatively low for the reversed airfoil, because of the lower lift when σ is equal to 0.9. In figure 11h, the results show that increasing σ can improve the lift coefficient, especially for the forward airfoil when σ is larger than 0.2. The improvement of the reversed airfoil performance is relatively slow, possibly caused by the massive flow separation. Additionally, the drag of the forward airfoil has a slight increase, while it decreases significantly for the revered airfoil. Based on the distribution of the moment coefficient, it is observed that it drops steeply for the reversed airfoil. In general, compared with that for the forward airfoil, the predictive performance for the reversed airfoil fluctuates a lot, especially in the range of $40°$~$160°$ and $220°$~$340°$, but it becomes much smoother with the increase of the oscillating amplitude, which is more evident in the former range as a result of the relatively low inflow instantaneous Reynolds number. Therefore, it infers that the flow structures are more complicated for the reversed airfoil and should be studied deeply.

(a)

(b)

(c)

(d)

(e)

(f)

(g)

(h)
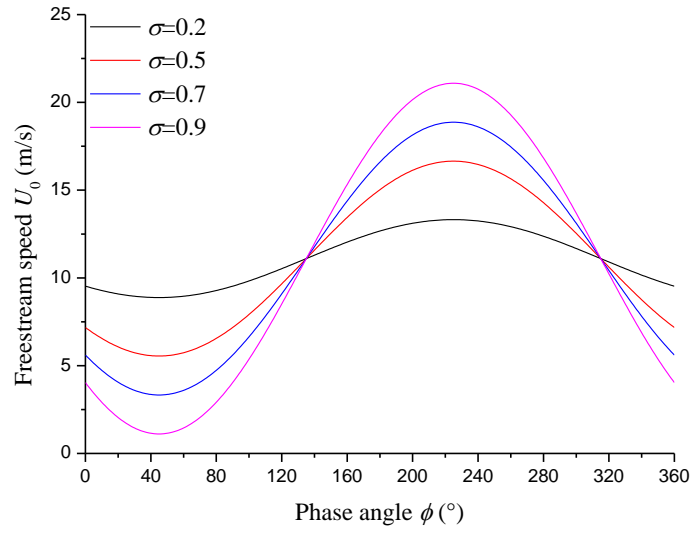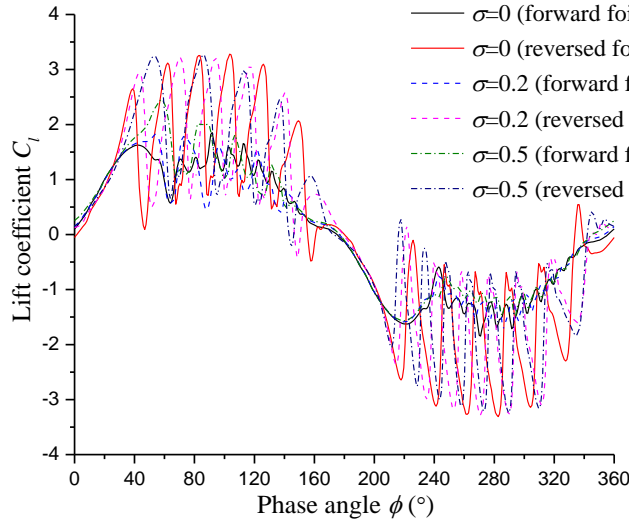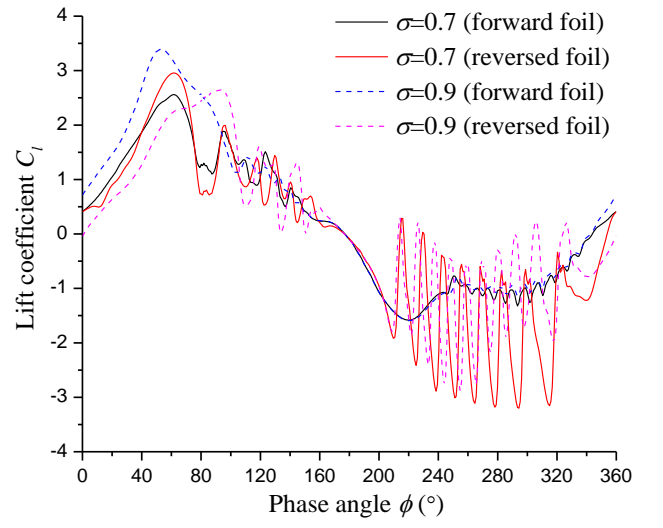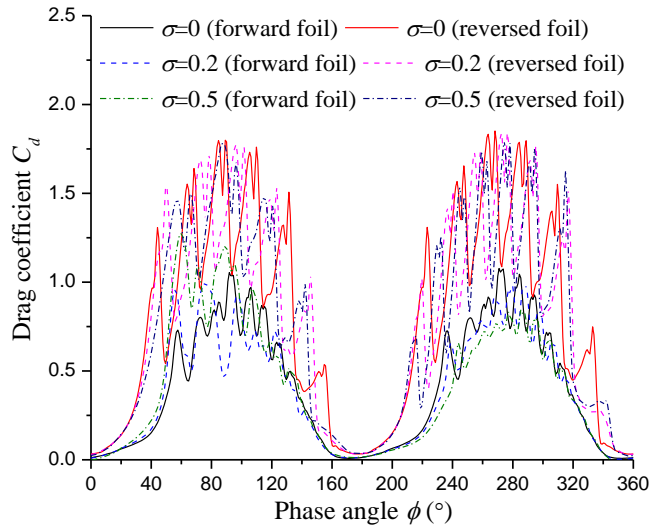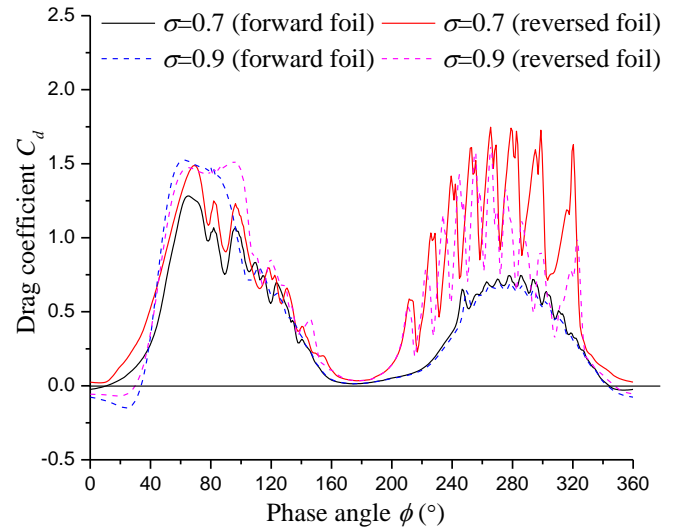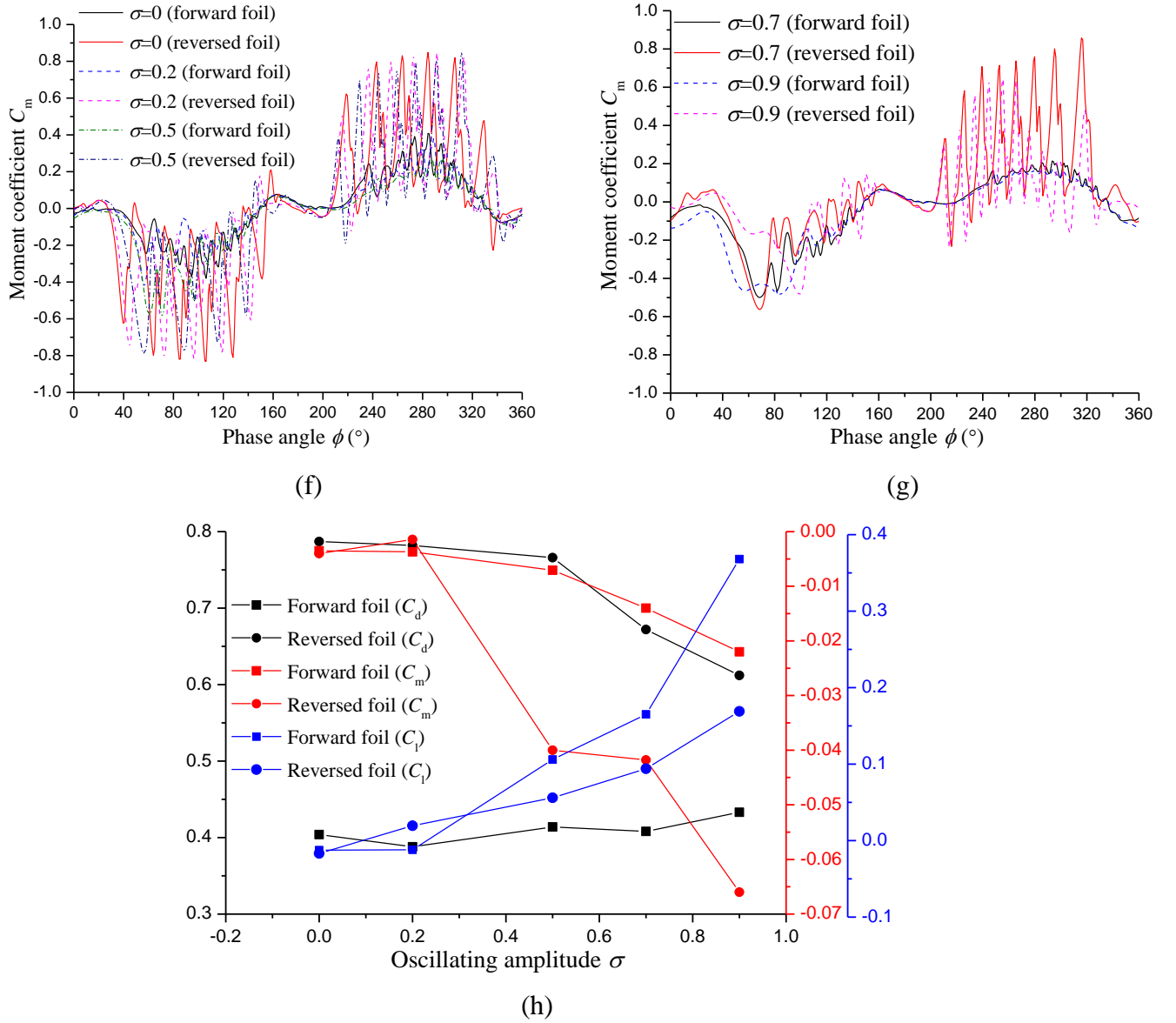
Fig.11 Performance of forward and reversed airfoils. (a) Freestream velocity variation; (b) and (c) Instantaneous lift coefficient; (d) and (e) Instantaneous drag coefficient; (f) and (g) Instantaneous moment coefficient; (h) Mean lift, drag and moment coefficients.

The flow structures, at two instants when $\Phi=45°$ and $\Phi=225°$, are displayed in figure 12 and 13 for four cases with oscillating amplitudes of 0, 0.2, 0.5 and 0.9, using the spanwise vorticity distribution coupled with the streamlines. At $\Phi=45°$, the freestream velocity has a minimal value, and the detailed vortex structures and pressure distributions are shown in figure 12. For the forward airfoil, it is observed that the large-scale LEV and TEV coexist when the oscillating amplitude σ is smaller than 0.5, but their size becomes smaller. When σ is 0.9, the TEV almost disappears. Then, when the airfoil operates in reversed mode, there is a complex vortex system for $\sigma=0$. The LEV has already shed into the wake, and the TEV attached on the trailing edge develops fully, which leads to the obvious pressure drop, as shown in figure 12i. Additionally, the secondary vortex (SV), induced by the reverse flow from the lower surface and the fluid flow around the outer edge of the LEV [5], is also evident. Influenced by the separated shear layer and the secondary vortex, the second LEV (SLEV) appear near the sharp leading edge.

With the increase of σ, the size of LEV and TEV become smaller and the LEV moves to the leading edge gradually, due to the decrease of the instantaneous Reynolds number. At $\sigma=0.9$, the intensity of vortices becomes weak and the flow structures over the reversed airfoil is more complicated. However, the weak vortical flows can alleviate the performance fluctuation in figure 11. When it comes to the vortex influence on the performance, the pressure distributions show that the LEV plays an important role in improving the performance when it is attached on the upper surface, especially for the reversed airfoil when $\sigma =0.2$ and 0.5. But the smaller size of LEV and vortices shedding into wakes cause the performance degradation for the reversed airfoil, while the LEV still maintains over the forward airfoil, leading to the relatively high performance at this moment. Consequently, it can be found that the flow structures on the reversed airfoil are more complex than that on the forward airfoil, due to the sharp leading edge resulting in the earlier massive flow separation. With the increasing of σ, the flow gradually becomes stable due to the reduction of the freestream velocity. However, at $\sigma=0.9$, the flow would be more complicated for the reversed airfoil, characterized by the vortex attached on the upper surface and the vortices shed into the wake.


(a)

(b)

(c)

(d)
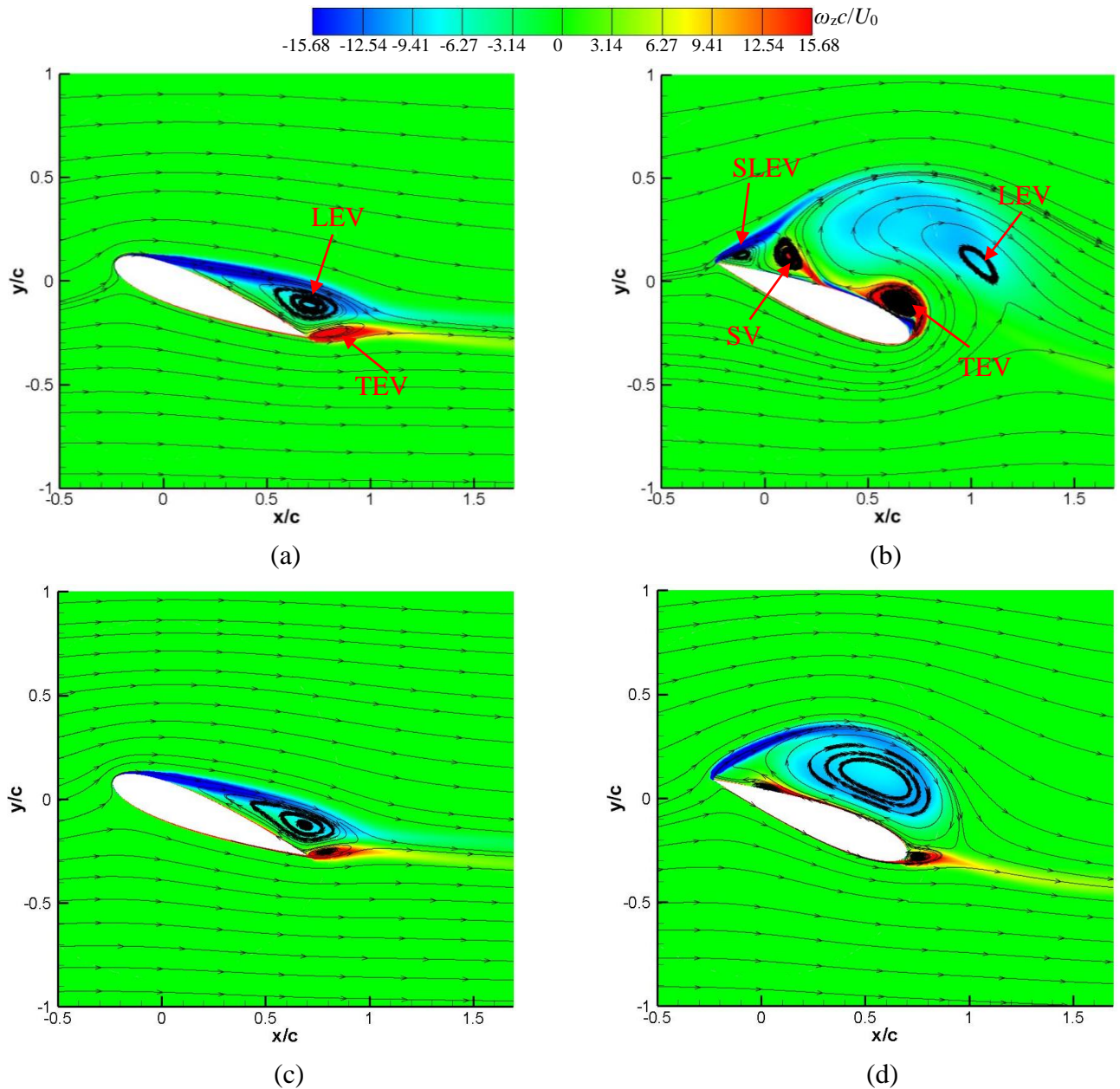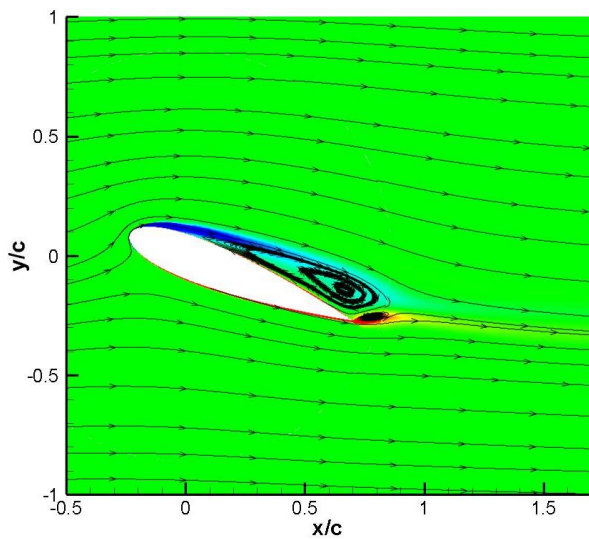
(e)
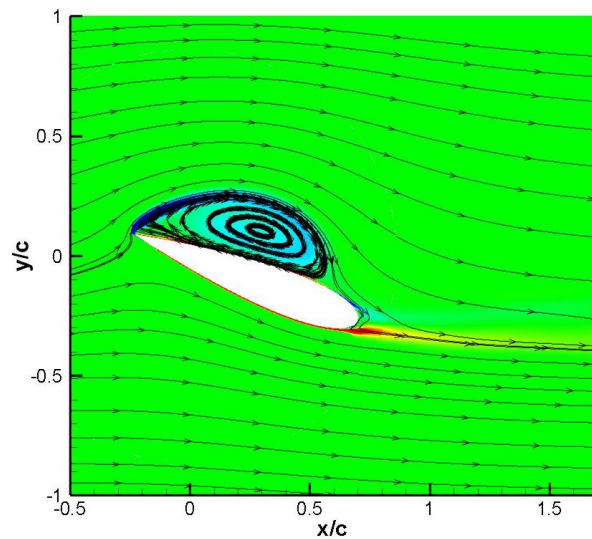
(f)
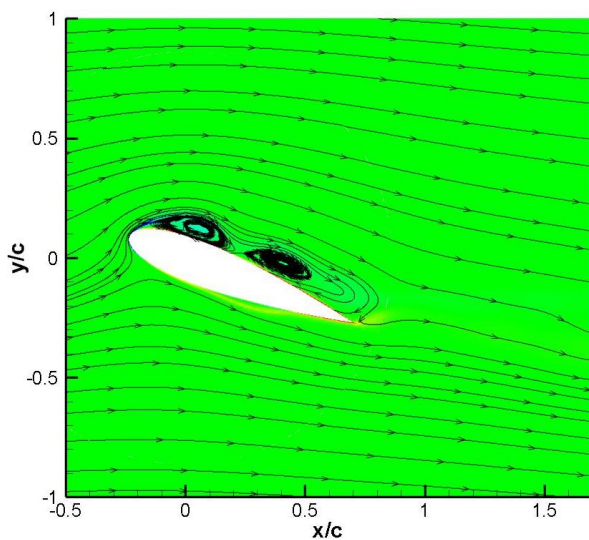
(g)
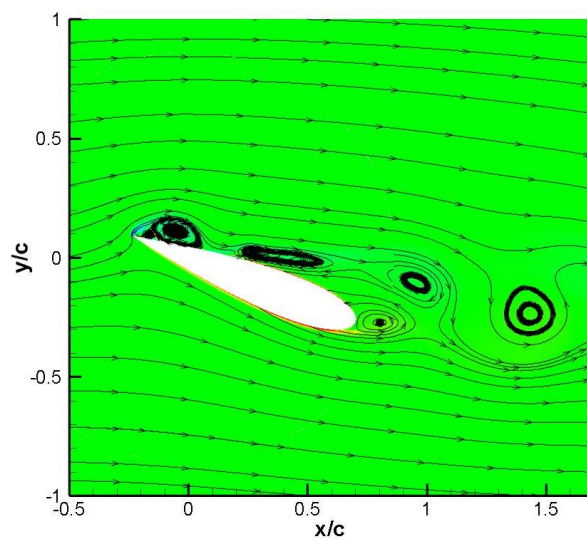
(h)
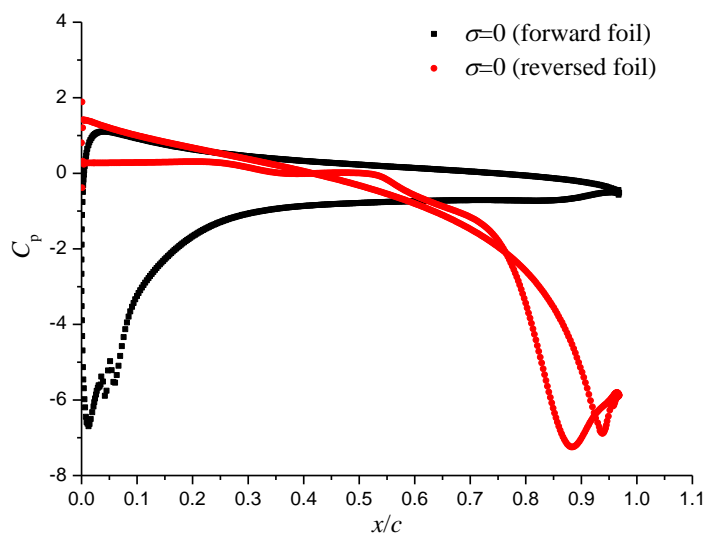
(i)
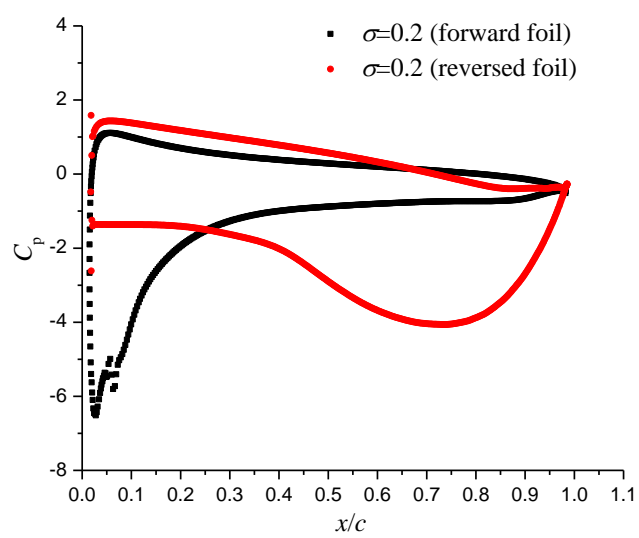
(j)
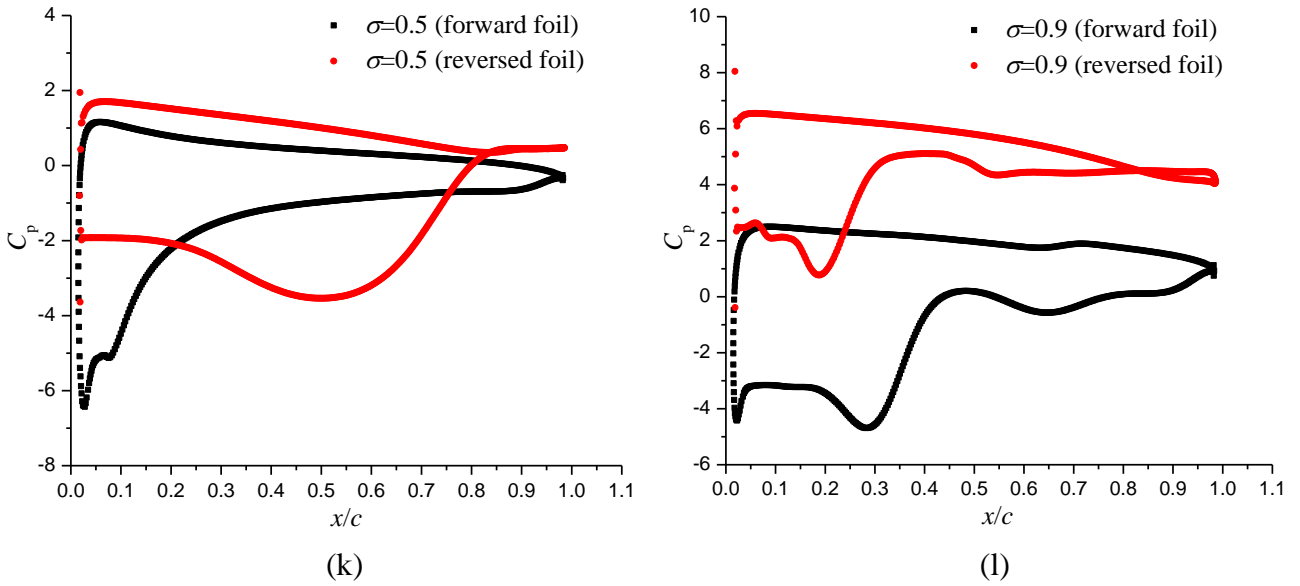
Fig.12 Flow structures and pressure distributions of forward and reversed airfoils. (a) and (b) σ=0; (c) and (d) σ=0.2; (e) and (f) σ=0.5; (g) and (h) σ=0.9; (i), (j), (k) and (l) Pressure coefficients.

Afterwards, the flow structures on forward and reversed airfoils at Φ=225° where the freestream velocity has a positive peak, are presented in figure 13. At this instant, for the forward airfoil, it seems that the flow structures are almost unchanged, but the lowest pressure in figure 11i, 11j, 11k and 11l, increases with σ. However, as σ increases, the flow filed varies considerably for the reversed airfoil. For the case with σ=0, the LEV has already disappeared in the wake, while the TEV occupies a large fraction of the blunt trailing edge. Also, the SV and SLEV emerge together with the opposite sign of the vorticity. With the increase of σ, the TEV also shed into the wake and the SLEV develops gradually. In figure 13f, it is attached on the whole upper surface nearly, leading to the large pressure difference, as shown in figure 13k, which is beneficial to the performance enhancement. Afterwards, when σ=0.9, the evolution of different vortices becomes the same with that for σ=0, which indicates that a new cycle starts. Obviously, the shedding of LEV and development of TEV result in the significant reduction of the pressure, as shown in 13i and 13l. Generally, it concludes that at Φ=225°, the increase of the freestream velocity for different cases has almost no influence on the flow structures on the forward airfoil. However, with the increase of σ, the flow structure over the reversed airfoil experiences a periodic evolution, and the pressure on the lower surface is affected remarkably by the development of different vortices.
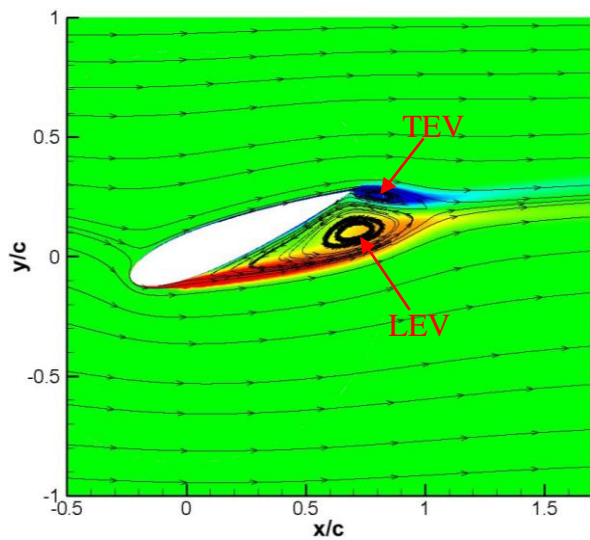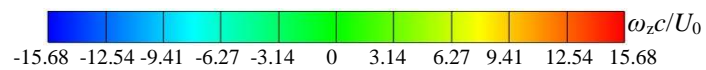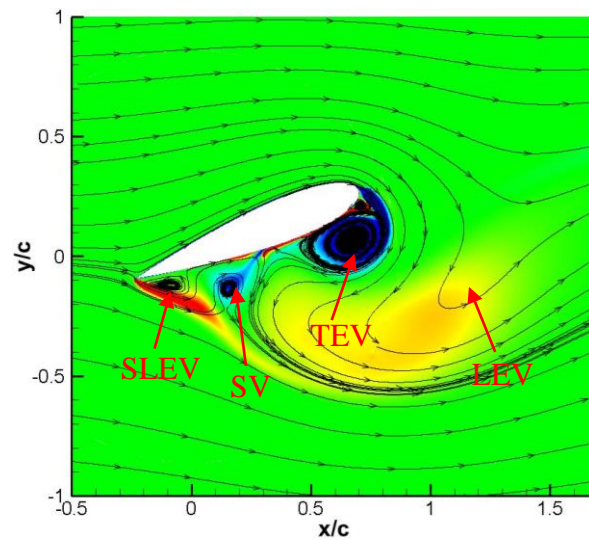
(a)   (b)
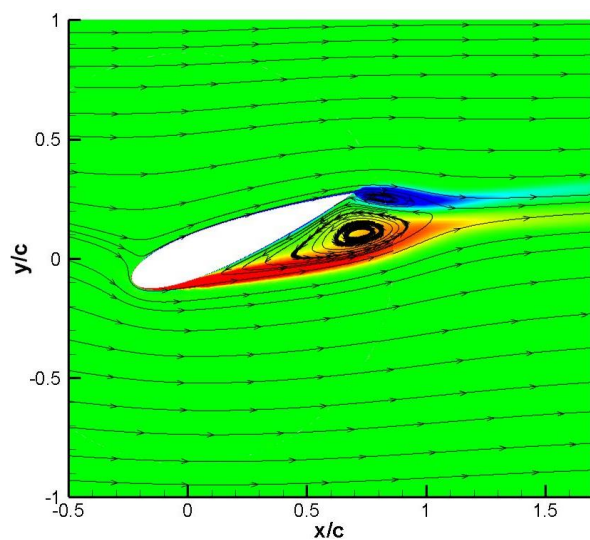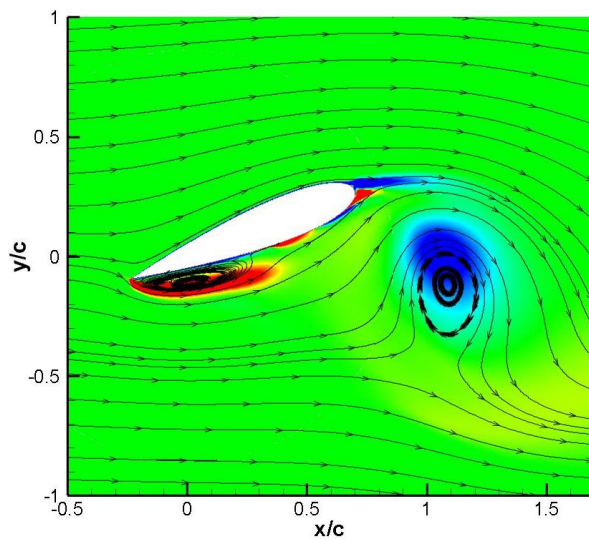
(c)   (d)
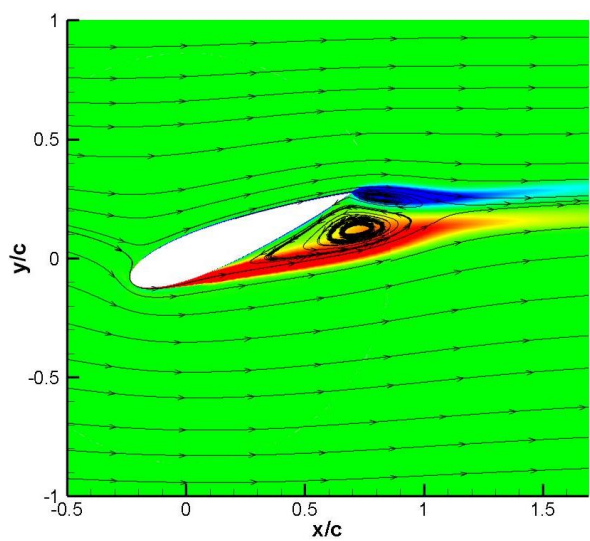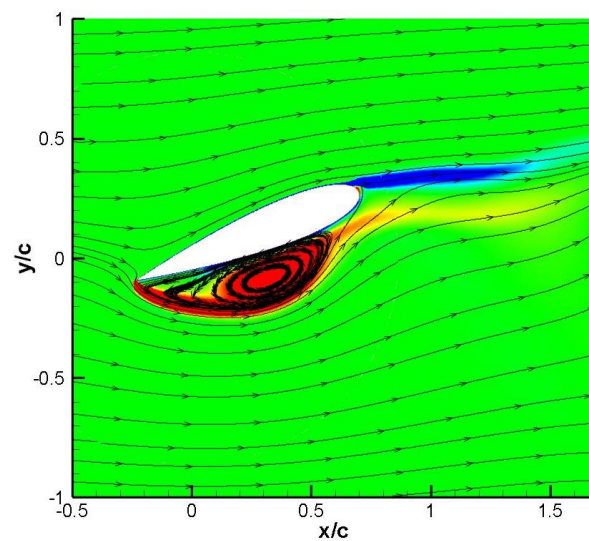
(e)   (f)
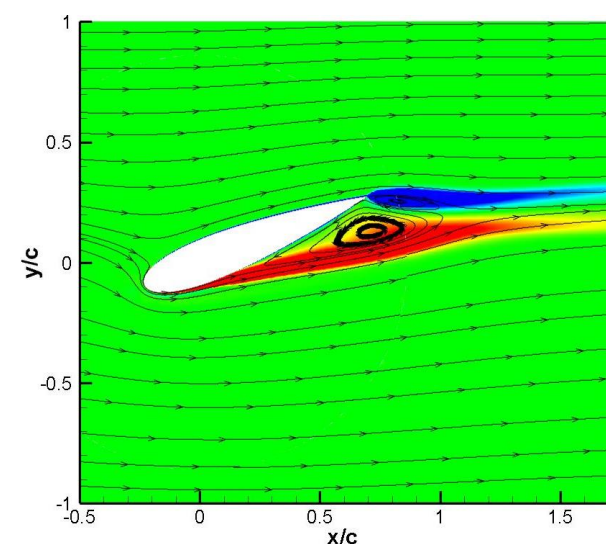
(g)
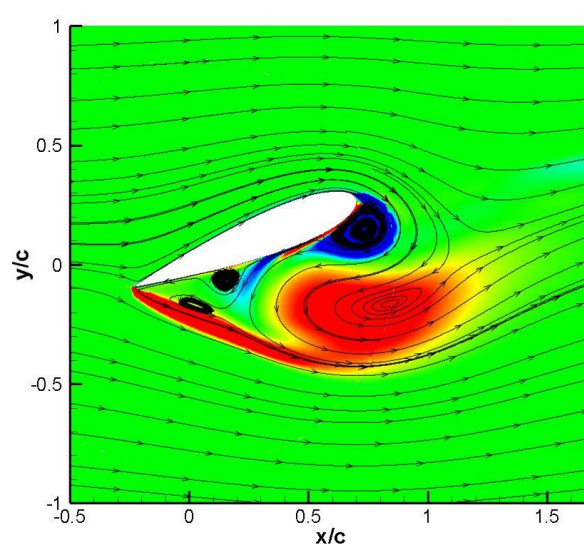
(h)
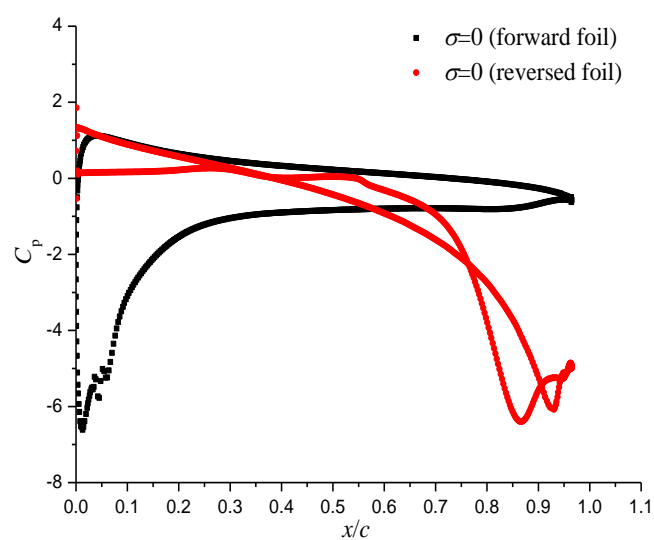
(i)
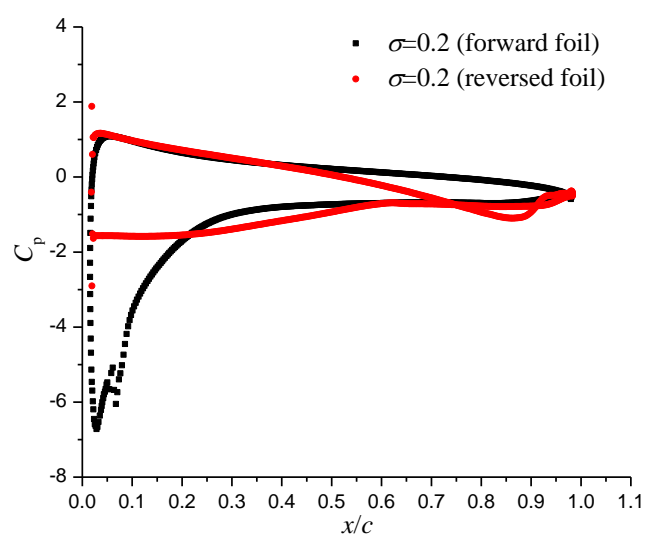
(j)
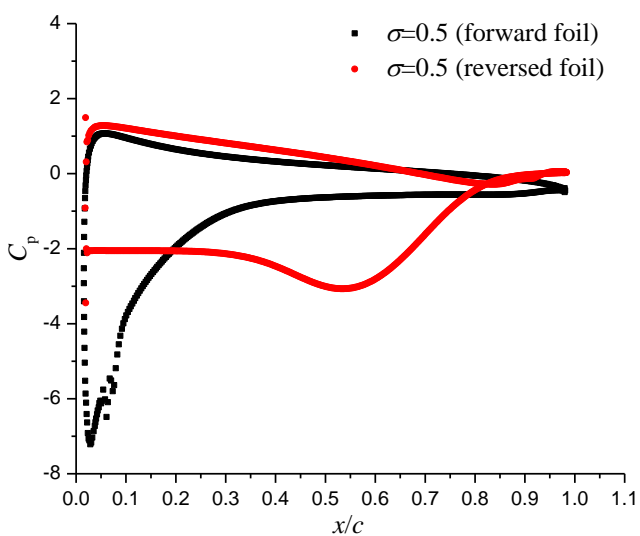
(k)
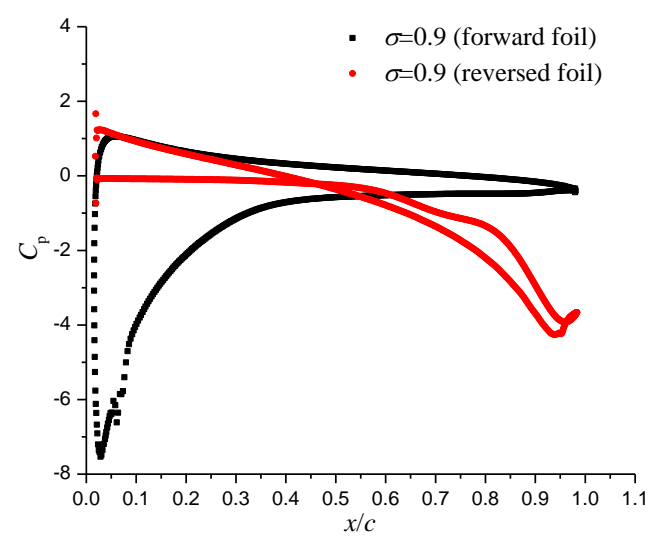
(l)

Fig.13 Flow structures and pressure distributions of forward and reversed airfoils. (a) and (b) $\sigma=0$; (c) and (d) $\sigma=0.2$; (e) and (f) $\sigma=0.5$; (g) and (h) $\sigma=0.9$; (i), (j), (k) and (l) Pressure coefficients.
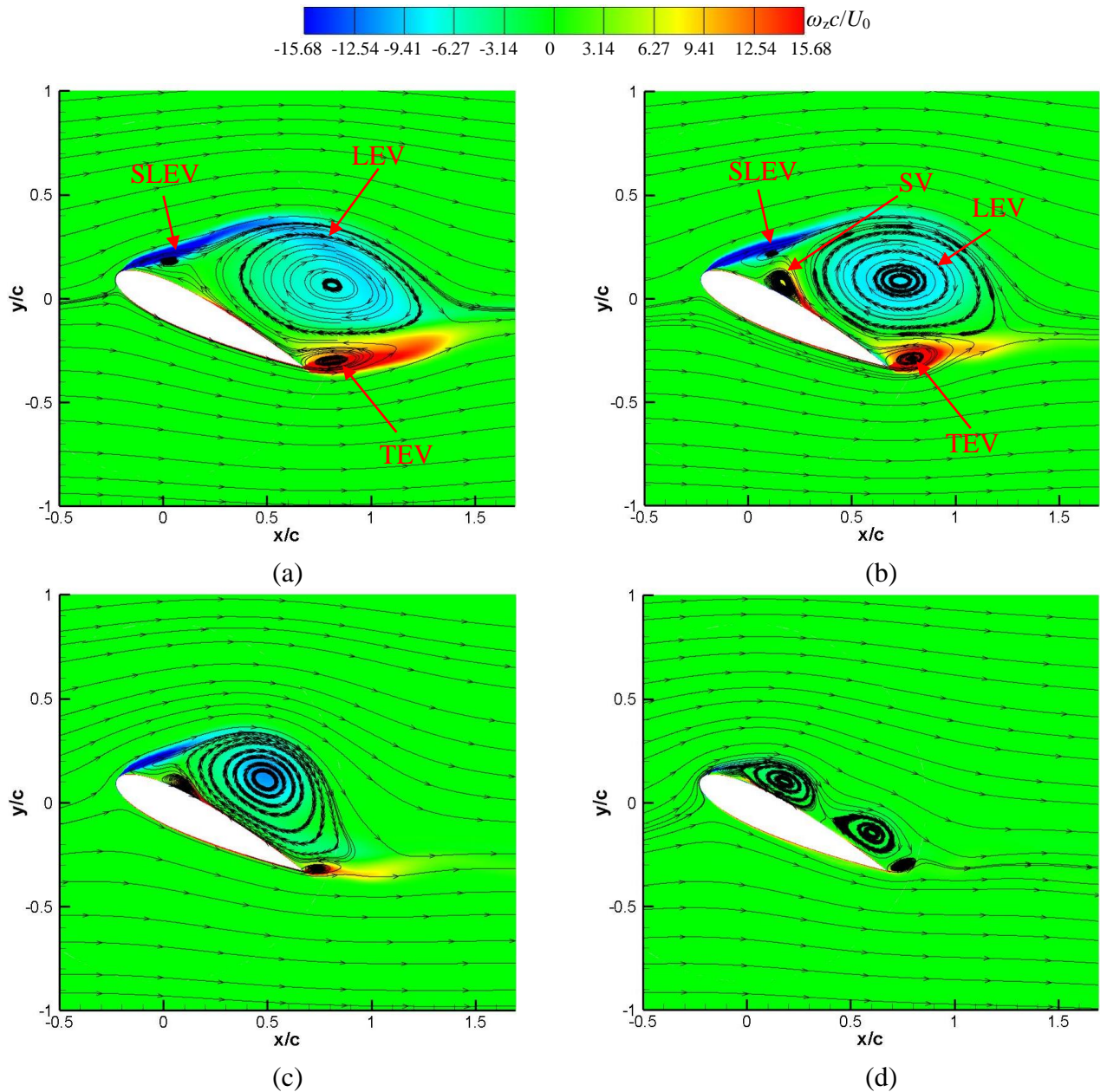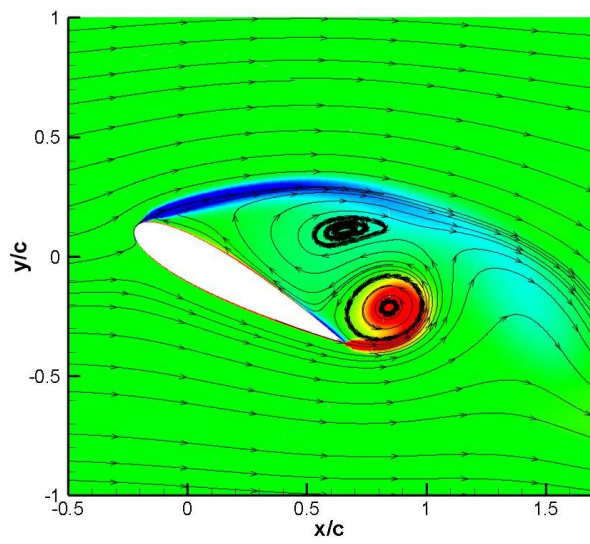
The influence of the oscillating amplitude σ on the laminar-turbulence transition at a relatively small incidence is investigated in figure 14, using the distributions of the turbulent kinetic energy and skin friction coefficient. On the upper surface of the forward airfoil, the LSB is visible and its size becomes longer with the increase of σ, mainly induced by the reattachment point moving downstream. This event results from the decrease of the freestream velocity with the increase of σ, which leads to the decrease of the Reynolds number. At $\sigma=0.9$, the separated shear layer would not reattach on the airfoil surface, as shown in figure 14l, due to the very low instantaneous Reynolds number. Simultaneously, it is observed that the transition phenomenon also exists in the middle area on the lower surface. For the reversed airfoil, the large-scale flow-separation-induced LSB makes the contribution to the transition, and its size becomes smaller with the increase of σ. Besides, it can be detected that the transition also occurs near the trailing edge of the reversed airfoil both on the upper and lower sides, which indicates that it undergoes the second transition near the blunt trailing edge. The trailing-edge transition on the reversed airfoil always mixes with the flow separation, which can increase the complexity of the wake flow and the energy loss. The difference of the transition over forward and reversed airfoils is sketched in figure 15.

(a)   (b)
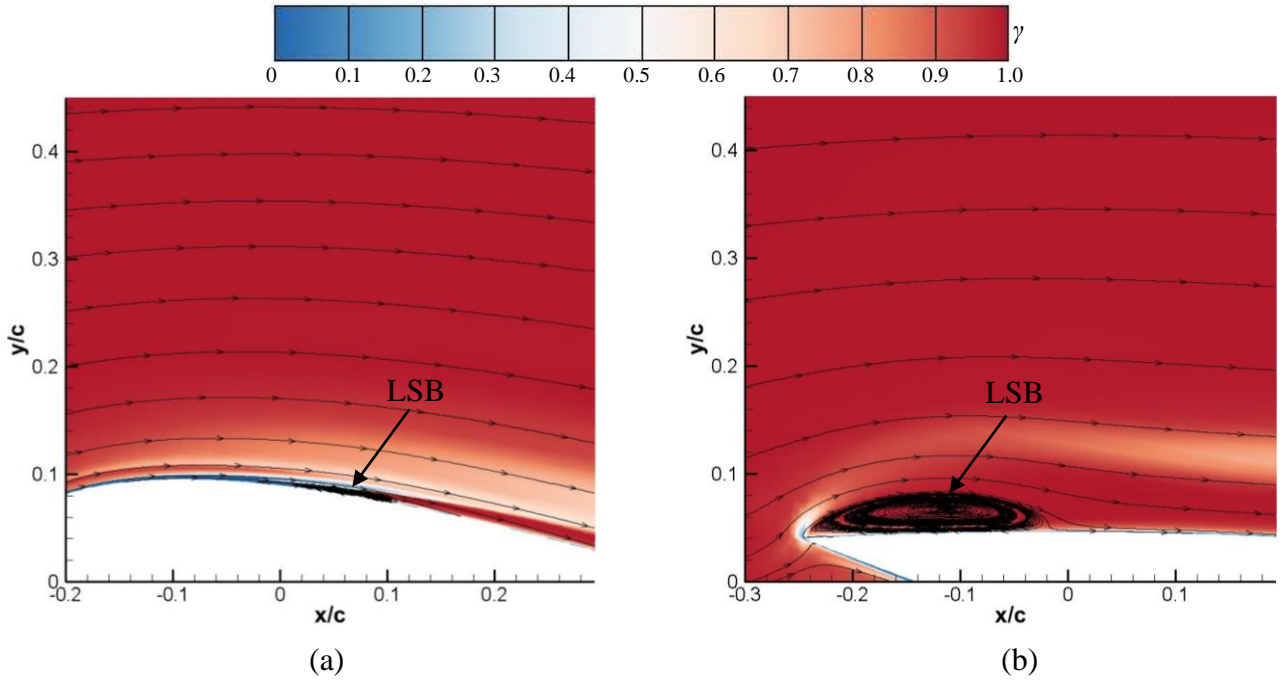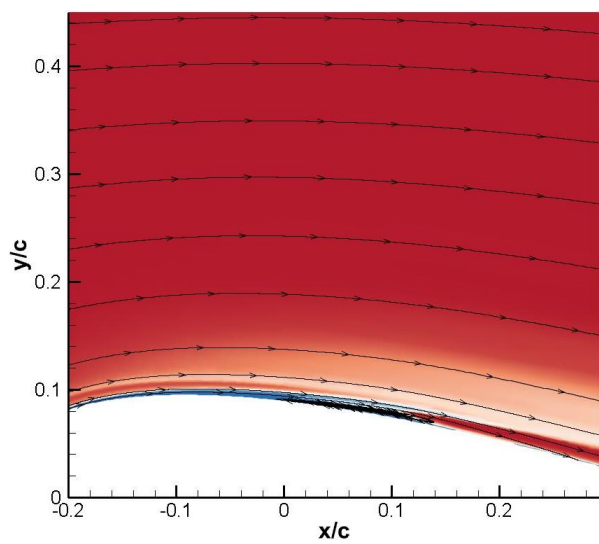
(c)
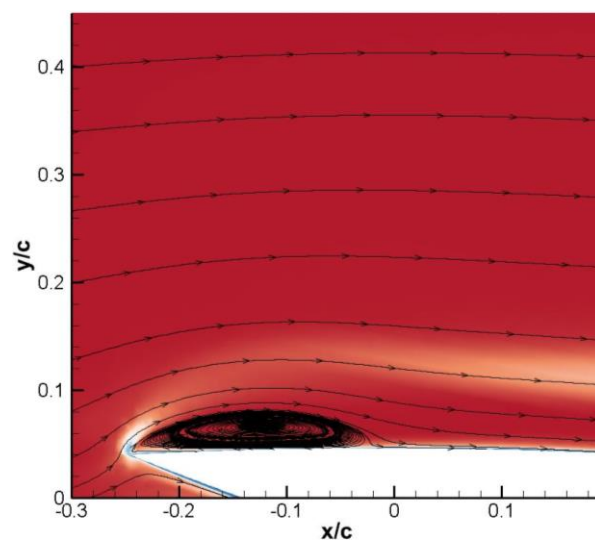
(d)
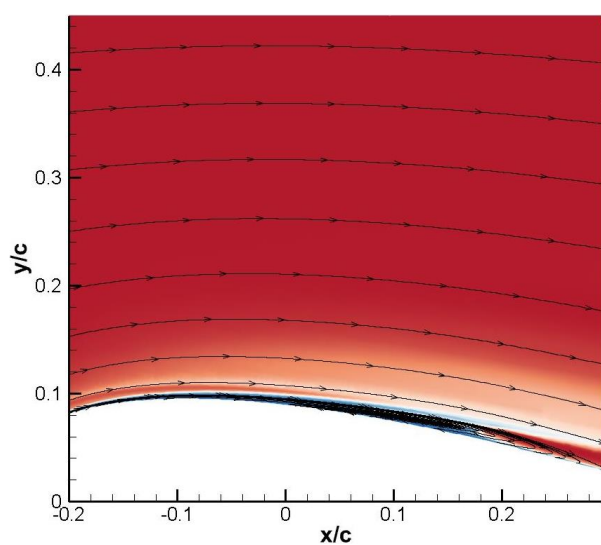
(e)
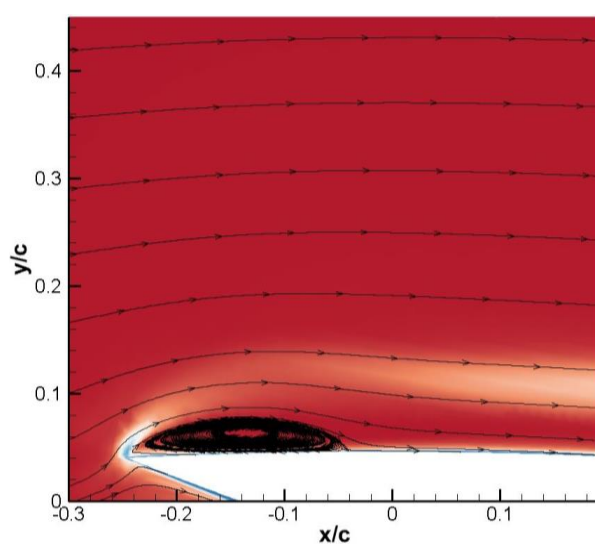
(f)
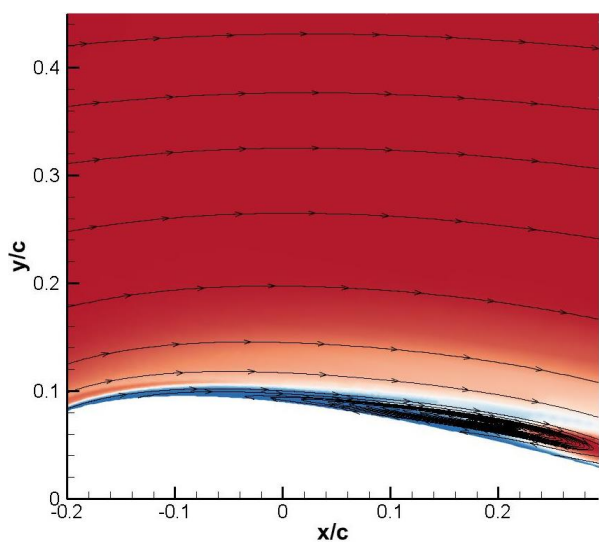
(g)
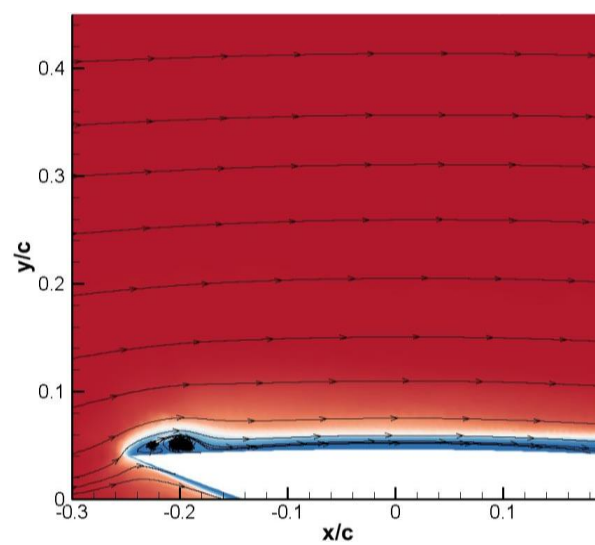
(h)
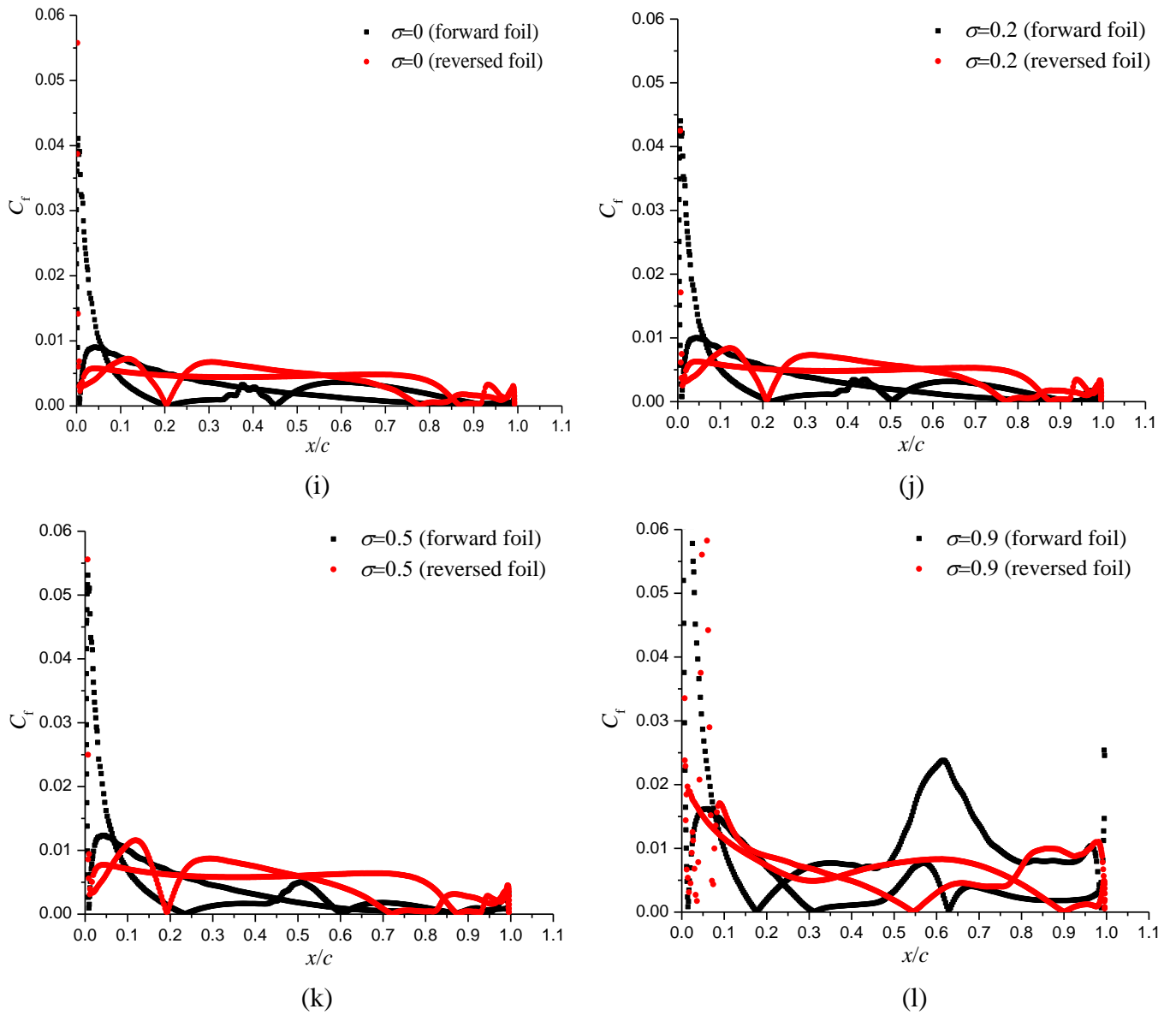
Fig.14 Transition over forward and reversed airfoils. (a) and (b) σ=0; (c) and (d) σ=0.2; (e) and (f) σ=0.5; (g) and (h) σ=0.9; (i), (j), (k) and (l) Skin friction coefficients.
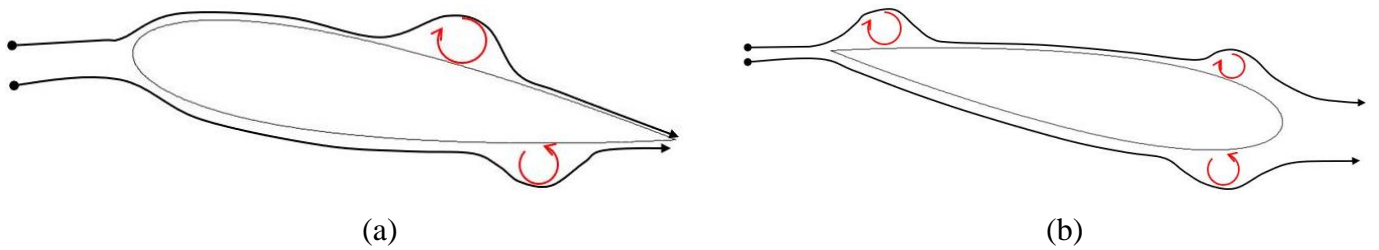
Fig.15 Sketch of the transition over two configurations. (a) Forward airfoil; (b) Reversed airfoil.

The unsteady vortical flows for different cases with oscillating amplitudes of 0, 0.2, 0.5 and 0.9 are displayed in figure 16, under dynamic stall condition. At these instants, the freestream velocity increases gradually. When σ is equal to 0, except for the large-scale LEV and TEV, a SLEV with small size is also observed in the shear layer connecting with LEV. When the incidence further increases in figure 16e, the SLEV and TEV develops fully, while the LEV has already dissipated in the wake. Then, in the next time shown in figure 16i, the third leading edge

vortex (TLEV) in the shear layer develops quickly and the TEV starts to separate. Finally, in figure 14m, the TLEV sheds into the wake and the second trailing edge vortex (STEV) re-generates in a new cycle. However, at the same instant, as σ increases to 0.2 and 0.5, the SV with the positive vorticity near the airfoil surface is evident. Simultaneously, it seems that the vortex convection speed becomes slow with the increase of σ, for a specific example, at the last time, the TLEV for the case with $\sigma=0$ has already she into the wake, while it is still attached on the upper surface. When σ is 0.9, due to the low freestream velocity, the LEV is only at the inception stage and it connects with a vortex near the trailing edge. Then, the near-wall flow in figure 16h differs from that in figure 16e, 16f and 16g, where the LEV attached on the upper surface is the main structure. Even in the last time, the SLEV and TEV are shown in the screen, which means that the flow evolution is totally delayed at low Reynolds number for the case with $\sigma=0.9$. As a result, it concludes that with the increase of σ, the flow evolution is delayed, especially for the case with $\sigma=0.9$, which is ascribed to the extremely low Reynolds number. Additionally, when $\sigma=0$, the flow structure is relatively simple, for an instance, the SV is absent, due to the large freestream velocity.
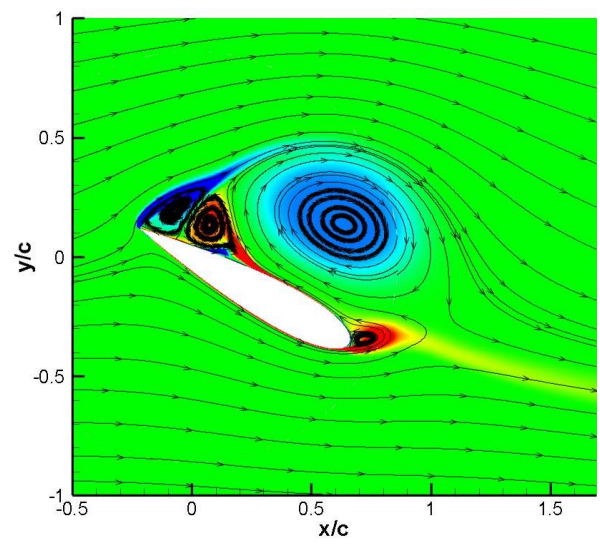
(e)

(f)

(g)

(h)

(i)

(j)
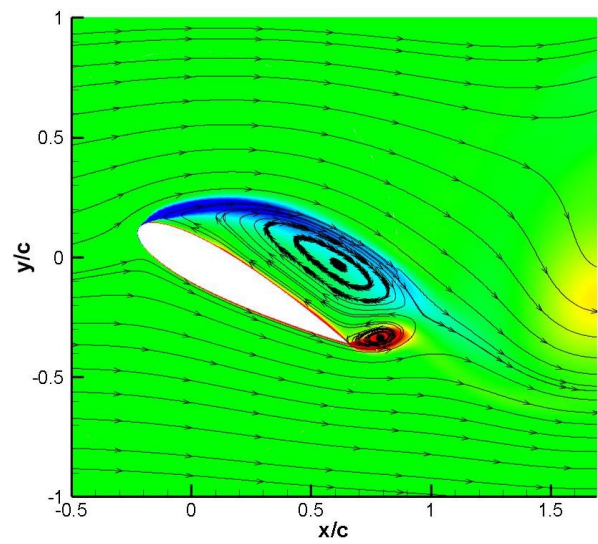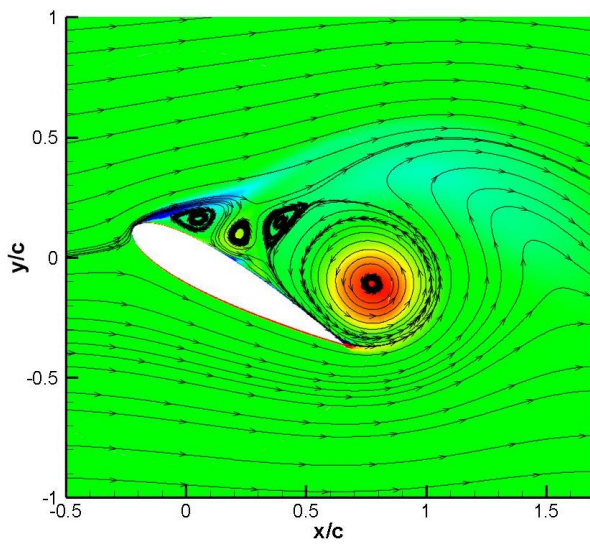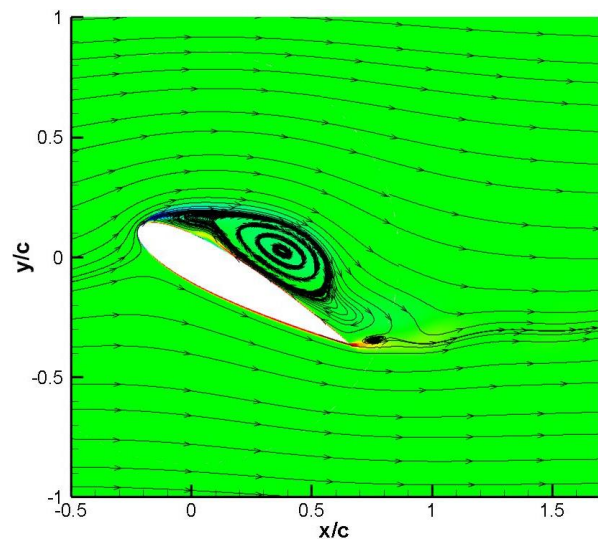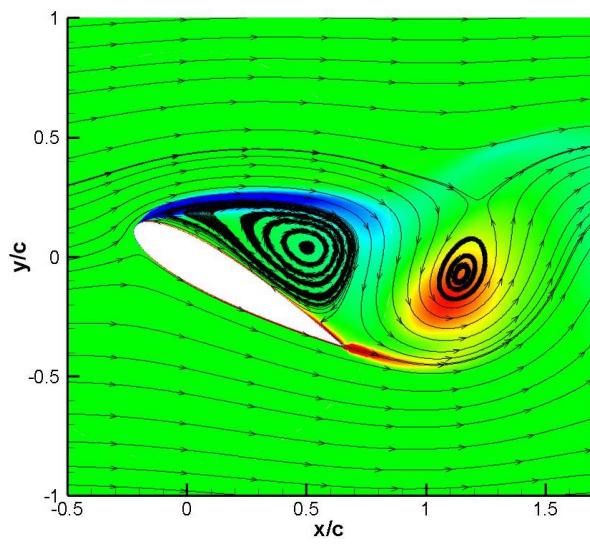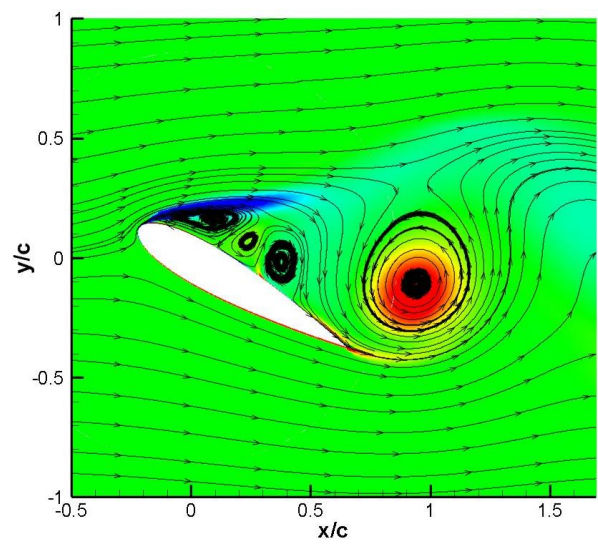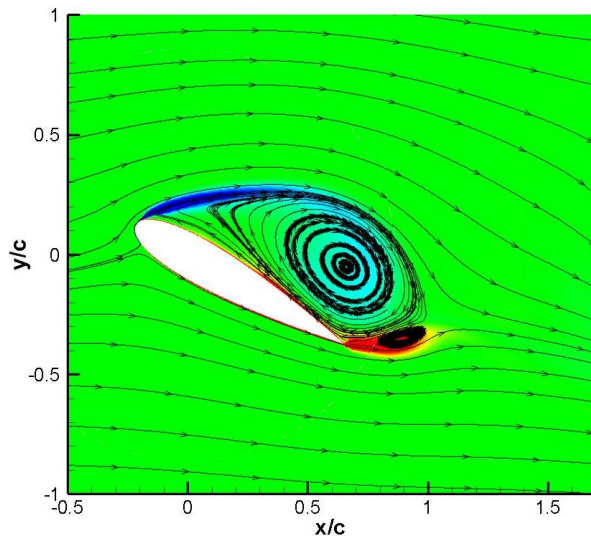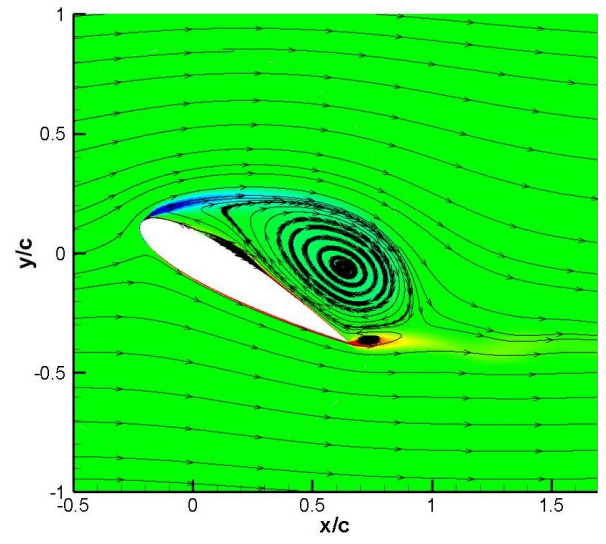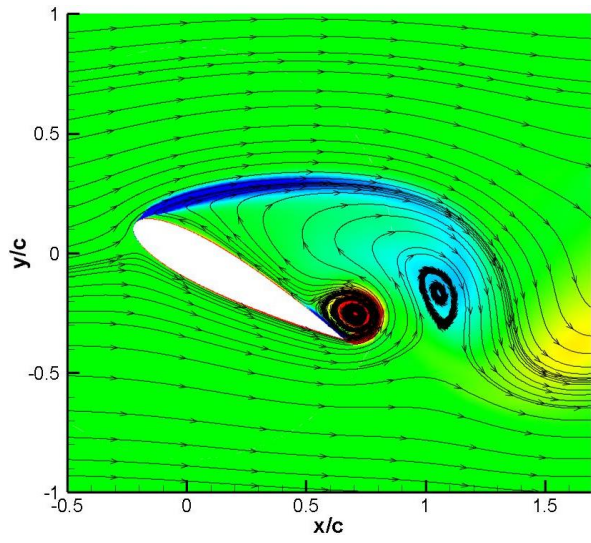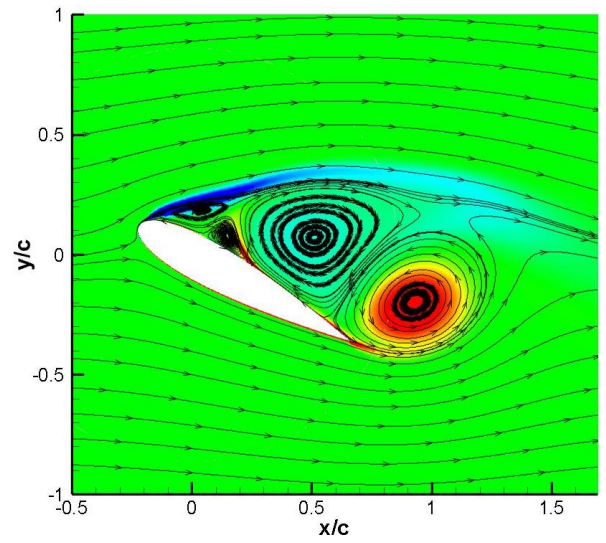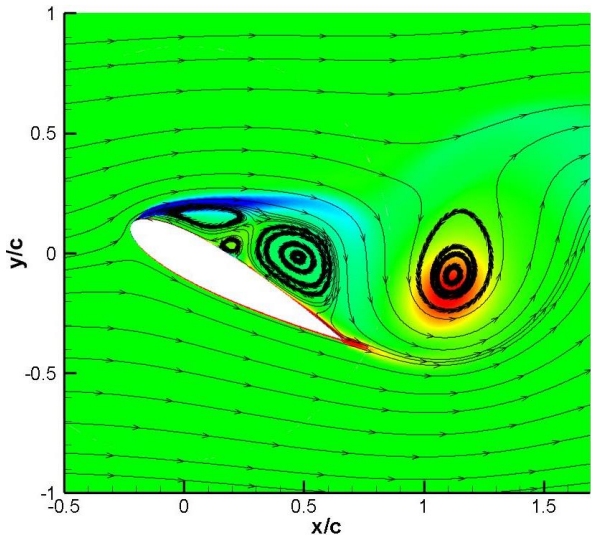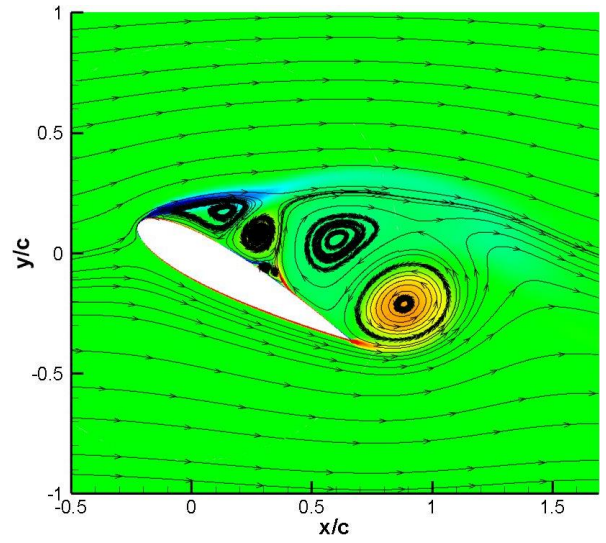
Fig.16 Unsteady vortical flows over the forward airfoil. (a), (e), (i) and (m) σ=0, Φ=60°, 75°, 90° and 105°; (b), (f), (j) and (n) σ=0.2, Φ=60°, 75°, 90° and 105°; (c), (g), (k) and (o) σ=0.5, Φ=60°, 75°, 90° and 105°; (d), (h), (l) and (p) σ=0.9, Φ=60°, 75°, 90° and 105°.

The flow structures over the reversed airfoil under different oscillating amplitude conditions are presented in figure 17. When $\sigma=0$, on the upper surface, there are LEV, SV and SLEV and the TEV has already shed into the wake. Then, at the next instant, the SLEV develops along the surface and STEV moves downstream. Further increasing the incidence to a maximal value, the TTEV, SLEV and TLEV coexist on the upper side, as shown in figure 17i. Lastly, the TTEV disappears, while the TLEV develops with the generation of the fourth leading edge vortex (FLEV). Then, with the increase of σ, the shedding TEV is still visible in the screen. Besides, the LEV shown in figure 17b is still in the development. With the further increase of σ, it seems that the flow state is in the former cycle, in which the LEV would separate while the SLEV develops. When $\sigma=0.9$, even the LEV is also at the initial stage. Compared with the flow for the case with $\sigma=0$, the LEV only appears three times and TEV occurs two times when $\sigma=0.2$ and 0.5. However, the frequency is still high than that on the forward airfoil, which indicates that the flow is more unsteady on the reversed airfoil, due to the sharp leading edge. But as σ increases to 0.9, there is no much difference about the flow structures on the forward and reversed airfoils, for the reason that the LEV, TEV, SV and SLEV emerge on the upper side in the last time simultaneously.
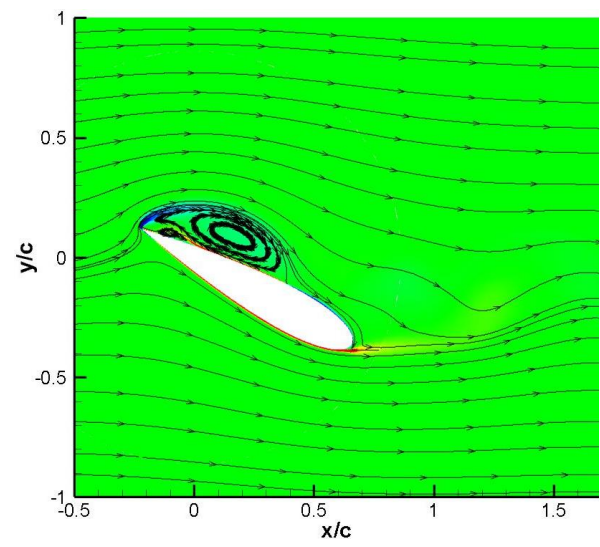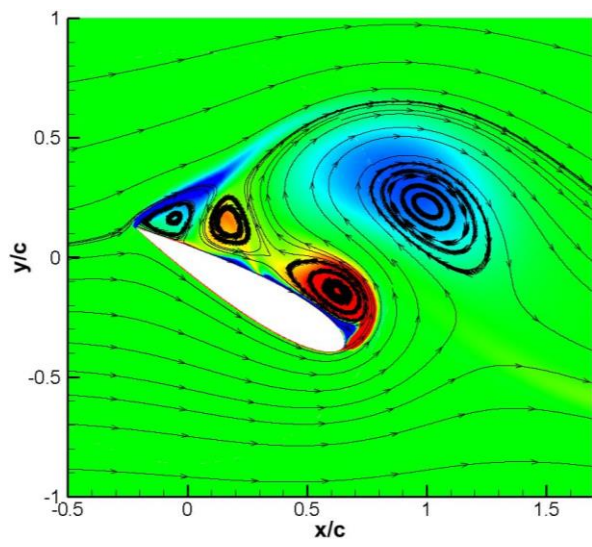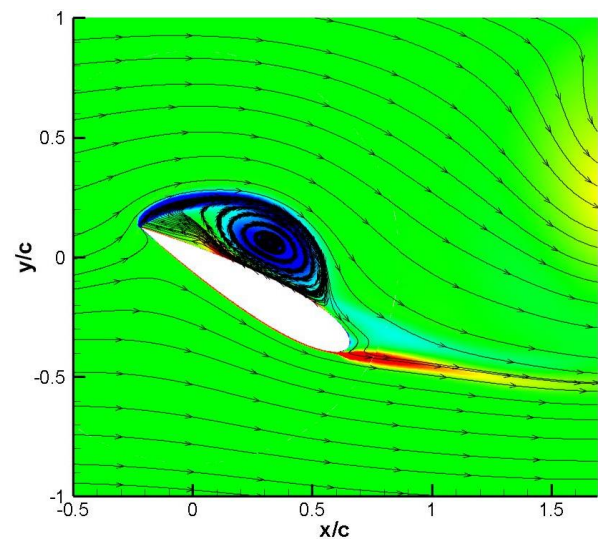

(a)

(b)

(c)

(d)
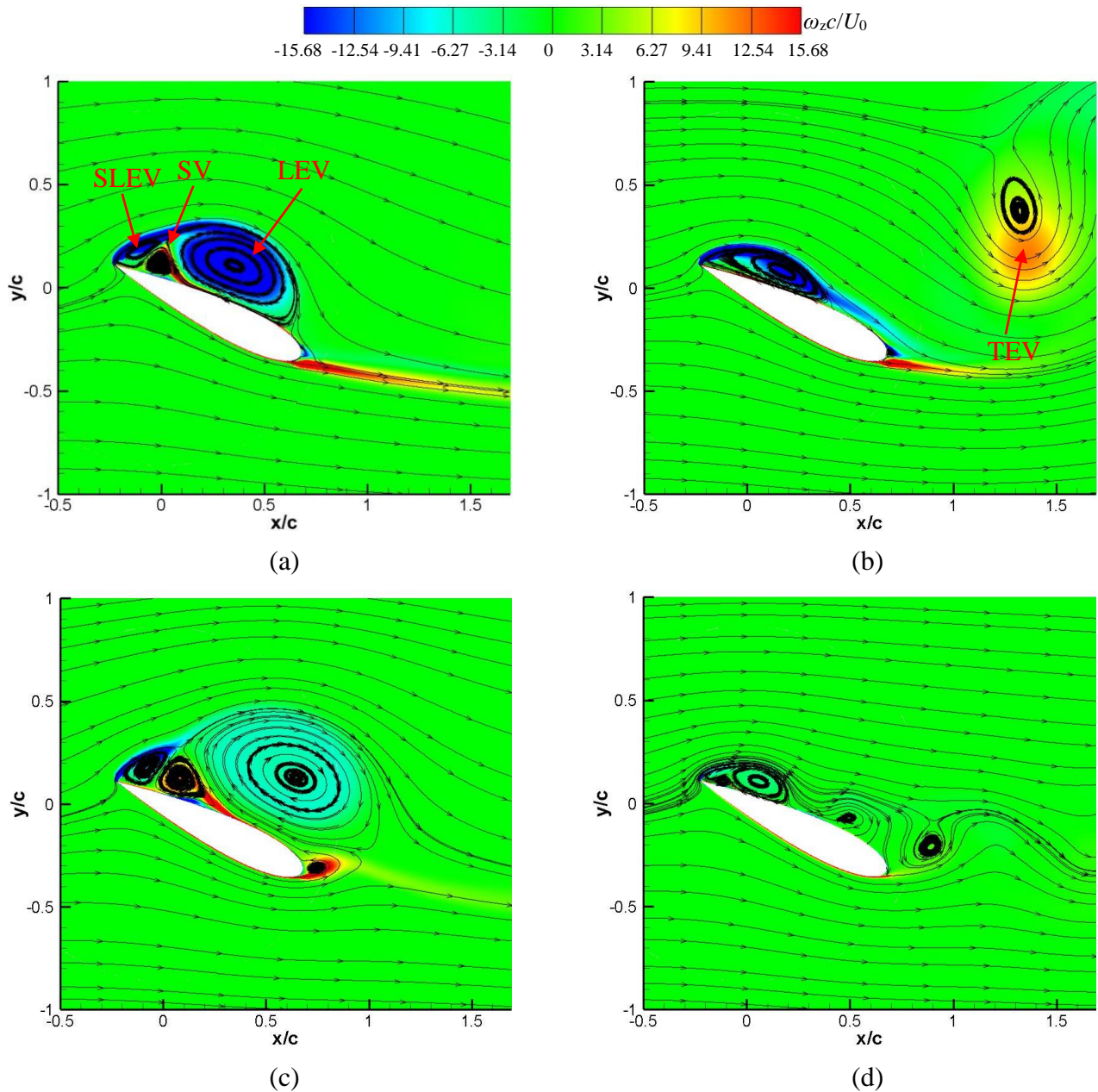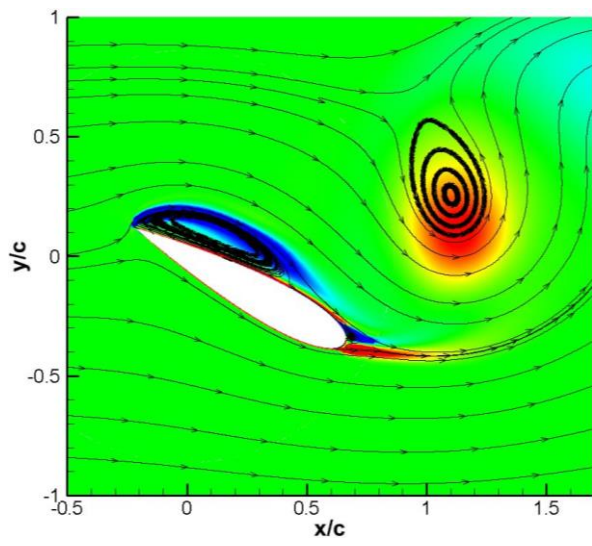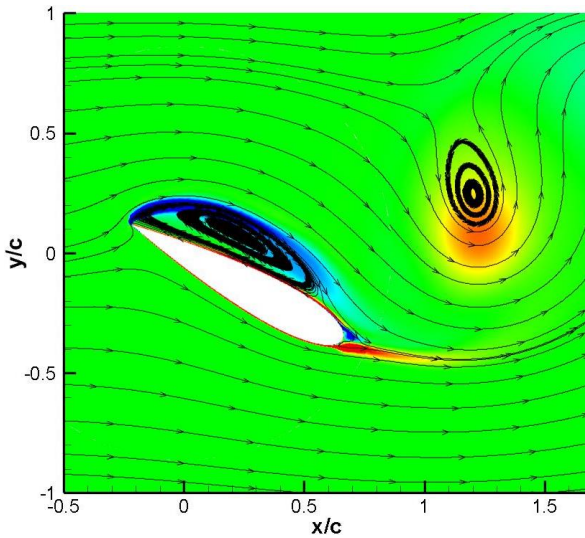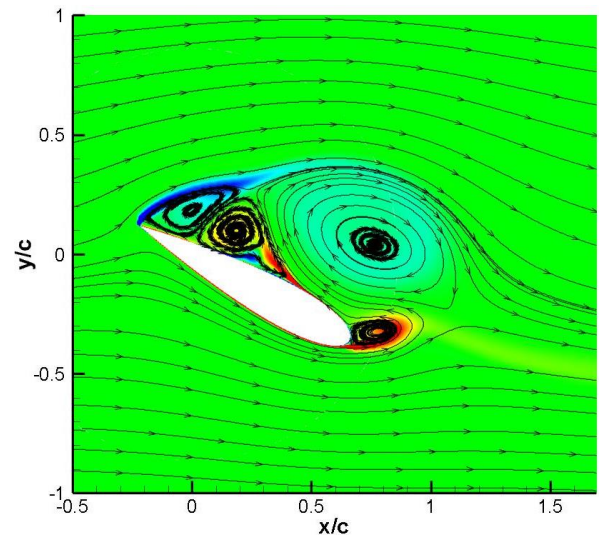
(e)

(f)
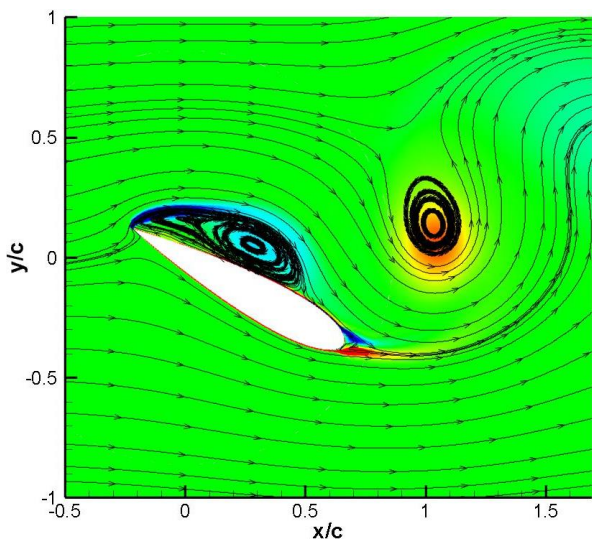
(g)

(h)


(i)

(j)
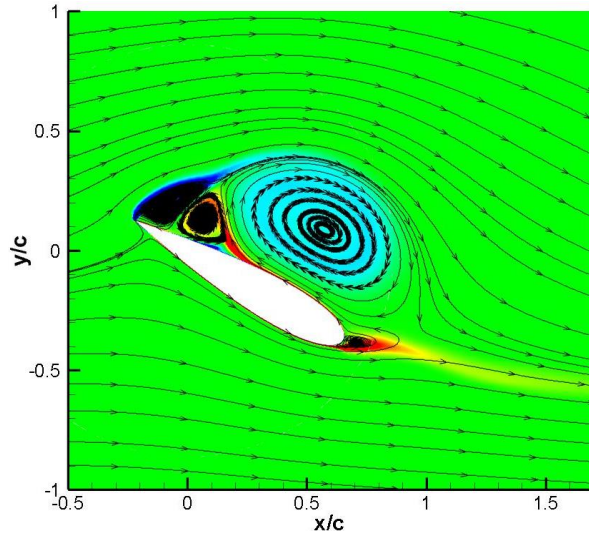
(k)
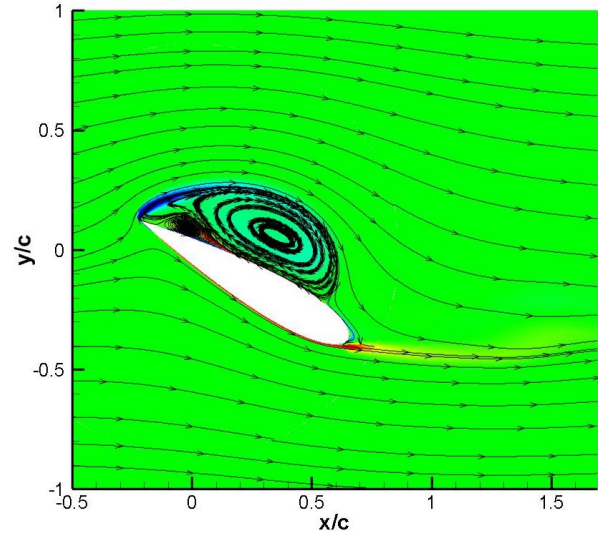
(l)
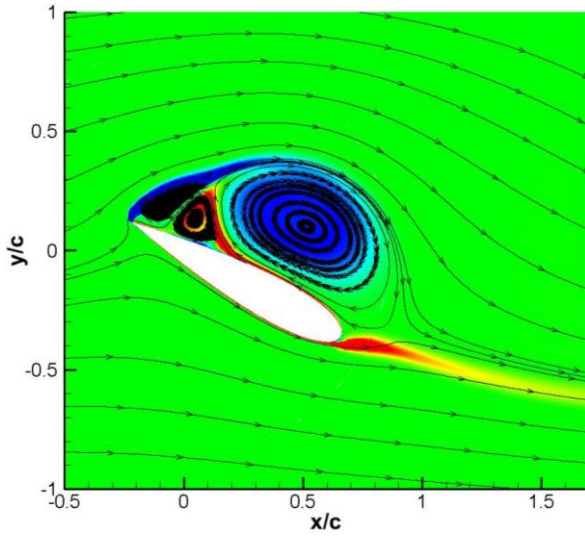
(m)
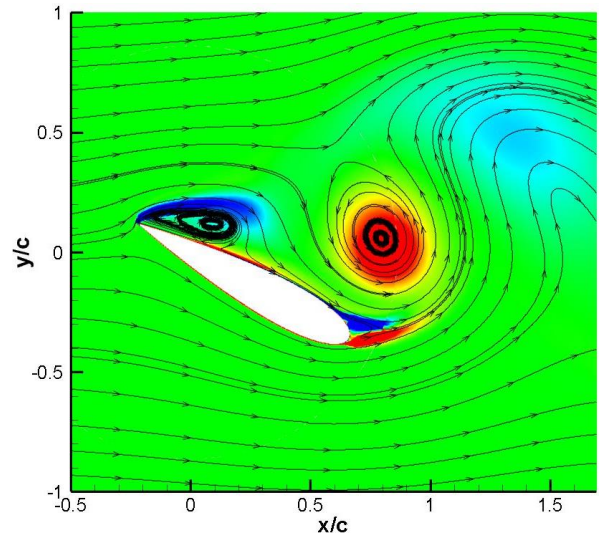
(n)

(o)

(p)

Fig.17 Unsteady vortical flows over the reversed airfoil. (a), (e), (i) and (m) $\sigma=0$, $\Phi=60^{\circ}$, 75°, 90° and 105°; (b), (f), (j) and (n) $\sigma=0.2$, $\Phi=60^{\circ}$, 75°, 90° and 105°; (c), (g), (k) and (o) $\sigma=0.5$, $\Phi=60^{\circ}$, 75°, 90° and 105°; (d), (h), (l) and (p) $\sigma=0.9$, $\Phi=60^{\circ}$, 75°, 90° and 105°.

### 3.3   *Effect of the mean reduced frequency k_n*

In this section, the influence of the mean reduced frequency k_n on the performance and vortex dynamics is studied in detail. The instantaneous and time-averaged lift, drag and moment coefficients of forward and reversed airfoils are plotted in figure 18. The tested case is with the freestream oscillation of $11.1 \cdot [1 + 0.5 \cdot \sin(\Phi - 135^\circ)]$. Both for the forward and reversed airfoils, the lift peak is delayed, especially at large reduced frequency. It is observed that at k_n=0.02 for both two configurations and at k_n=0.036 for the forward airfoil, the lift coefficient has a relatively large fluctuation at Φ=40°-160°, compared with that at Φ=200°-320°. However, when k_n is 0.036 for the reversed airfoil, it seems that there is also a large fluctuation of the lift coefficient at Φ=200°-320°. Simultaneously, with the increase of k_n, both the fluctuations in these two regions are reduced. In general, the fluctuation of the performance for the reversed airfoil is still larger than that of the forward airfoil. In figure 18g, it shows that the mean lift coefficient of the forward airfoil increases initially and then has a slight decrease at k_n=0.144. On the contrary, the mean lift coefficient of the reversed airfoil at k_n=0.02 is a little bit larger than that of the forwards airfoil, mainly induced by the lift variation at Φ=200°-320°, as shown in figure 18a. Then, after that, the lift coefficient decreases dramatically. The moment coefficient also increases with k_n, but the increase rate is relatively large for the reversed airfoil. When it comes to the drag coefficient, it can be seen that the magnitude of the reversed airfoil is much larger than that of the forward airfoil.
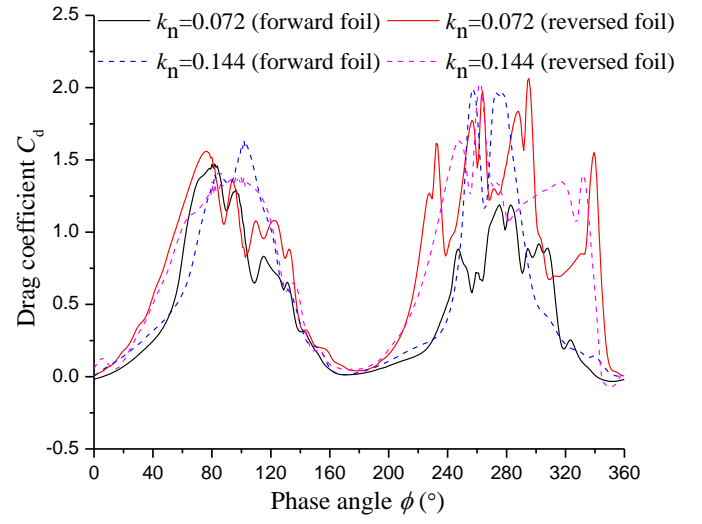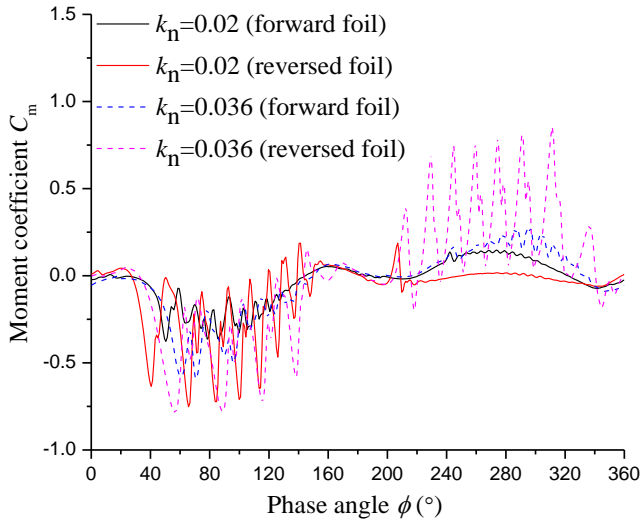

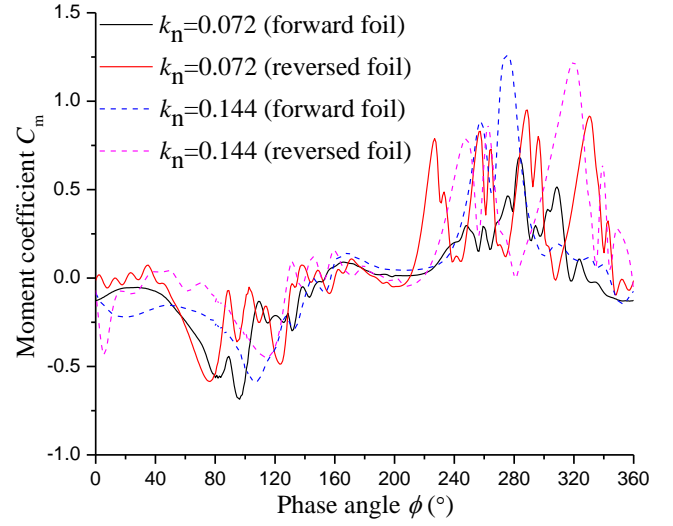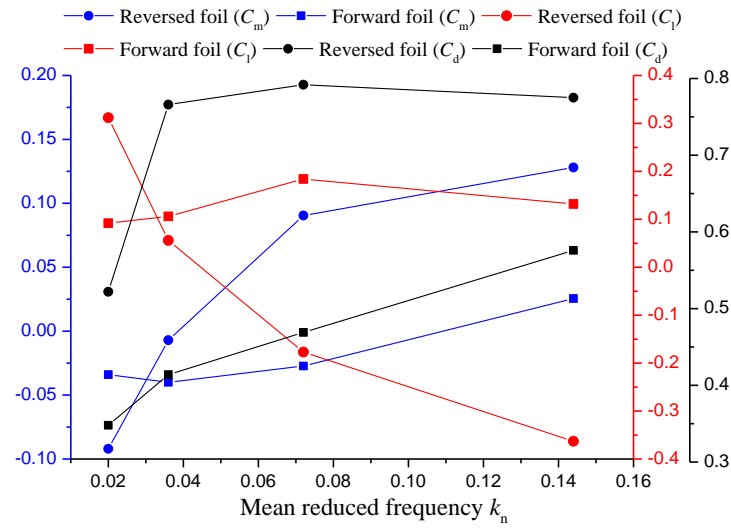(a)   (b)
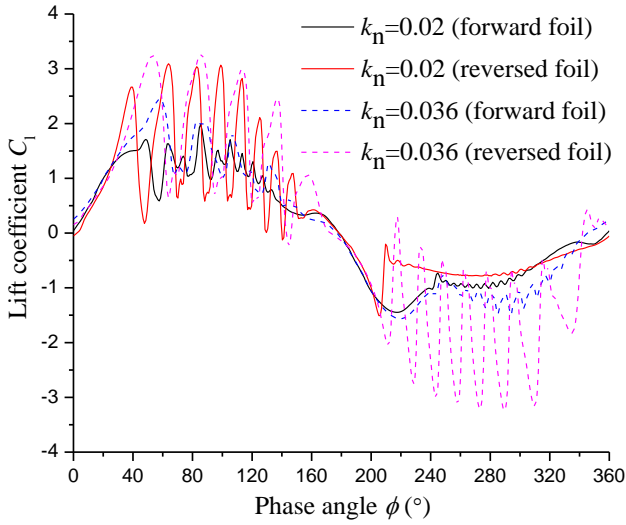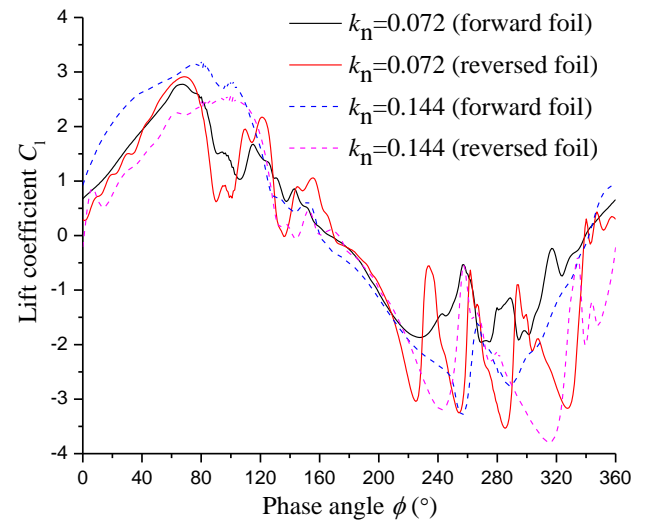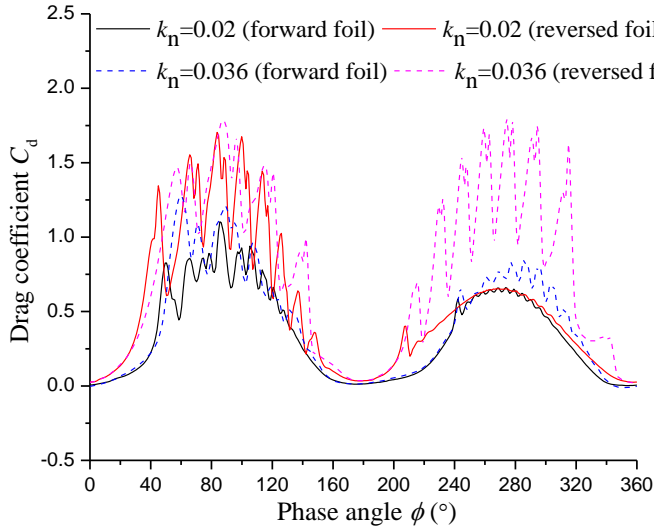
Fig.18 Performance of forward and reversed airfoils. (a) and (b) Instantaneous lift coefficient; (c) and (d) Instantaneous drag coefficient; (e) and (f) Instantaneous moment coefficient; (g) Mean lift, drag and moment coefficients.

Then, the flow structures over forward and reversed airfoils at two instants when the freestream velocity has the minimal and maximal magnitudes, are shown in figure 19 and 20, at four k_n. Figure 19 presents the spanwise vorticity and pressure distributions at $\Phi=45°$. At low reduced frequency, the existence of LEV and TEV is observed, but they disappear gradually with the increase of k_n. For the reversed airfoil, the flow field is more chaotic compared with that on the forward airfoil. The LEV has already separated from the upper surface when k_n is 0.02, and there are three main vortex structures remaining on the upper side, including the SLEV, SV and TEV. The shedding of LEV and development of TEV have much influence on the pressure distribution, as shown in figure 19i. With the increase of k_n, the flow structure near the airfoil surface is delayed. For example, in figure 19b, the LEV has already shed into the wake, but it is still attached on the upper surface under the development condition in figure 19d. In figure 19h, it is in the initial time near the sharp leading edge. Moreover, based on the flow structure, it is observed that the low-pressure region induced by LEV over the upper surface moves to the leading edge, which is shown in figure 19i and 19j.
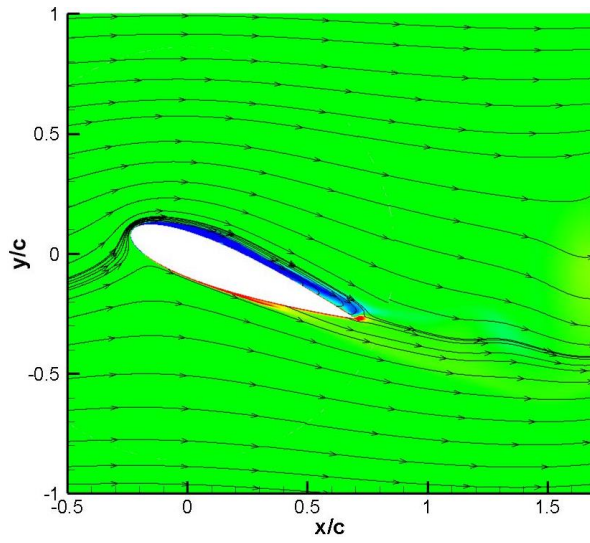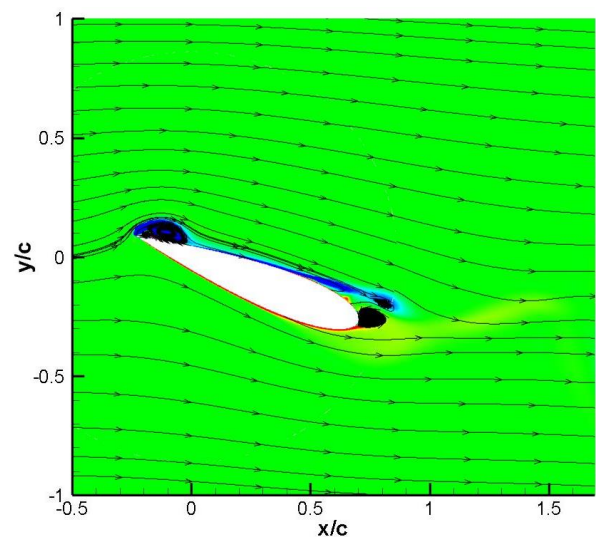

(a)
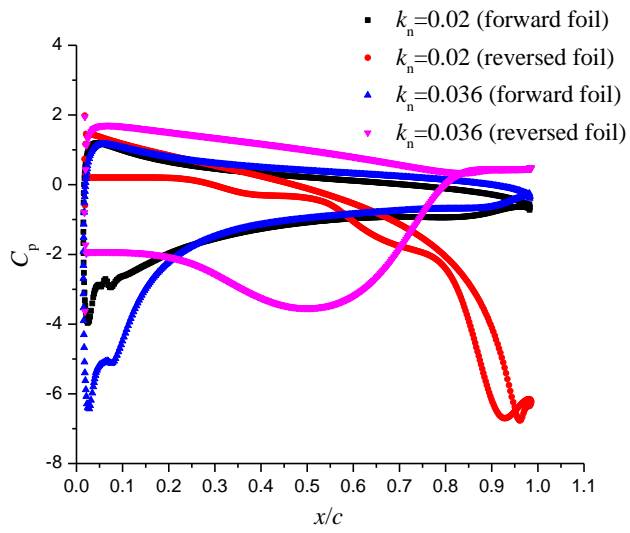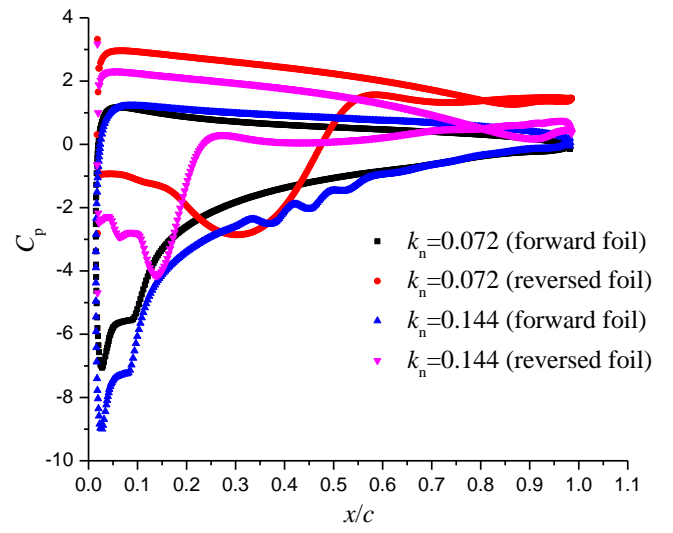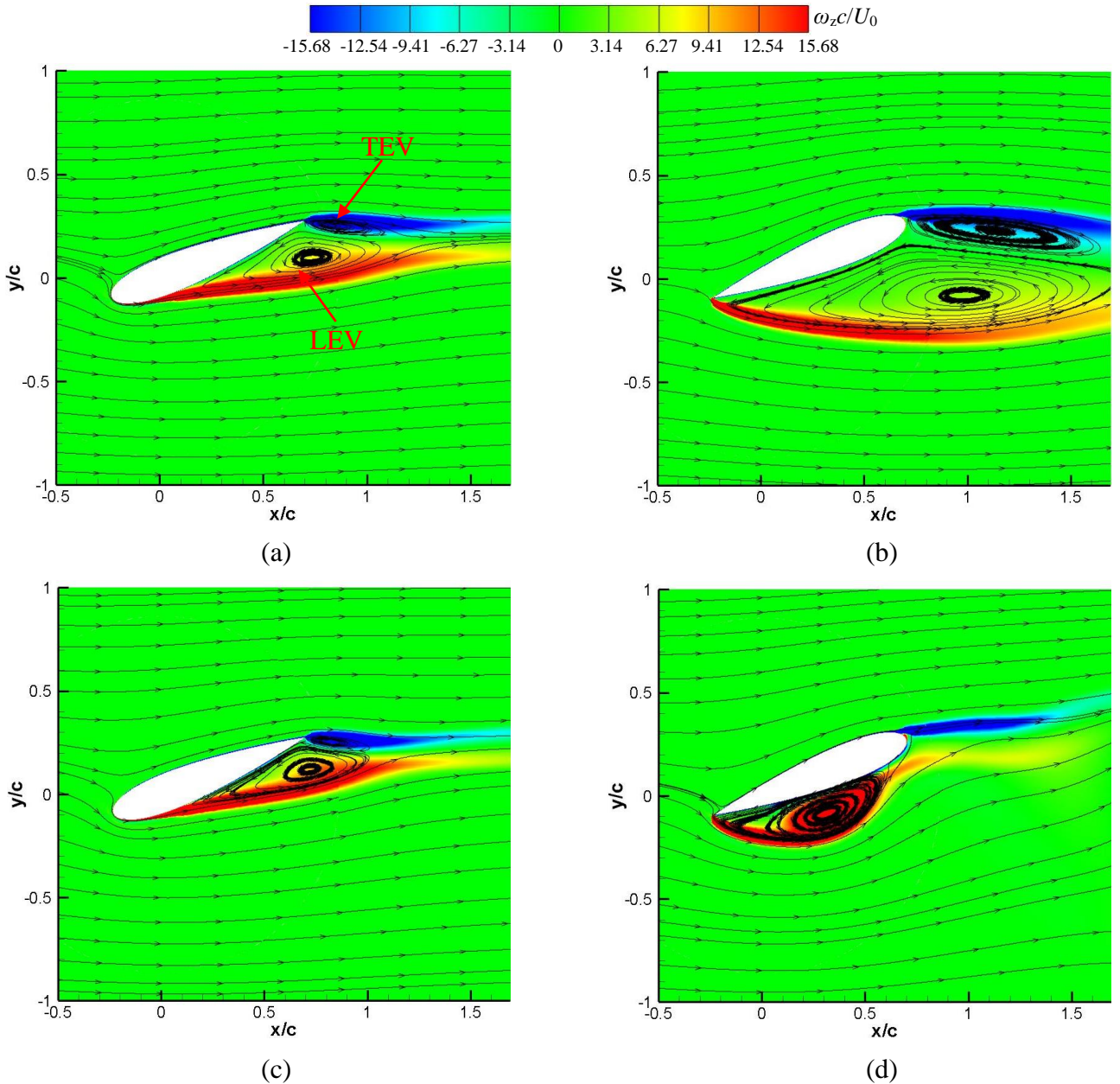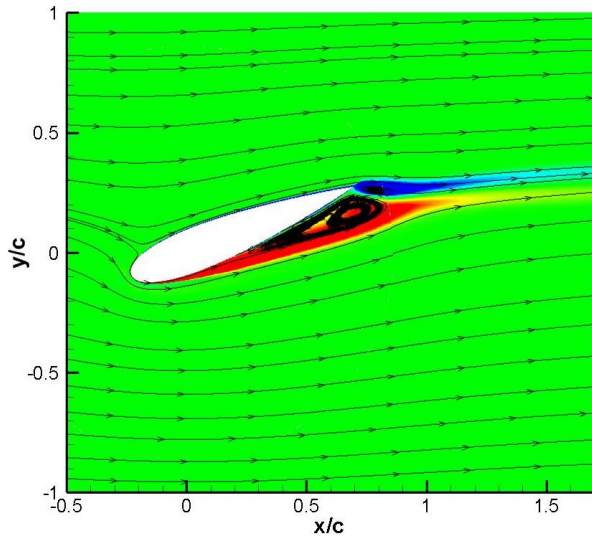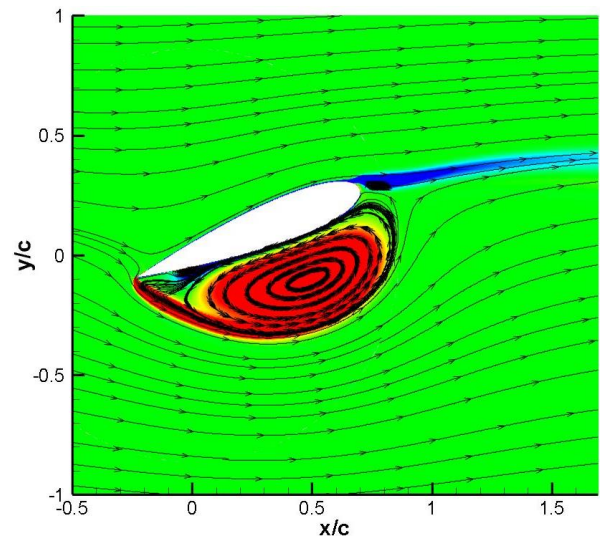
(b)

(c)

(d)
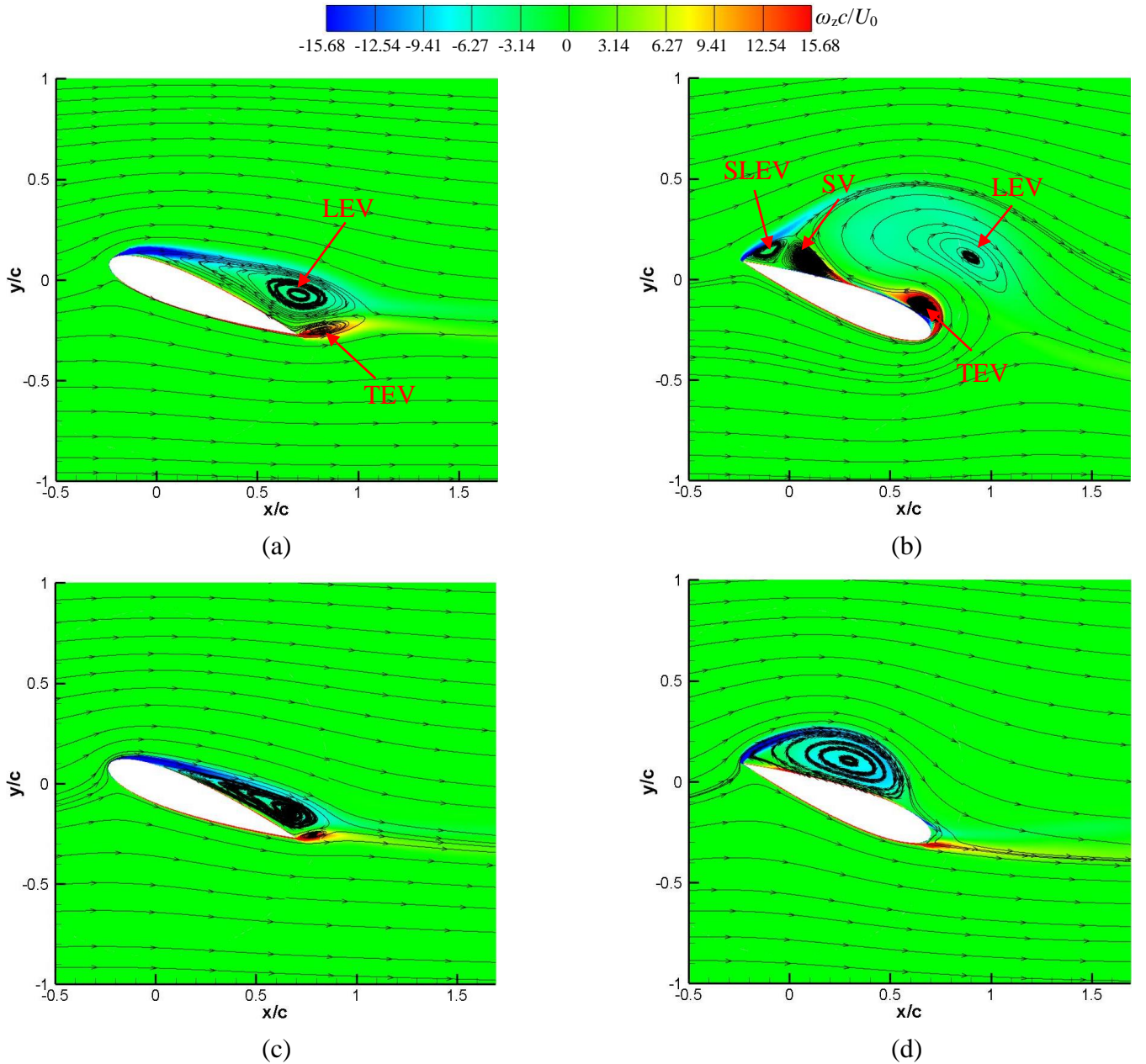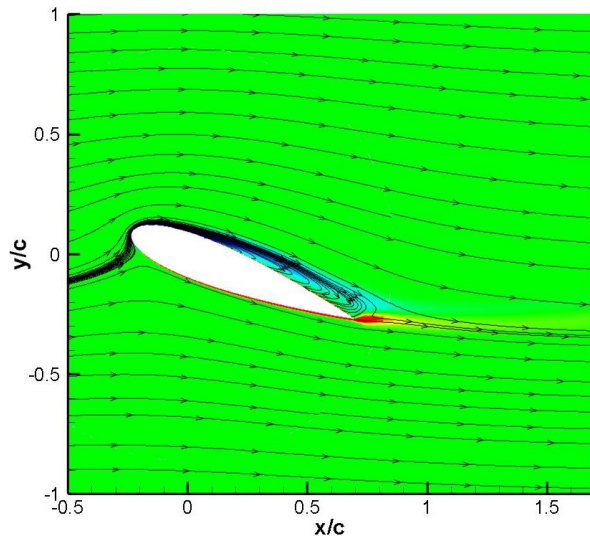
(e)
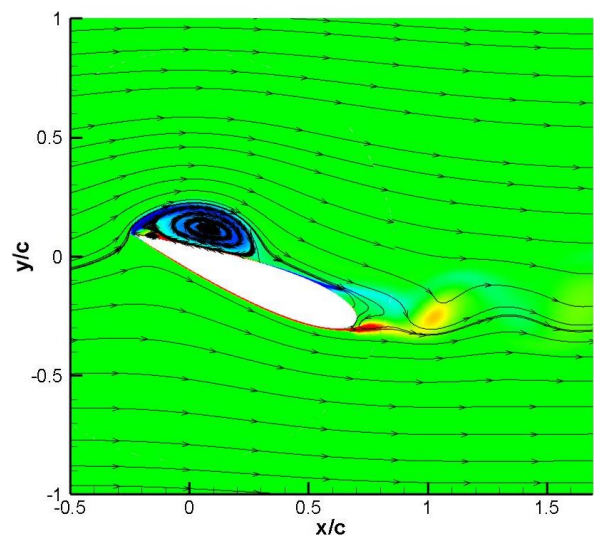
(f)

(g)

(h)

(i)

(j)

Fig.19 Vortex structures and pressure distributions at $\Phi=45°$. (a) and (b) $k_n=0.020$; (c) and (d) $k_n=0.036$; (e) and (f) $k_n=0.072$; (g) and (h) $k_n=0.144$; (i) and (j) Pressure coefficients.

Then, the vortical flows at $\Phi=225°$ when the freestream velocity is maximal are displayed in figure 20. Generally, the flow separation at this moment is more obvious than that at $\Phi=45°$, as a consequence of the relatively large instantaneous freestream Reynolds number. The main feature of the flow structure is that the LEV and TEV emerge on the lower surface, but it is more evident for the reversed airfoil. With the increase of k_n, the flow is postponed, characterized by the LEV size and location. It is very interesting that the LEV size is much larger at $k_n=0.072$ than that at $k_n=0.036$. At $k_n=0.144$, the LEV over the surface of the forwards airfoil becomes unclear. The pressure distribution of the forward airfoil has no much difference at various k_n, but the pressure difference becomes large. However, the LEV over the reversed airfoil has a great impact on the performance, especially at $k_n=0.072$ when a large-scale LEV occupies almost the whole lower surface. Generally, it seems that the flow morphology change is quite similar, compare with that at $\Phi=45°$, but has a slight difference at $k_n=0.072$ for the reversed airfoil. By the way, the vortex at this moment is relatively far away from the surface and the size is also small, due to the large freestream Reynolds number.

(a)

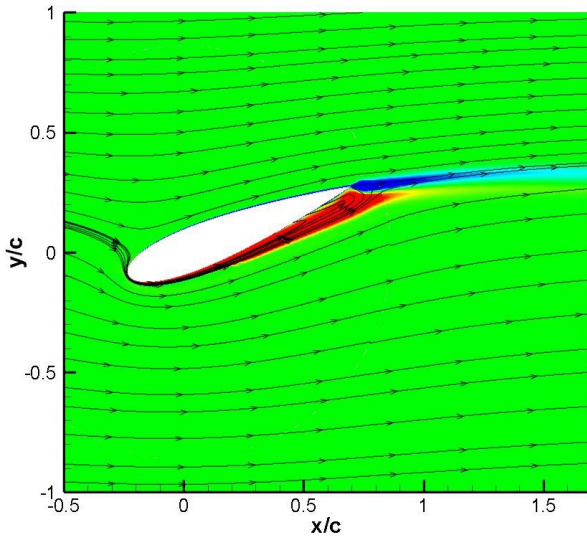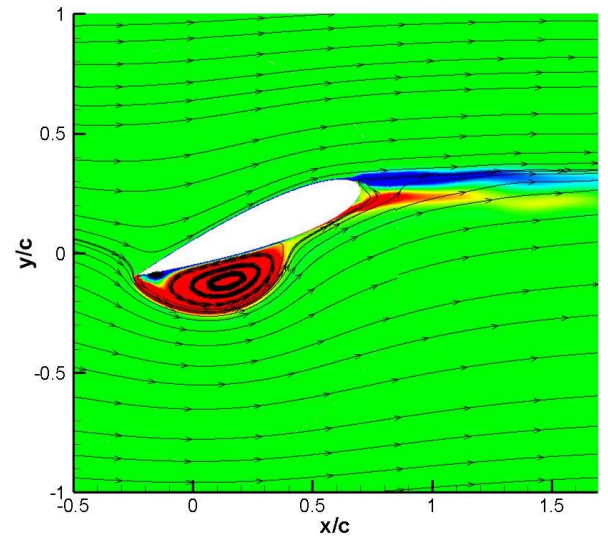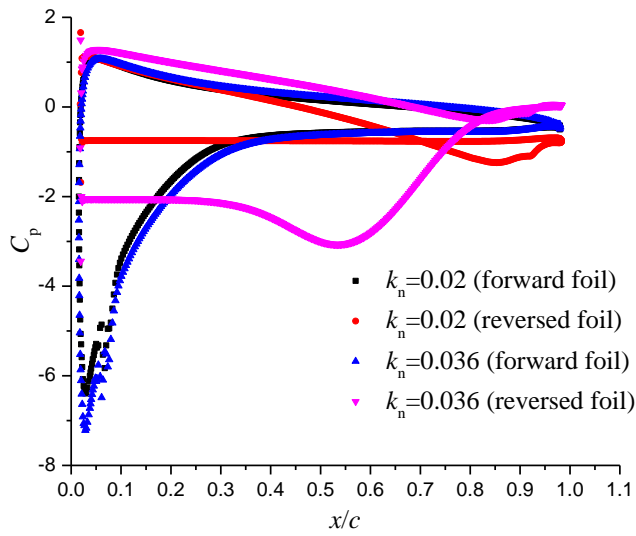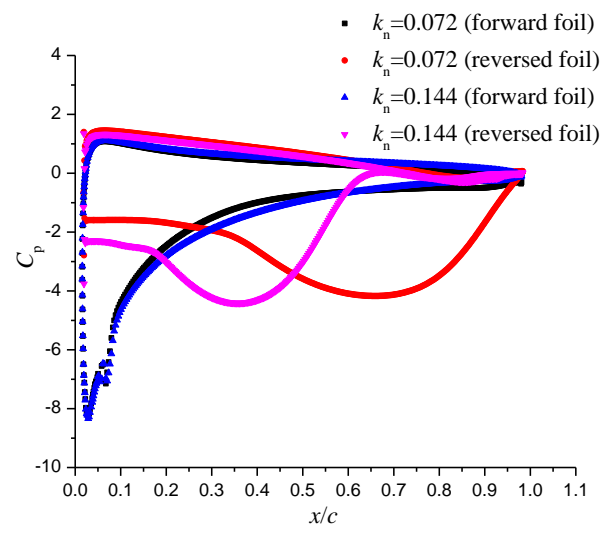(b)

(c)

(d)

(e)

(f)

(g)

(h)

(i)

(j)

Fig.20 Vortex structures and pressure distributions at $\Phi=225°$. (a) and (b) $k_n=0.020$; (c) and (d) $k_n=0.036$; (e) and (f) $k_n=0.072$; (g) and (h) $k_n=0.144$; (i) and (j) Pressure coefficients.

The distributions of the intermittency and skin friction coefficient are employed to reveal the influence of k_n on the transition event, as shown in figure 21. At k_n=0.02 and 0.036, the LSB over the forward airfoil is still on the screen, but the separation and reattachment points move downstream. Then, there is no reattachment of the separated shear layer when the reduced frequency is 0.072 and 0.144 for the forward airfoil, which means that the LSB becomes unclear gradually. However, the leading-edge flow-separation-induced LSB makes the contribution to the transition over the reversed airfoil. With the increase of k_n, the size of LSB becomes smaller, shown by the reattachment point moving upstream. In addition, near the trailing edge, the location of small-scale LSB on the upper surface is more upstream with k_n, but the transition on the lower surface moves downstream. As k_n increases to 0.144, there is nearly no flow separation near the sharp leading edge, but the transition occurs on the lower surface. Thus, it concludes that the transition is also delayed with the increase of k_n, but the situation is quite different on the forward and reversed airfoils.
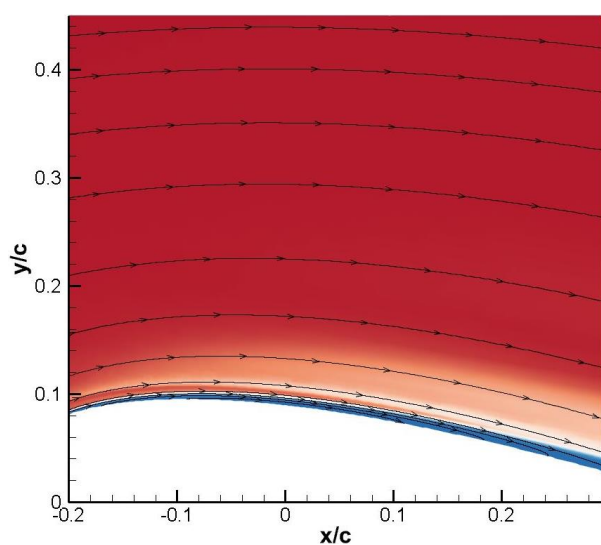

(a)

(b)

(c)

(d)
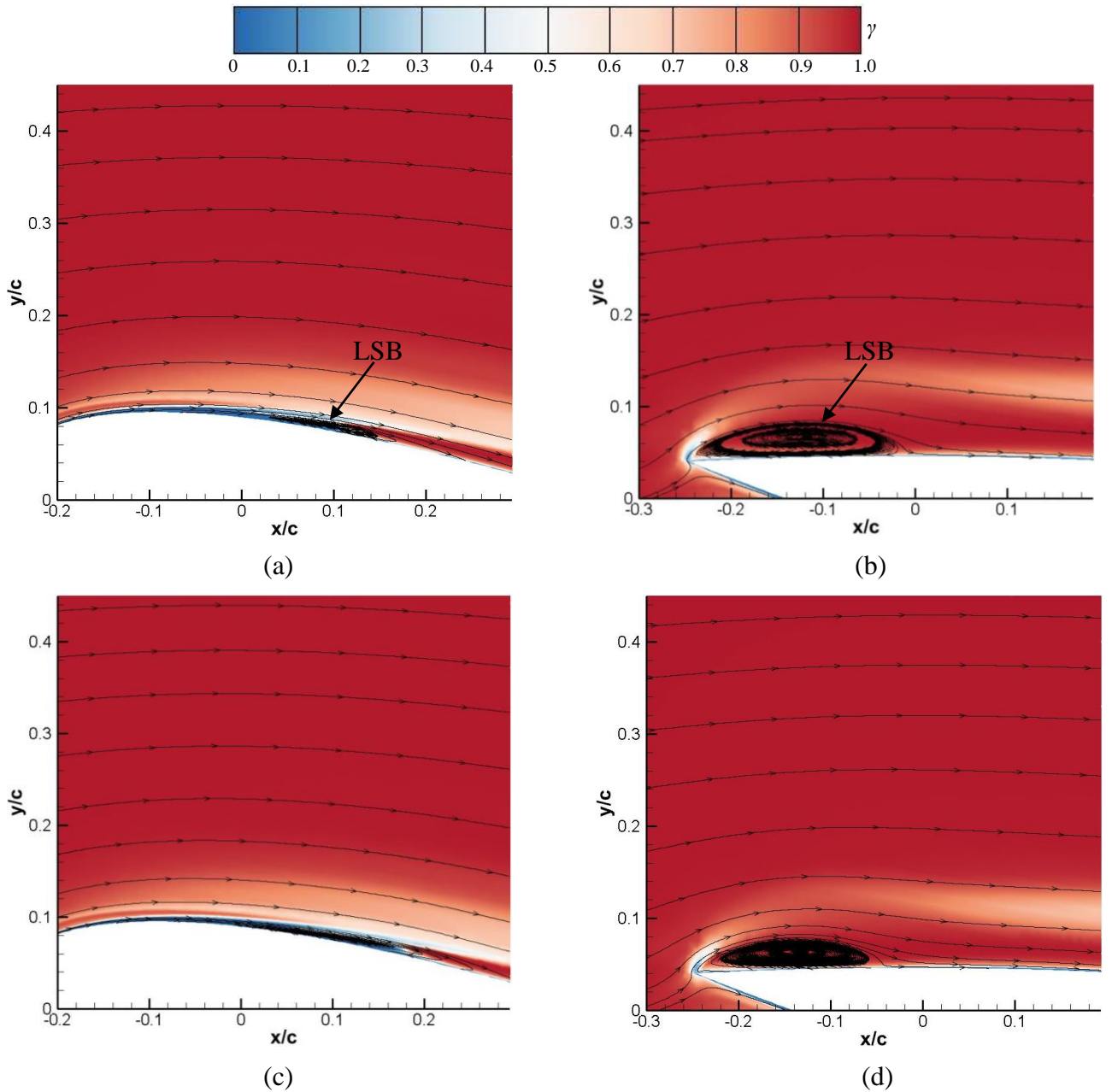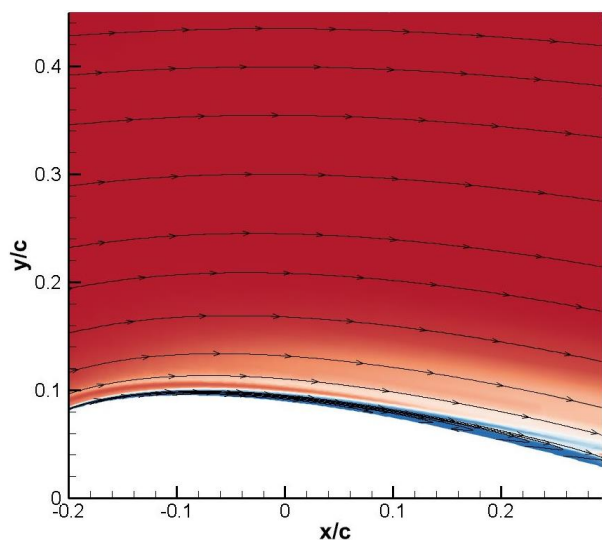
(e)
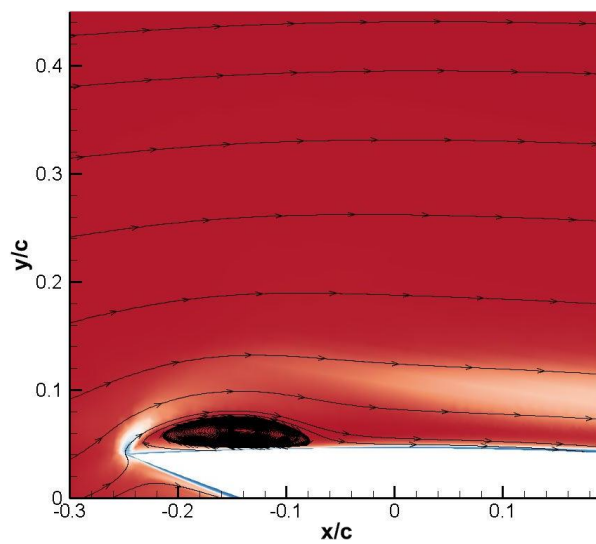
(f)

(g)
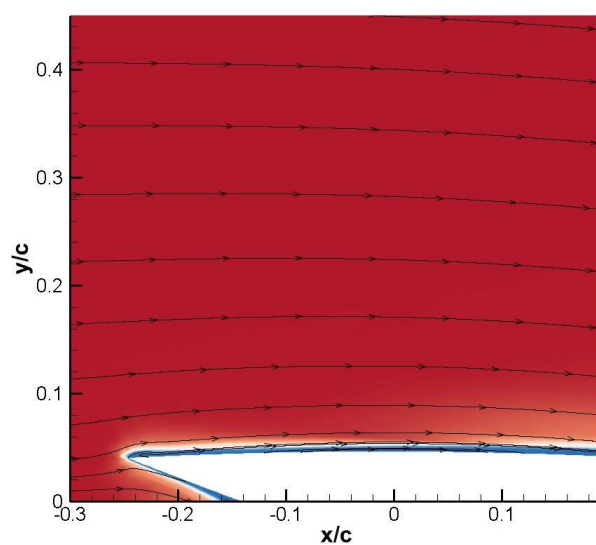
(h)
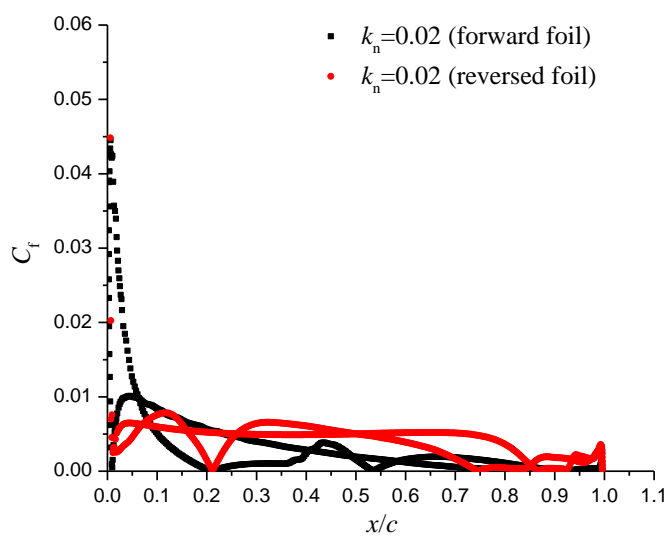
(i)
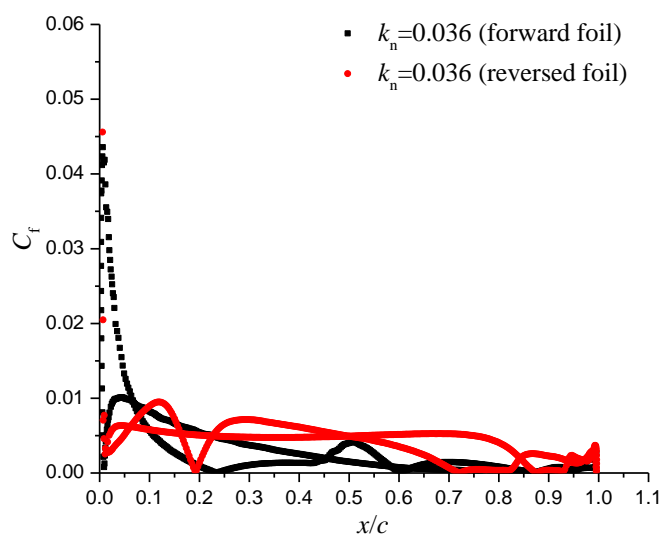
(j)
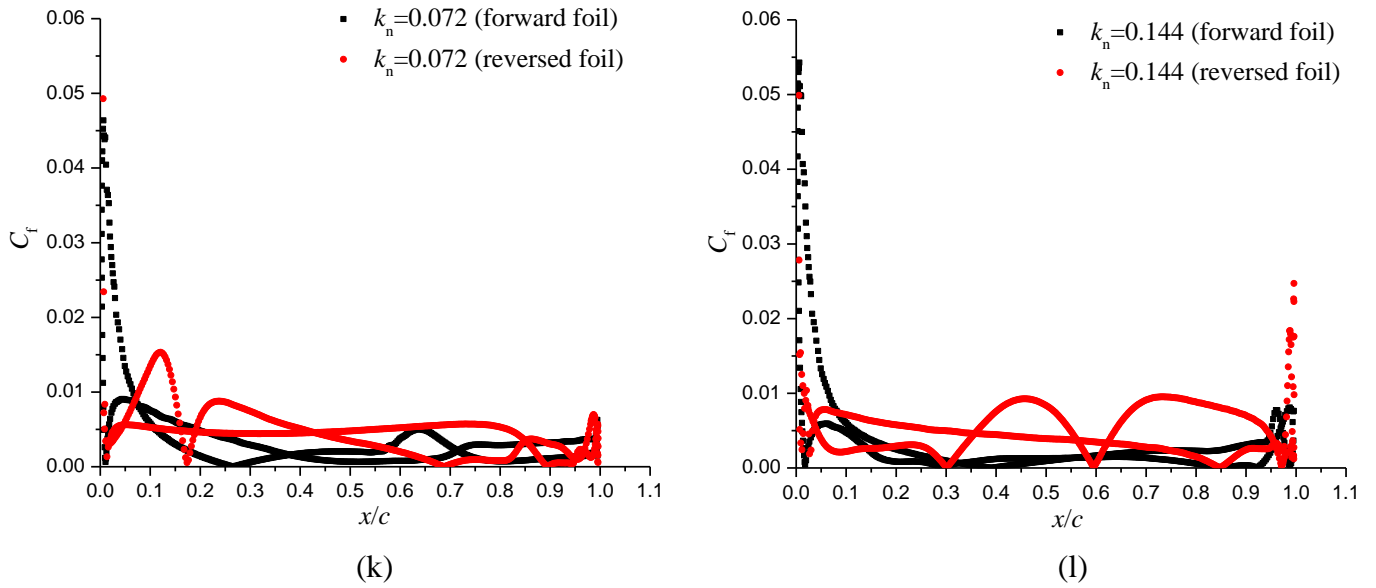
Fig.21 Transition and skin friction coefficients at $\Phi=18^{\circ}$. (a) and (b) $k_n=0.020$; (c) and (d) $k_n=0.036$; (e) and (f) $k_n=0.072$; (g) and (h) $k_n=0.144$; (i), (j), (k) and (l) Skin friction coefficients.

The vortical flows under dynamic stall condition when the airfoil has the maximal incidence are presented in figure 22, at different k_n. It shows that the flow structures over the forward airfoil develop completely and the LEV starts to separate when k_n is 0.02. But on the reversed airfoil, it nearly vanishes and moves downstream. Simultaneously, the TEV and SV appear near the leading edge. When k_n increases to 0.036, the LEV still attaches on the airfoil surface with SLEV and SV. Then, with the further increase of k_n, the LEV separates from the upper surface and other three vortex structures develop fully. It seems that the flow separation at $k_n=0.072$ occurs earlier than that at $k_n=0.036$, which is the same with that in figure 19 and 20. This can be responsible for the relatively large drag coefficient shown in figure 18g. Finally, in figure 22g and 22h, all the vortices are still in the early stage of the development.
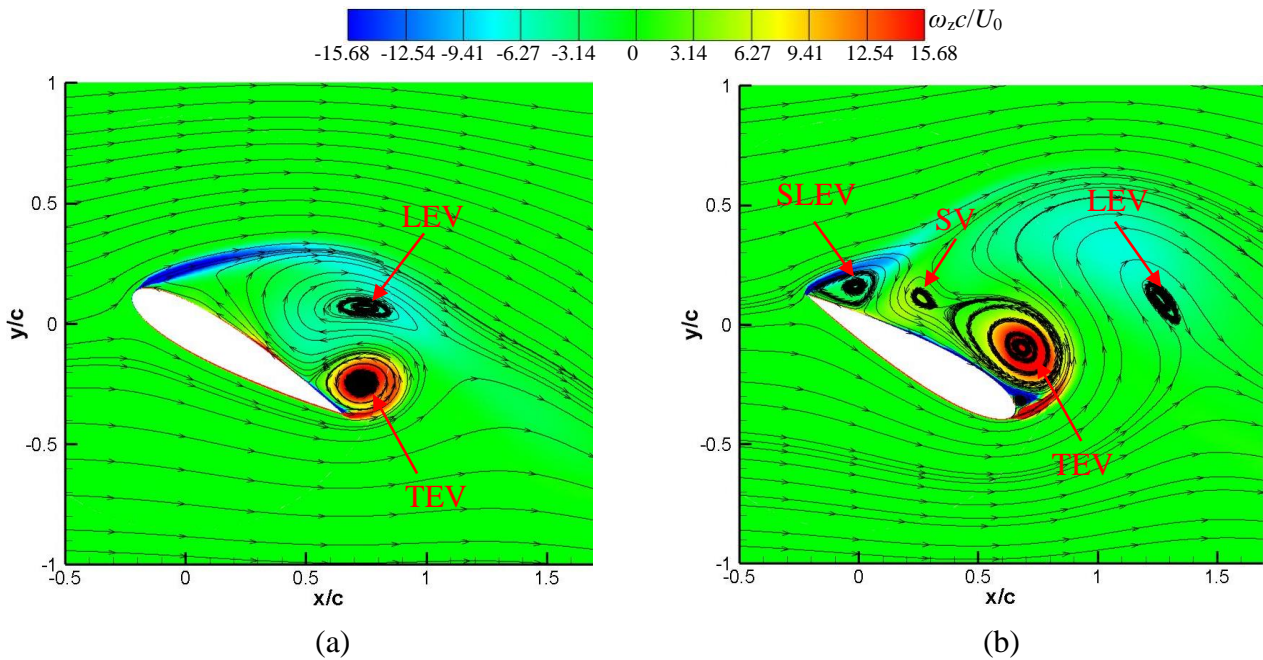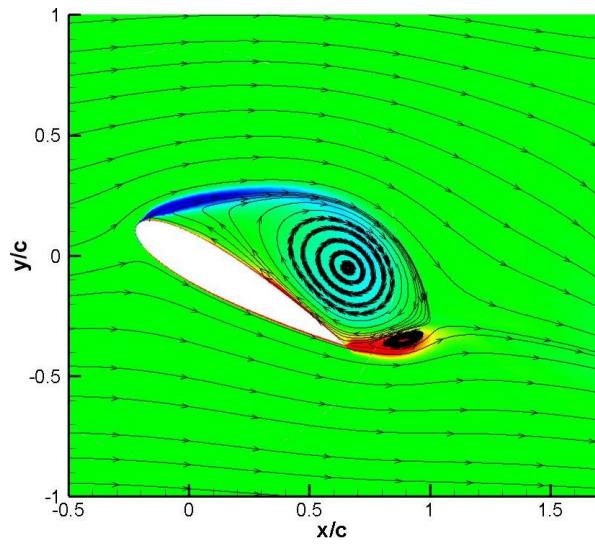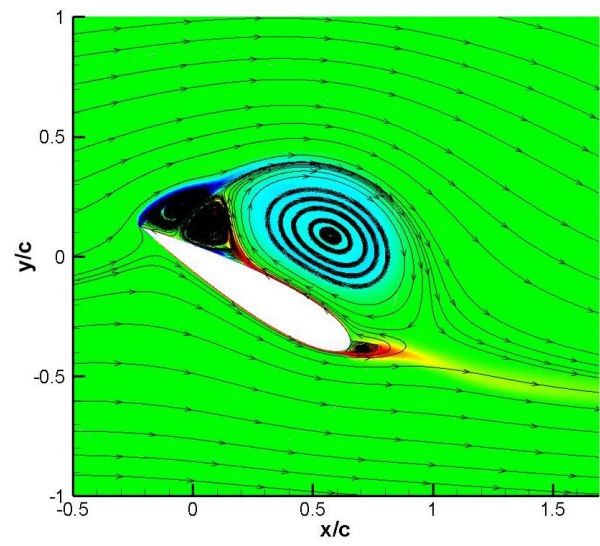
Fig.22 Vortex dynamics at $\Phi=90°$. (a) and (b) $k_n=0.020$; (c) and (d) $k_n=0.036$; (e) and (f) $k_n=0.072$; (g) and (h) $k_n=0.144$.

The velocity profiles in the wake region at various k_n are plotted in figure 23. Generally, the velocity distribution of the reversed airfoil is affected remarkably by the vortex shedding, compared with that of the forward airfoil, indicating that the velocity deficit is relatively large for th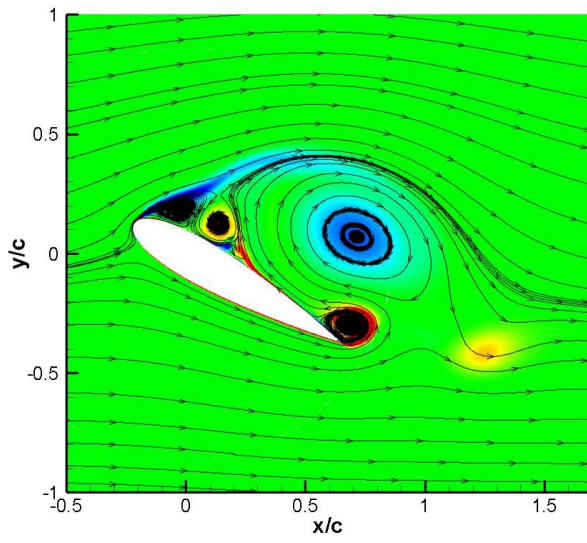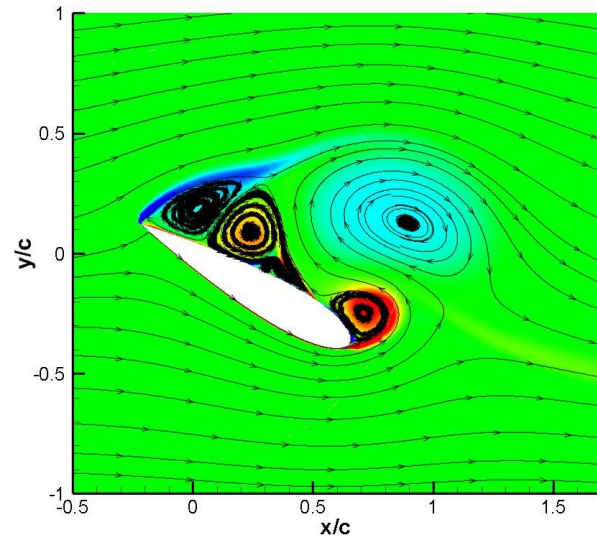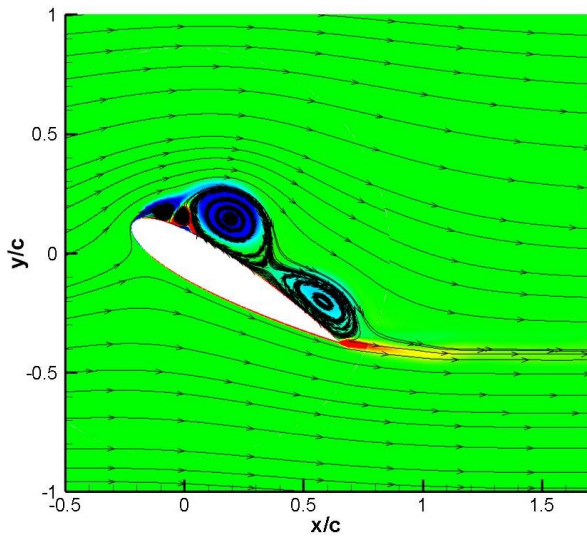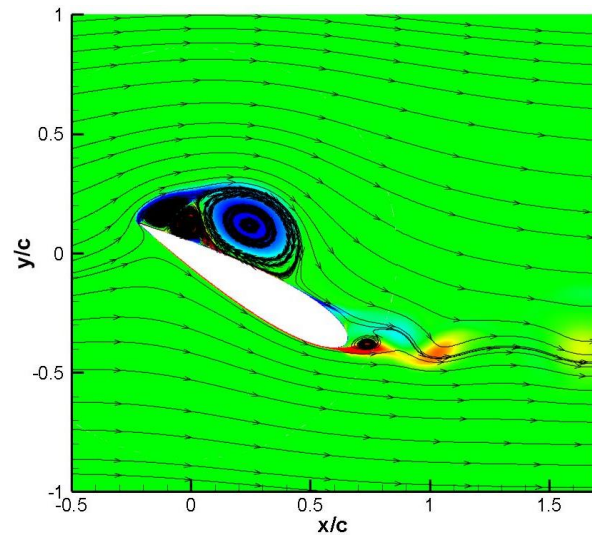e reversed airfoil. For an instance, the velocity variation in the vertical direction at $k_n=0.02$ is extremely large, due to the massive flow separation, as is shown 22b. Besides, the velocity variation at $k_n=0.072$ is relatively obvious than that at $k_n=0.036$, due to the earlier flow separation, which can be used to the clarify the large drag coefficient in figure 18g. Afterwards, downstream from the airfoil at $x/c=2.87$, the large variation of the velocity occurs for the case with $k_n=0.36$ for two configurations, because of the vortical flows convecting downstream. Besides, it seems that there exists a transition from drag-indicative to thrust-indicative type of the velocity profile as k_n increases. In a conclusion, the delayed flow structure with the increase of k_n also leads to different velocity profiles in the wake region, which should be further investigated in detail.

(a) (b)
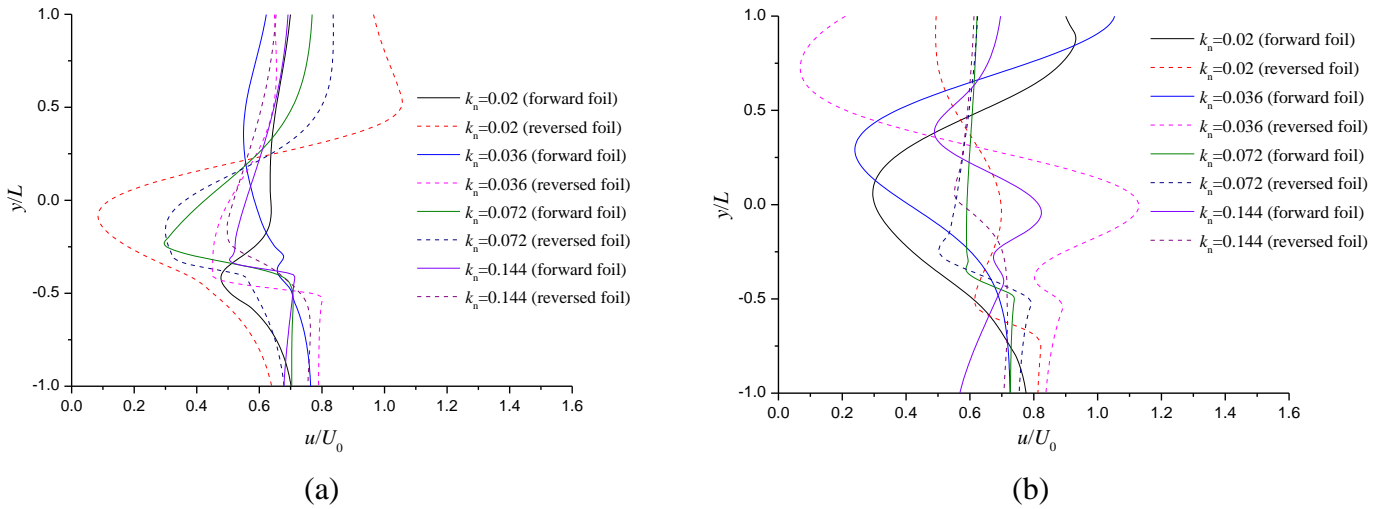
Fig.23 Wake velocity profiles at $\Phi=90°$. (a) $x/c=1.22$; (b) $x/c=2.87$.

4. Concluding remarks and future work

The global performance, transition and vortex dynamics of forward and reversed airfoils are investigated in the present work, under different oscillating freestream conditions. The influence of the phase lag, oscillating amplitude and mean reduced frequency are analyzed deeply. The main conclusions are obtained as follows:

(1) The performance varies considerably for the cases with different phase lags, which depends on the freestream instantaneous Reynolds number. When the freestream velocity is relatively large, the flow separation is more evident. The increase of the pitching amplitude leads to the large oscillation of the performance, but the trend is opposite for two phase lags when the freestream has the maximal and minimal values. When it comes to the transition, the size of LSB becomes short at large freestream instantaneous Reynolds number, mainly induced by the upstream movement of the reattachment point.

(2) The flow structures over the reversed airfoil are more complicated than that on the forward airfoil, shown by the performance fluctuation and vortex dynamics. Simultaneously, increasing oscillating amplitude can improve the mean performance, especially for the forward airfoil when the oscillating amplitude is larger than 0.2. Furthermore, the drag of the reversed airfoil is much higher than that of the forward airfoil, but it has a decrease with σ. At $\Phi=45°$, the freestream velocity is extremely low as σ is 0.9, leading to the complex flow field for the reversed airfoil.

Then, the flow structure has a massive separation at $\Phi=225^{\circ}$, due to the increase of the freestream velocity with σ. The flow-separation-induced LSB near the reversed airfoil leading edge makes the contribution to the transition, and then the flow reattaches after the LSB. Afterwards, a transition on both two sides near the trailing edge is detected again, indicating that there is a second transition occurrence. However, this process becomes weak with the increase of σ, due to the low freestream Reynolds number.

(3)   The time-averaged performance of the reversed airfoil changes significantly with k_n. The lift coefficient decreases for two configurations, especially for the reversed airfoil. Additionally, although the drag coefficient of the reversed airfoil is much higher than that of the forwards airfoil, it increases remarkably for the forward airfoil. In general, vortex structures and the transition are delayed as k_n increases. However, when k_n is 0.072, it seems that the flow separation occurs earlier than that at $k_n= 0.036$. The delayed flow structure can be inferred from the velocity profiles in the wake region, and there is a transition from the drag-indicative to thrust-indicative type with the increase of k_n.

Due to the earlier flow separation near the sharp leading edge, the detailed near-wall flow structures are deserved to be investigated deeply over the reversed airfoil, using the hybrid RANS/LES or large eddy simulation (LES), to analyze the energy loss induced by the flow-separation-induced bubble near the sharp leading edge and second transition on the trailing edge.

Acknowledgement

References

[1]   Wu, X., Zhang, X., Tian, X., Li, X., & Lu, W. (2020). A review on fluid dynamics of flapping foils. *Ocean Engineering*, 195, 106712 (1-30).

[2]   Wang, S., Ingham, D. B., Ma, L., Pourkashanian, M., & Tao, Z. (2010). Numerical investigations on dynamic stall of low Reynolds number flow around oscillating airfoils. *Computers & fluids*, *39*(9), 1529-1541.

[3]   Wang, S., Ingham, D. B., Ma, L., Pourkashanian, M., & Tao, Z. (2012). Turbulence modeling of deep dynamic stall at relatively low Reynolds number. *Journal of Fluids and Structures*, *33*, 191-209.

[4]   Tseng, C. C., & Cheng, Y. E. (2015). Numerical investigations of the vortex interactions for a flow over a pitching foil at different stages. *Journal of fluids and structures*, *58*, 291-318.

[5]   Tseng, C. C., & Hu, H. A. (2016). Flow dynamics of a pitching foil by Eulerian and Lagrangian viewpoints. *AIAA Journal*, *54*(2), 712-727.

[6]   Menter, F. R., Langtry, R. B., Likki, S. R., Suzen, Y. B., Huang, P. G., & Völker, S. (2006). A correlation-based transition model using local variables—part I: model formulation. *Journal of Turbomachinery*, 128, 413-422.

[7]   Menter, F. R., Langtry, R., & Völker, S. (2006). Transition modelling for general purpose CFD codes. *Flow, Turbulence and Combustion*, *77*(1-4), 277-303.

[8]   Ducoin, A., Astolfi, J. A., Deniset, F., & Sigrist, J. F. (2009). Computational and experimental investigation of flow over a transient pitching hydrofoil. *European Journal of Mechanics-B/Fluids*, *28*(6), 728-743.

[9]   Zhang, M., Wu, Q., Wang, G., Huang, B., Fu, X., & Chen, J. (2020). The flow regime and hydrodynamic performance for a pitching hydrofoil. *Renewable Energy*, *150*, 412-427.

[10]   Lind, A. H., Lefebvre, J. N., & Jones, A. R. (2014). Time-averaged aerodynamics of sharp and blunt trailing-edge static airfoils in reverse flow. *AIAA Journal*, *52*(12), 2751-2764.

[11]   Lind, A. H., & Jones, A. R. (2015). Vortex shedding from airfoils in reverse flow. *AIAA Journal*, *53*(9), 2621-2633.

[12]   Lind, A. H., Smith, L. R., Milluzzo, J. I., & Jones, A. R. (2016). Reynolds number effects on rotor blade sections in reverse flow. *Journal of Aircraft*, *53*(5), 1248-1260.

[13]   Marchand, J. B., Astolfi, J. A., & Bot, P. (2017). Discontinuity of lift on a hydrofoil in reversed flow for tidal turbine application. *European Journal of Mechanics-B/Fluids*, *63*, 90-99.

[14]   Lind, A. H., & Jones, A. R. (2016). Unsteady aerodynamics of reverse flow dynamic stall on an oscillating blade section. *Physics of Fluids*, *28*(7), 077102 (1-22).

[15]   Smith, L. R., & Jones, A. R. (2019). Measurements on a yawed rotor blade pitching in reverse flow. *Physical Review Fluids*, 4(3), 034703 (1-20).

[16]   Gursul, I., & Ho, C. M. (1992). High aerodynamic loads on an airfoil submerged in an unsteady stream. *AIAA Journal*, *30*(4), 1117-1119.

[17]   Brendel, M., & Mueller, T. J. (1988). Boundary layer measurements on an airfoil at a low Reynolds number in an oscillating freestream. *AIAA Journal*, *26*(3), 257-263.

[18]   Strangfeld, C., Müller-Vahl, H., Nayeri, C. N., Paschereit, C. O., & Greenblatt, D. (2016). Airfoil in a high amplitude oscillating stream. *Journal of Fluid Mechanics*, 793, 79-108.

[19]   Pierce, G. A., Kunz, D. L., & Malone, J. B. (1978). The effect of varying freestream velocity on airfoil dynamic stall characteristics. *Journal of the American Helicopter Society*, *23*(2), 27-33.

[20]   Müller-Vahl, H. F., Strangfeld, C., Nayeri, C. N., Paschereit, C. O., & Greenblatt, D. (2020). Dynamic stall under combined pitching and surging. *AIAA Journal*, *58*(12), 5134-5145.

[21]   Gharali, K., & Johnson, D. A. (2013). Dynamic stall simulation of a pitching airfoil under unsteady freestream velocity. *Journal of Fluids and Structures*, *42*, 228-244.

[22]   Ma, P., Wang, Y., Xie, Y., & Huo, Z. (2018). Effects of time-varying freestream velocity on energy harvesting using an oscillating foil. *Ocean Engineering*, *153*, 353-362.

[23]   Shi, Z. W., & Ming, X. (2008). Effects of unsteady freestream on aerodynamic characteristics of a pitching Delta wing. *Journal of Aircraft*, *45*(6), 2182-2185.

[24]   Smith, L. R., & Jones, A. R. (2020). Vortex formation on a pitching aerofoil at high surging amplitudes. *Journal of Fluid Mechanics*, *905*, A22 (1-26).

[25]   Kirk, P. B., & Jones, A. R. (2019). Vortex formation on surging aerofoils with application to reverse flow modelling. *Journal of Fluid Mechanics*, *859*, 59-88.

[26]   Menter, F. R., Kuntz, M., & Langtry, R. (2003). Ten years of industrial experience with the SST turbulence model. *Turbulence, Heat and Mass Transfer*, *4*(1), 625-632.

[27]   Dong, H., Xia, T., Chen, L., Liu, S., Cui, Y. D., Khoo, B. C., & Zhao, A. (2019). Study on flow separation and transition of the airfoil in low Reynolds number. *Physics of Fluids*, *31*(10), 103601 (1-9).

[28]   Wang, R., & Xiao, Z. (2020). Transition effects on flow characteristics around a static two-dimensional airfoil. *Physics of Fluids*, *32*(3), 035113 (1-14).

[29]   Moran-Guerrero, A., Gonzalez-Gutierrez, L. M., Oliva-Remola, A., & Diaz-Ojeda, H. R. (2018). On the influence of transition modelling and crossflow effects on open water propeller simulations. *Ocean Engineering*, *156*, 101-119.

[30]   Lanzafame, R., Mauro, S., & Messina, M. (2013). Wind turbine CFD modelling using a correlation-based transitional model. *Renewable Energy*, *52*, 31-39.

[31]   Martinat, G., Braza, M., Hoarau, Y., & Harran, G. (2008). Turbulence modelling of the flow past a pitching NACA0012 airfoil at 10^5 and 10^6 Reynolds numbers. *Journal of Fluids and Structures*, *24*(8), 1294-1303.

[32]   Kim, D. H., & Chang, J. W. (2014). Low-Reynolds-number effect on the aerodynamic characteristics of a pitching NACA0012 airfoil. *Aerospace Science and Technology*, *32*(1), 162-168.

[33]   Boutilier, M. S., & Yarusevych, S. (2012). Separated shear layer transition over an airfoil at a low Reynolds number. *Physics of Fluids*, *24*(8), 084105 (1-23).